METHODS TO CHARACTERIZE THE PERFORMANCE OF HEAD DISK INTERFACE USING A MULTIFUNCTIONAL SPINSTAND

BUDI SANTOSO

B.ENG (HONS), NUS

A THESIS SUBMITTED FOR
THE DEGREE OF MASTER OF ENGINEERING

DEPARTMENT OF ELECTRICAL AND COMPUTER ENGINEERING

NATIONAL UNIVERSITY OF SINGAPORE

2011

ACKNOWLEDGEMENT

I would like to extend my sincere gratitude to my supervisor and advisor, Dr. Yuan Zhimin, for his outstanding guidance and support in the course of my work which leads to a fruitful completion of this thesis. His vast knowledge in the area of high density magnetic recording and his expertise in nano-instrumentation technology will continue to inspire me in the future and beyond.

I would also like to thank Dr. Leong Siang Huei for his mentorship in many aspects of this thesis and for his great advice, expertise in the area of nano-instrumentation. I am equally grateful to the recording physics and systems team of Data Storage Institute (DSI), in particular, Mr. Ong Chun Lian and Mr. Lim Joo Boon Marcus Travis who have provided me with lots of helpful support and experience in the course of this work.

Finally, I am fortunate to be able to work at the Data Storage Institute (DSI) as it is indeed a world class working facility within the comfort zone of the National University of Singapore and the Department of Electrical and Computer Engineering.

TABLE OF CONTENTS

SUMMARY

A multifunctional spinstand has been developed to integrate Head Disk Interface (HDI) measurement tools such as Acoustic Emission (AE), Laser Doppler Vibrometer (LDV) and missing pulse electronics to provide concurrent measurement capability to characterize slider dynamics and media defects. In this case, multifold information can be obtained that will help to remove spurious information present in any single scan. It has been shown that the LDV's capability to detect media defects is comparable to the Optical Surface Analyzer (OSA) and through a special enhancement method, the LDV can also be used concurrently with missing pulse to perform media defect certification that is fast and more efficient.

Measurement of slider dynamics are carried out in two different test conditions. In the first test condition, mapping of slider-defect interaction provides two-dimensional information on the size of the interaction regime and nature of interactions. Such a mapping approach is suggested for useful characterization of sliders, in particular, thermal activated protrusions from Thermal Fly Height Control (TFC) technology. Secondly, slider dynamics of ultra-low flying heights are studied using thermal protrusion. Here, contact induced vibration is analyzed in both frequency and time domain to better understand the touch down process. It is pointed out that slider dynamics is a slider design specific characteristics and frequency domain analysis is shown to be useful to characterize the slider's mechanical response. Time domain information helps to reveal slider's interaction with media surface. Concurrent methods can help to provide better understanding of slider-lube interactions using sensitivity of different measurement methods.

Tribocharging is a critical HDI phenomenon at ultra-low flying heights. Tribocharge buildup at the slider-disk interface was investigated by measuring tribocurrent at the head disk interface in three regimes: slider flying and disk deceleration, slider dragging at constant

speed, and disk acceleration to slider flying. In general, the tribocharging is different for deceleration and acceleration regimes and is shown to be related to velocity and acceleration. The onset appearance and changes to the tribocurrent occur at different disk velocity (and have different peak values) for different initial velocities used. Additional tribovoltage and AE measurements are performed to correlate and help explain the tribocharging occurrence at the interface.

Keywords: Flying height; In-situ Fly Height; Thermal Fly Height Control; Slider dynamics; Media Defect, Laser Doppler Vibrometer, Missing Pulse, Tribocharging

LIST OF TABLES

LIST OF FIGURES

LIST OF ABBREVIATIONS

ABS	Air Bearing Surface
AE	Acoustic Emission
AFC	Anti-Ferromagnetic Coupling
AFM	Atomic Force Microscope
AM	Amplitude Modulation
CIP	Current-in-Plane
CMR	Colossal Magneto Resistance
CMRR	Common Mode Rejection Ratio
CPP	Current Perpendicular-to-Plane
DLC	Diamond-Like Carbon
DLL	Dynamic-Link Library
DSI	Data Storage Institute
DUT	Device under Test
FIB	Focused Ion Beam
FH	Flying Height
GCS	General Command Set
GUI	Graphical User Interface
GMR	Giant Magneto Resistance
GPIB	General Purpose Interface Bus
HDD	Hard Disk Drive
HDI	Head Disk Interface
HGA	Head Gimbal Assembly
HSA	Head Stack Assembly
ID	Inner Diameter
IDEMA	International Disk Drive and Equipment & Materials

INSIC	Information Storage Industry Consortium
LDV	Laser Doppler Vibrometer
LZT	Laser Zone Texture
MCU	Micro Controller Unit
MP	Missing Pulse
NPLC	Number of Power Line Cycles
OSA	Optical Surface Analyzer
PCB	Printed Circuit Board
PCI	Peripheral Component Interconnect
PES	Position Error Signal
PSD	Photo Sensitive Detector
PTP	Pole Tip Protrusion
PZT	Piezoelectric Transducer
RAMAC	Random Access Method of Accounting and Control
RF	Radio Frequency
RMS	Root Mean Square
RPM	Revolution Per Minute
RRO	Repeatable Run Out
SNR	Signal to Noise Ratio
SPI	Serial Peripheral Interface
SUL	Soft Under Layer
TA	Thermal Asperity
TFC	Thermal Fly Height Control
TGMR	Tunneling Magneto Resistance
TPI	Track Per Inch
USB	Universal Serial Bus
VCM	Voice Coil Motor

VISA	Virtual Instrument Software Architecture

LIST OF SYMBOLS

f	Frequency
K_u	Anisotropy constant
λ	Wavelength
V	Volume; velocity; voltage
t	Time
T	Temperature
g	Head gap length
I	Current
R	Resistance
C	Capacitance
Q	Charge
d	Head media spacing; depth
w	Width
φ	Phase
J	Current density
k	Boltzmann constant; wave number
ε	Dielectric constant
τ	Time constant
A	Servo burst A; arbitrary constant
B	Servo burst B; arbitrary constant
C	Arbitrary constant

LV	Linear velocity
β	Temperature coefficient
v	Velocity
x	Position; horizontal cartesian axis
y	Vertical cartesian axis
L	Suspension length
r	Radius from disk center
θ	Skew angle; angle

CHAPTER 1: Introduction

1.1 The Hard Disk Drive Evolution

The hard disk drive (HDD) celebrated its glorious 50 years anniversary of innovation in 2006. Since it was invented in 1956 by IBM as Random Access Method for Accounting and Control (RAMAC), the IBM 350, magnetic storage technology has enjoyed tremendous growth in areal density with significant reduction in cost and form factor. Back then, each IBM 350 RAMAC unit contains thirty 24" diameter magnetic disks with a combined capacity of 4.4MB [1]. This translates to 5 million binary 7-bit decimal encoded characters. The recording density, defined as the number of bits per square inch area of magnetic disk surface, was only 2 kb/in^2. The cost is so high, such that IBM provides rental service for 350 RAMAC users with rental cost of $130 a month for a megabyte of storage.

Today, hard disk drive is the highest capacity non-volatile storage device which can store up to 600GB of data on a single 3.5" platter with an areal density of 540 Gb/in^2 [2]. This is approximately a factor of over 200 million increments in areal density. The roadmap of magnetic storage devices, charted by Wood *et al* [3] in Figure 1-1, shows that from 1956 to 1991 the average growth rate was 39% per annum. With the invention of Giant Magnetoresistance (GMR) read head in the early 1990s, the growth rate of areal density per annum increases at a phenomenal rate of 65% and at times, even surpassing the rate of growth of semiconductor industry. This growth rate has brought about significant evolution in high quality digital media, entertainment, as well as consumer electronics.

In 2007, the discovery of GMR was awarded Nobel Prize in physics [4]. The continual growth rate in areal density is further sustained with the driving implementation of perpendicular recording technology which is still the dominant technology today. As bit size reduces, the volume of the material that constitutes the bit also decreases. This results in the

reduction of magnetic anisotropy energy and consequently, thermal energy becomes sufficient to randomize the magnetic moments and cause magnetic instability. At this point, superparamagnetic limit has been reached and magnetic data is impossible to be stored. In order to keep up with fast areal density growth rates, magnetic storage technologies are advancing into new magnetic recording configurations such as bit patterned media or heat assisted magnetic recording in order to overcome the fundamental limit of superparamagnetism.

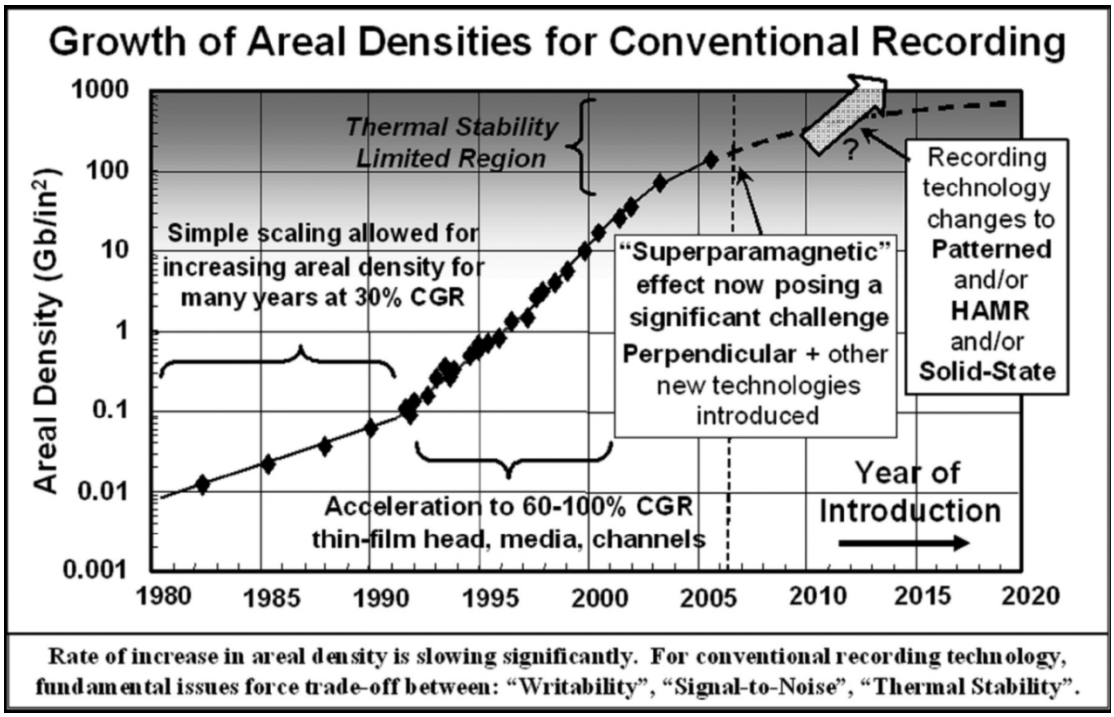

Figure 1-1: Growth of areal densities for conventional recording [3]

1.2 Components of Hard Disk Drive

The hard disk drive today is in the 1.8, 2.5 or 3.5 inch form factors with capacities ranging from 80 GB to 3 TB [2] at a cost of less than $0.50 per GB. The key components are the magnetic disk and the read/write head. Other important components include, spindle motor, voice coil motor (VCM), preamplifier and signal processing units, *etc*. Hard disk drive technology incorporates various aspects of engineering technology in servo, electronics,

mechanical, and materials as shown in Figure 1-2. Therefore, engineering system integration and instrumentation technology are paramount in HDD design and research.

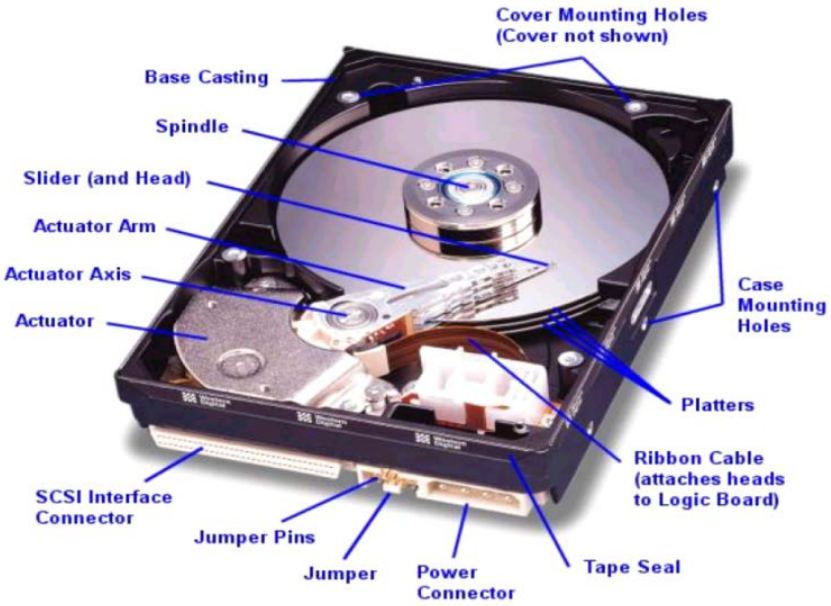

Figure 1-2: Components of a hard disk drive

1.2.1 Magnetic Media

The magnetic media consists of several layers of materials with one or more recording layers. The disk's substrate forms the bulk of the thickness which ranges from 0.635 to 1.7 mm. Thicker media adds to weight and stability which results in less non-repeatable vibrations. Today, magnetic recording media is granular and is composed of weakly coupled and randomly oriented ferromagnetic grains per bit cell. The first two layers are non-magnetic and provide mechanical and tribological durability of the head disk interface [5]. The lubricant acts as a complimentary mechanism of protection. It is made of a relatively high molecular weight linear polymer. The coating is usually monolayer thickness of several Angstrom and binds well to the surface of carbon atoms. A typical lubricant material is perfluoropolyethers with molecular weights of 2000 and more [5]. The diamond-like carbon

(DLC) layer is a few nm thick and provides the hardness that is necessary to prevent the damage of the magnetic layers and the consequent introduction of debris.

Textured surfaces are also desirable to provide improvements in magnetic characteristics in both circumferential and radial directions. However, continual increase in areal density demands for reduction in flying height means that the surface roughness needs to be minimal [6]. Since then, texturing is no longer implemented. The recording layer material is normally composed of Cobalt Chromium Platinum (CoCrPt) oxide-based hard ferromagnetic material [7]. Hard magnetic material possesses large coercivity and remanent magnetization. This layer is usually grown on top of an underlayer which acts as a seed layer and promotes the growth of the magnetic film in a desired orientation. In the advancement of longitudinal recording, anti-ferromagnetically coupled (AFC) media uses one or two coupling layers to stabilize the magnetization state of the recording layer [8]. In perpendicular recording, the soft underlayer (SUL) is added under recording layer which a soft magnetic material with high permittivity is used as virtual mirror of the recording head and to close the flux loop from the head.

1.2.2 Read and Write head

The read sensor, the writer coil, together with the air bearing surface (ABS) are fabricated together on a silicon wafer substrate. Till today, writing technology still remains inductive. Inductive writing uses electromagnetic induction by passing current through the write coil which induces a magnetic field over the soft magnetic pole and transfers magnetic flux onto a magnetic media. In longitudinal recording, a typical writing head would be a ring structure in which magnetic flux are produced across a gap parallel to the disk surface [5]. In this way, a horizontal fringing magnetic field is used to change the direction of magnetization on the media. In perpendicular recording, magnetic field is produced from a single pole

writing head coupled with an SUL. In this configuration, the media is virtually placed within the gap of a ring type head and a strong field in the direction perpendicular to the media surface is used to change the media magnetization [9].

In contrast to writing technology, the magnetic read head has evolved from inductive ring head to the present form of magnetoresistive thin film structure. Since the first implementation of giant magnetoresistive structures in the early 90s, GMR based sensor has been implemented in several spin valve configurations such as Current Perpendicular-to-Plane (CPP) or Current-In-Plane (CIP) GMR [10]. Together with the increase in areal density, reader sensors need to shrink and they need to be more sensitive. This brings about further research of new sensor structures such as Tunneling GMR (TGMR) or new materials with Colossal MR (CMR) [10]. Today, the dominant reader sensor uses TGMR technology which has much greater sensitivity than GMR.

1.3 Magnetic Recording Technology

Longitudinal recording has been used since the first invention of magnetic storage. In this configuration, the magnetization of bits is in the direction parallel to the media and the read head senses flux dominantly from bit transitions. Longitudinal recording has enjoyed tremendous growth in areal density up to 150Gb/in^2 in recent years despite the limit prediction by *S.H* Charap of 40 Gb/in^2 in year 1996 [11]. This achievement is made possible through rigorous head disk integration optimization and introduction of new media structures, such as the Anti-Ferromagnetic Coupled (AFC) media to stabilize the bits. Today, the industry has shifted entirely to perpendicular recording to meet the demand of higher capacities and in view of other advantages of perpendicular recording.

Perpendicular recording was introduced in late 1970s. Table 1-1 [12] summarizes the comparison between longitudinal and perpendicular recording. Since favorable magnetization

of perpendicular recording is in vertical direction, it is possible to grow smaller grain diameter and large volume thus maintaining thermal stability.

Table 1-1: Complementary relationship and performance-related features in HDD integration between perpendicular recording and longitudinal recording [12]

	Perpendicular	Longitudinal
Original findings of complementary relationship [13]		
	$\lambda \rightarrow 0$, Hd $\rightarrow 0$	$\lambda \rightarrow 0$, Hd $\rightarrow 4\pi M$
Head	Single pole-type	Dipole (Ring)-type
Medium	Perp. Anisotropy	Longi. Anisotropy
	Thick d	Thin d
	High Ms, High Hc	Low Ms, High Hc
Signal	Digital (Sat.)	Analog (non-Sat.)
Rec. Method	(FM, PCM)	AC Bias Method
Erase	DC Field	AC Field
Performance-related features in HDD integration		
Media	High squareness	Low squareness
	(Uni-axial orientation)	(Pseudo-2D random ori.)
	With soft underlayer	Recording layer only
Thermal	Good at high density	Good at low density
Stability	- Controlled by Hn	
Write Process	Medium in write flux path	Medium outside of path
	- Efficient writing	
	- High frequency writing	
	- Wide temperature range	
	Low spacing sensitivity	High spacing sensitivity
	- Relaxed spacing	- Narrow spacing required
	Sharp transition	
	Narrow erase band	
	- High TPI servo writing	
Read Process	High output	Low output
	- High SNR	
	- Good tracking servo	
	- Relaxed head sensitivity	- High head sensitivity required
	Narrow reading	Wide reading
Signal	With DC component	Without DC component
Channel	Positive coefficient PRML	Negative coefficient PRML

Lower demagnetization field can also be achieved with thicker recording layer. With larger thickness, media magnetic stability can still be maintained with smaller in-plane grain diameter according to (1.1) [8]

$$\tau = f_0^{-1} \exp\left(\frac{K_u V}{k_B T}\right), \qquad (1.1)$$

where τ is time constant of magnetic stability, f_0 is the magnetization reversal attempt frequency, K_u is magnetic anisotropy, V is unit volume, k_B is the Boltzmann constant and T is temperature.

Writing a higher coercivity media is necessary so that grain size can be further reduced. Due to soft underlayer (SUL) coupling, with the same write current and writer material in longitudinal recording, vertical head field is now doubled. The maximum fringing field in longitudinal ring head is $2\pi M_s$ and the maximum fringing field in pole head perpendicular magnetic recording is $4\pi M_s$ [9]. A larger pole thickness is good to achieve higher writing field. However, thick poles can cause recording problems at a skew angle.

Higher readback signal can be achieved compared with an equivalent longitudinal medium which improves signal-to-noise ratio (SNR). A high orientation ratio (in vertical magnetization direction) of perpendicular magnetic recording media also improves side-track writing and edge noise [7]. This is mainly due to pole head field which has predominantly vertical orientation and does not have any cross-track fringe structure. A sharp track edge enables higher density recording and a smaller bit aspect ratio. The write field gradient at the side edges of a recording head are usually sharper than is observed in longitudinal recording. This leads to better defined tracks and narrower magnetic transitions which improves thermal stability at high data densities [9].

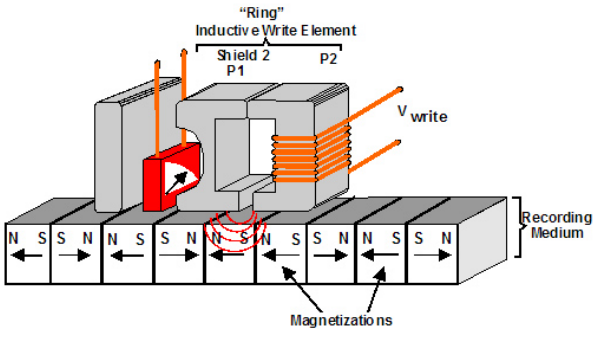

Figure 1-3: Longitudinal recording [77]

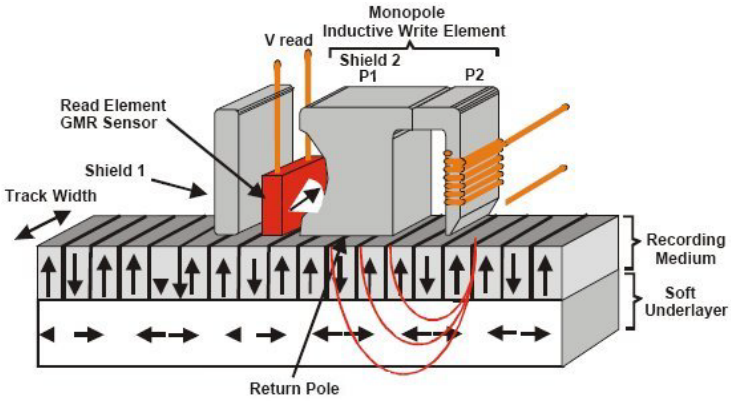

Figure 1-4: Perpendicular recording [77]

1.4 Slider and Head Disk Interface

The head disk interface (HDI) is often referred to as the separation region of head media system in a magnetic recording configuration. This region is of particular interest because it directly relates to the reliability of hard disk drives. An areal density of 1 Tb/in^2 in the near future expects medium thickness to be 15 nm and mean grain size to be reduced to 6 nm. This also means that reader width, gap length, and head medium spacing needs to be reduced further. According to the roadmap by the Information Storage Industry Consortium (INSIC) [13] in Figure 1-5, head media spacing should be reduced to 5 nm at 1 Tb/in^2 areal density. The term head media spacing refers to the sum of flying height (FH), head media overcoat thickness, and lubricant thickness. Head Diamond-Like Carbon (DLC) needs to be reduced to 0.9 nm, media DLC thickness to 1.1 nm, and lubricant thickness to 0.9 nm. Flying height refers to the sum of mechanical clearance at zero Pole Tip Protrusion (PTP) and glide avalanche as illustrated in Figure 1-6. Here, a 2 nm flying height needs to be achieved.

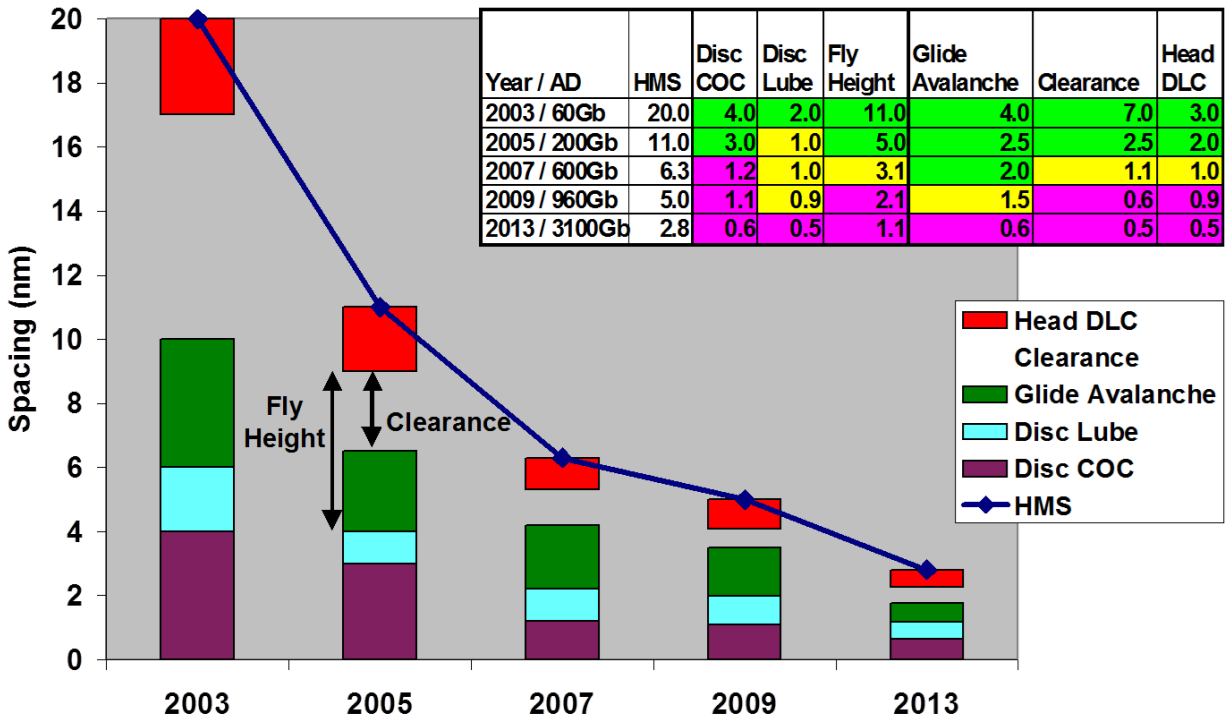

Year / AD	HMS	Disc COC	Disc Lube	Fly Height	Glide Avalanche	Clearance	Head DLC
2003 / 60Gb	20.0	4.0	2.0	11.0	4.0	7.0	3.0
2005 / 200Gb	11.0	3.0	1.0	5.0	2.5	2.5	2.0
2007 / 600Gb	6.3	1.2	1.0	3.1	2.0	1.1	1.0
2009 / 960Gb	5.0	1.1	0.9	2.1	1.5	0.6	0.9
2013 / 3100Gb	2.8	0.6	0.5	1.1	0.6	0.5	0.5

Figure 1-5: Head disk interface roadmap

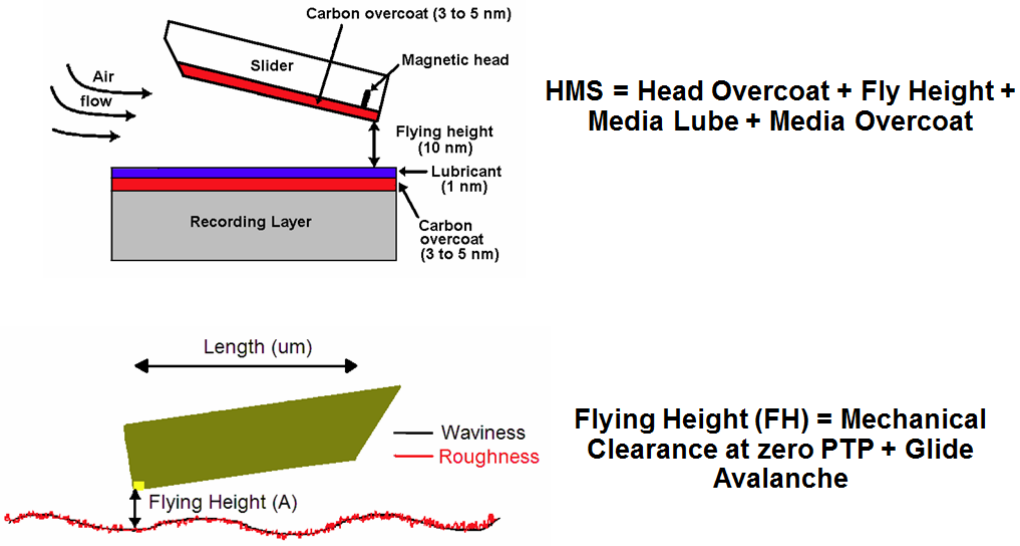

Figure 1-6: Definitions of head media spacing and flying height

As flying height reduces further, it is predicted that the head disk interface will shift to contact recording mechanism in Tb/in^2 era as shown in Figure 1-7. Regardless whether contact recording or flying recording is being implemented, critical concern lies in the stability of the interface. At such low flying height, physical phenomena such as

intermolecular forces, electrostatic forces, and tribocharging can cause problems in interface reliability.

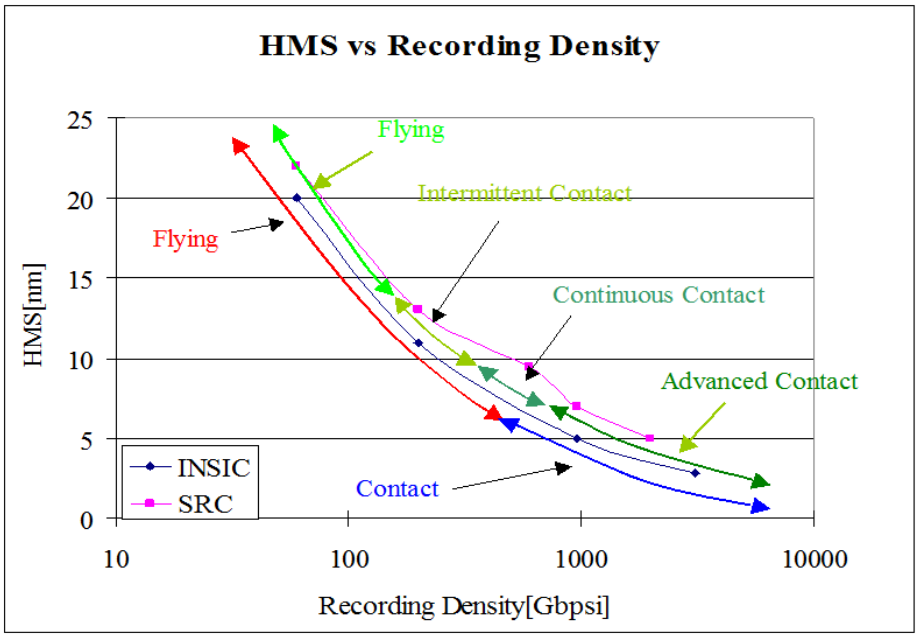

Figure 1-7: Head media spacing vs recording density and head disk mechanisms

From the tribological point of view, the slider-lube and the slider-lube-disk interactions are also the main concerns of head disk interface at such a spacing level. In view of these issues, characterization of head disk interface needs to be more comprehensive to eliminate spurious results. There exist excellent tools to characterize head disk interfaces. Unfortunately, they are all of specialized capability and functionality. For example, the optical fly height tester which measures flying height, laser Doppler vibrometer (LDV) which measures vibration, *etc*. This thesis focuses on the development of a new instrumentation system that integrates various testing methodologies to provide concurrent and comprehensive characterization of head disk interfaces. Therefore, one key areas of the research is on slider dynamics and stability. With the capability of the new system, new media certification methodology has also been developed. Finally, the last part of the work will be on the evaluation of tribocharging phenomenon, characterization, and impact on the slider flying dynamics. Tribocharging has been of paramount importance for ultra-low flying

sliders, as the presence of intermittent contact may induce tribocharging at the interface which has adverse effects on the reliability of the interface.

1.5 Thesis Organization and Structure

This thesis consists of six chapters with Chapter one being the introduction and Chapter 6 being the conclusion. In Chapter Two, head flying and contact performances in current literature are being reviewed. In Chapter Three, details on the development of the new integrated spinstand for head disk interface characterization will be described. This covers the major areas in electronics development, software development, as well as integration of slider disk positioning system. Chapter Four covers the applications of the new integrated system to new media certification method, followed by applications of concurrent methods of HDI measurements to characterize slider dynamics through touch down and defect interaction. In Chapter Five, tribocharge measurement of head disk interface is carried out using the integrated system. This chapter discusses in detail on setup development of an effective measurement system, electrical characterization methods of head disk interface, and on evaluation of tribocharging phenomenon through slider touch down and take off experiments.

CHAPTER 2: Methodology of Slider Flying and Contact Characterization

As hard disk technology is driven towards sub-5 nm slider disk spacing, head disk interface stability is influenced by physical phenomena such as intermolecular forces, tribocharging, and electrostatic forces. Moreover, the stiction effect becomes more significant when super smooth media are used with low glide height. At this level of ultra-low flying height, intermittent disk contact is inevitable and slider-lube-disk interaction becomes more intense. As such, maintaining slider's dynamic flying stability is a serious challenge. According to Brian *et al* [14], the slider's flying modulation should be within 10% or 0.5 nm variations at sub-5 nm flying height. In view of this, characterization methods of slider dynamics are crucial to facilitate further understanding of slider's behavior under different phenomena. This chapter discusses the slider's flying characteristics and causes of dynamic instabilities. We will also discuss various methodologies used by researchers to characterize slider dynamics. The chapter concludes with the review on tribocharging phenomenon and its impact on slider dynamics and interface reliability.

2.1 Sources of Flying Height Modulation

Slider flying stability issues have been one of the most critical causes of hard disk drives failures. With the implementation of thermal flying height control (TFC), read/write head is being protruded closer to disk surface using a heating transducer, hence effectively lowering the flying height to a desired level. With this implementation, it is possible to control the duration of ultra-low flying condition; only during read/write and to increase flying height during idle. This increases drive reliability while keeping the ability to lower flying height to sub-5 nm. Flying height variations can be caused by environmental effects

such as temperature and humidity, and dynamic flying modulations due to disk morphology such as disk microwaviness and disk clamping distortions. Compensation of these variations is possible if the disturbances are slower than the response time of the heating element [15]. For example, flying height change due to temperature can be computed according to pre-characterized sensitivity and appropriate heater power can be applied accordingly to maintain constant flying height. However, higher frequency flying height modulation is more difficult to compensate and therefore still poses a challenge to the thermal flying height control technologies.

2.1.1 Disk Morphology Effect on Flying Slider

Disk morphology refers to the profile of media surface. This profile ranges from sub-nanometer surface roughness, micro-waviness, and disk warping, *etc*. Sliders are designed to have high air bearing surface stiffness so that it can be resistant to low frequency disk profile changes. In other words, modern sliders are capable to follow low frequency disk run-out. However according to Ng *et al* [16], it can still be shown that at low flying height, fluctuations due to disk distortions are still present. The degree of flying height variation is strongly influenced by crown sensitivity of the air bearing surface (ABS).

Response of slider to surface roughness and microwaviness is not straightforward. Suk *et al* [17] found no correlation in slider's vibration frequency and surface roughness. Currently, many researchers are still actively studying the effect of high frequency morphologies due to micro-waviness on flying height modulations. These modulation frequencies usually range from 10 kHz to 500 kHz. In general, rougher media surface cause greater flying height modulation. Xu *et al* [18] measures vertical, pitch, and roll components of disk vibration and analyze the response of slider dynamics. Generally, pitch and roll components do not affect slider motion significantly. However among the three disks tested,

the slider amplifies the vertical topography of one disk sample. Zeng *et al* [19] correlated FH modulation by comparing measurement of disk topography and slider's dynamic response. It is concluded that FH modulation sensitivity depends very much on air bearing threshold for excitation due to disk morphology. The results of these studies are usually taken into considerations when designing new slider air bearing surface. It is to be noted that different slider's ABS design cause different excitation to disk's surface morphology and its selectivity on pitch or roll resonance.

In the application of thermal flying height control, Yuan *et al* [21] used real time in-situ flying height method to characterize dynamic flying height modulation and static surface microwaviness. The statistics of flying height modulation can be of importance to determining the appropriate margin for accurate and more reliable thermal actuation control.

2.1.2 Spindle Vibration and Disk Flutter

In a disk drive, the individual disk platter vibrates at its natural frequencies due to the internal windage excitation during rotation. This is commonly referred to as disk flutter. For high Track Per Inch (TPI) and high Revolution Per Minute (RPM) drives, disk flutter can be a critical issue since it can cause relative motion between data and servo heads. This causes track misregistration. As far as slider dynamics is concerned, disk flutter can also cause increase in dynamic flying height modulation. Figure 2-1(a) shows the FFT of raw LDV signal of a rotating disk along circumferential direction. Disk flutter measurements can be obtained by excluding the repeatable run-out (RRO) component of media topography. To obtain RRO, raw LDV data (which constitutes both RRO and NRRO) is averaged over several disk revolutions. Subsequently, the RRO FFT spectrum (with narrow peaks) can be removed from the FFT spectrum of raw LDV signal via subtraction to obtain the non-

repeatable component of disk vibration as shown in Figure 2-1(b). Disk flutter can then be analyzed from the processed data.

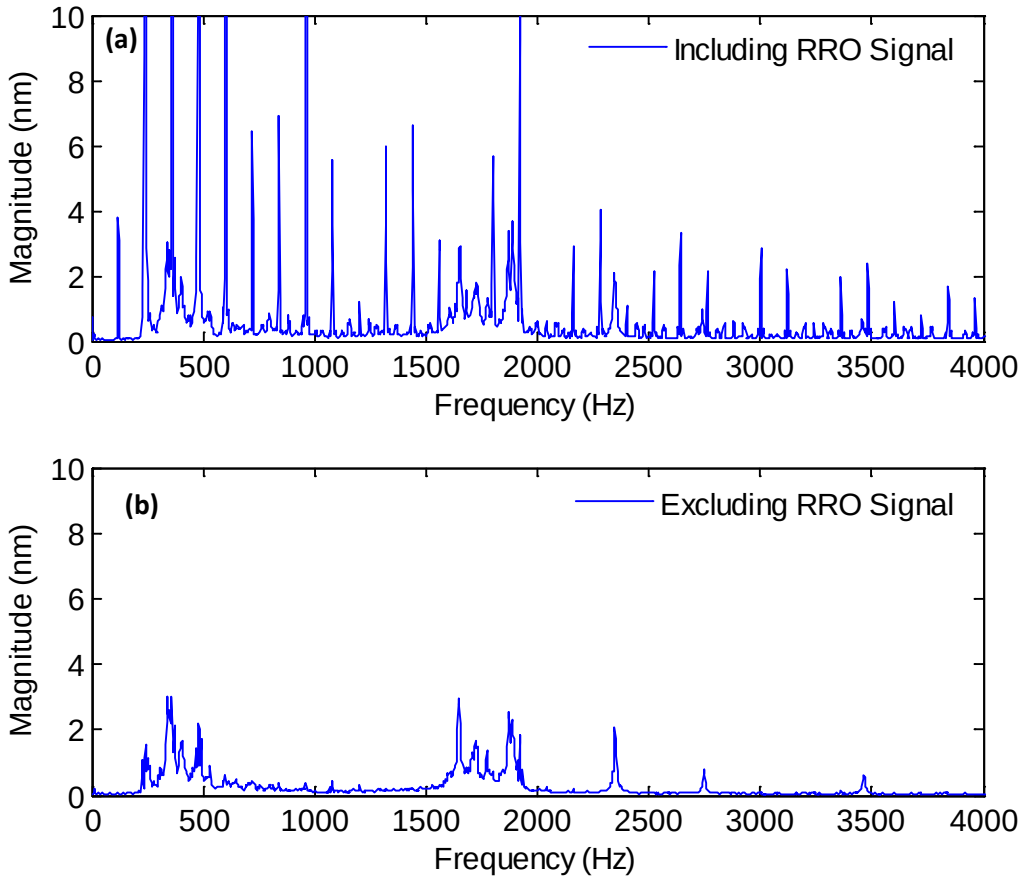

Figure 2-1: Disk flutter measurement

As shown in Figure 2-1(a), the narrow peaks correspond to the harmonics of repeatable mechanical distortions (RRO) due to the rocking mode of the spindle system as well as disk surface distortions due to disk clamping to the spindle. In most cases, the RRO frequency has very close correlation to the disk rotational frequency. This means that the periodic distortion is repeated at each revolution of the disk. In the case of 5400 RPM rotation, the RRO frequency is multiples of 90 Hz and in the case of 7200 RPM, the RRO frequency is multiples of 120 Hz. The spindle rocking mode is caused by unbalanced rotation about the rotating axis due to the deformation of spindle material or poorly designed fluid bearing which is the essential component to determine the dynamics of a spindle system. After

subtracting the RRO from the raw LDV signal, Figure 2-1(b) shows that the wide FFT peaks are components of disk flutter. According to Young *et al* [22], there is an interrelation between disk vibration and slider vibration. Figure 2-2(a) shows the FFT of disk flutter signal and Figure 2-2(b) shows the corresponding slider dynamics.

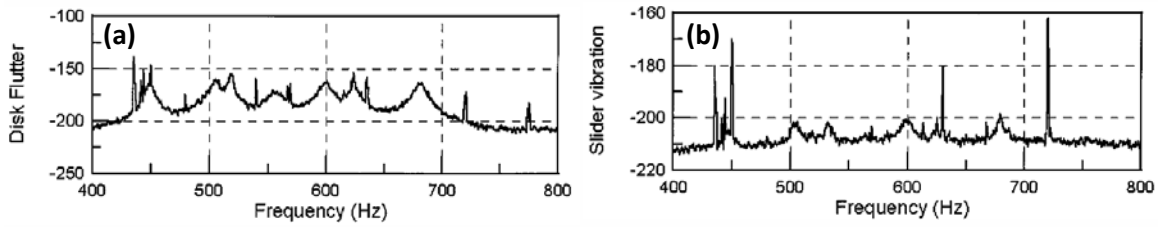

Figure 2-2(a): Disk flutter FFT
Figure 2-2(b): Slider dynamics in response to disk flutter

It is known that the disk flutter is dominated by disk material properties and geometry dimensions. Glass substrate is an excellent alternative material besides aluminum substrate for the disks, as it has significantly higher stiffness to density ratios which can dramatically reduce the amplitude of the disk vibrations. Generally, thicker substrate can help to increase the resonant frequencies of the disk and reduce the vibration amplitude.

2.2 Contact Induced Flying Height Modulation

Physical contact of slider to disk is undesirable. Intermittent contact causes slider flying vibration and instability, while continuous contact causes destructive damage to disk surface and eventually leads to head disk crash. In view this, detection of contact and characterization of slider flying dynamics is important. A typical characterization experiment will involve the detection of slider vibrations in time and frequency domains. Typically, the degree of contact will cause vibration frequencies to change. Therefore, the design of slider will involve some degrees of freedom so that when the slider flies on disk, it can orientate itself to the desired pitch and roll position. Naturally, a flying slider is perturbed with contact, and will vibrate with typical air bearing frequencies. The first pitch mode vibration is usually

lower than roll mode vibration and its frequency ranges from 0 to 500 kHz. In a typical experiment, TFC sliders are usually being used to lower the flying height and head disk contact is monitored using various measurement methods which will be discussed in the next section.

2.3 Methods to Characterize Slider Dynamics

The direct consequence of flying instability is slider disk interaction and the corresponding contact-induced slider vibration. In order to monitor these dynamics, researchers and engineers have used various techniques to characterize slider vibrations.

2.3.1 Laser Doppler Vibrometer (LDV)

The Laser Doppler Vibrometer (LDV) is a common tool used to measure slider vibration and disk topography. Laser Doppler vibrometry were used to study proximity of recording slider [14], in Knigge and Talke [23], and Liu *et al* [24]. A typical experimental setup involves using two measurement beams as shown in Figure 2-3. One measurement beam is applied on the disk and the other on the slider. Study of the use of LDV to measure flying height modulation with high resolution had been done by Zeng *et al* [19]. Kiely *et al* [25] used the reflected LDV laser signal from disk or media surface and sensed it using a photosensitive detector (PSD). In this way, angular changes of the surface can be obtained directly without interfering with vertical position change such that vertical, pitch, and roll vibration modes can be obtained simultaneously. Xu *et al* [18], extended the method to study a slider's off-track motion at both cross-track and down-track by using two additional LDVs. The study suggested that slider-lubricant interaction at the head-disk interface have a strong effect on slider dynamics.

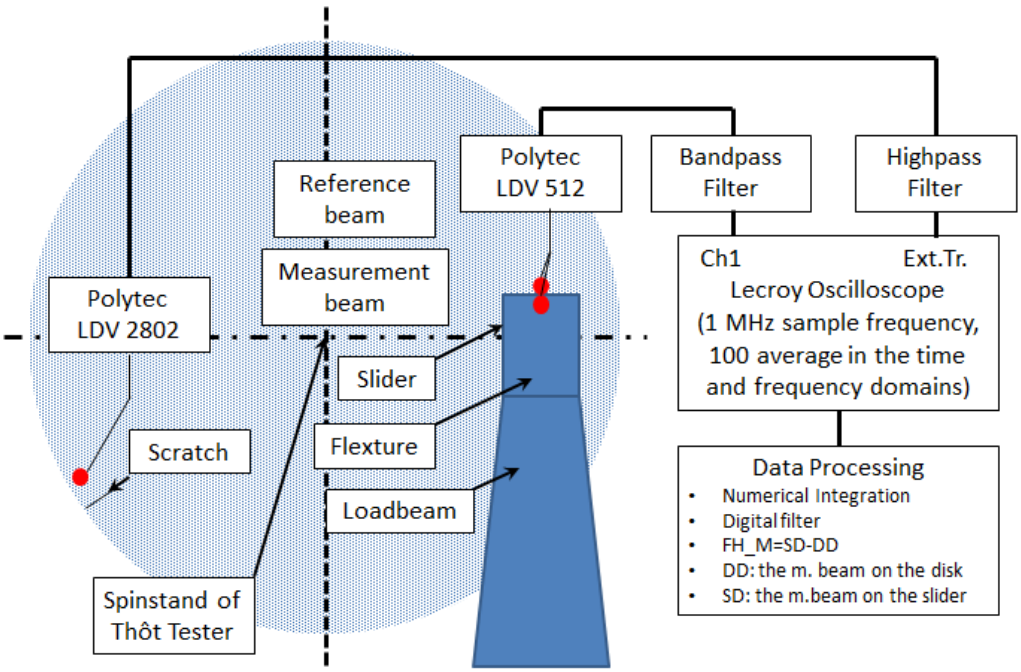

Figure 2-3: Experimental setup uses both reference beam on the disk and measurement beam on the slider

2.3.2 Acoustic Emission

Acoustic Emission (AE) sensors have also been widely used to detect contacts between the disk and slider. AE techniques are based on measurements of elastic waves propagating in solids from such sources as zones of elastic or/and plastic deformation, cracks, *etc*. An AE sensor consists of a Piezoelectric Transducer (PZT) that is attached near the source of elastic waves [26]. The use of AE sensor is usually implemented on a spinstand, where it is convenient to place a mini sensor very near to the head gimbal assembly (HGA) mount. Typically, the AE sensor's bandwidth ranges from 500 kHz to 1 MHz. The AE output signal can also be amplified by 20 dB or more. AE signal is usually monitored in time domain for sudden increase in amplitude root mean square (RMS) [27]. In a study by Zeng *et al* [19], if the measured AE signal shows slider ringing components in the frequency domain

or when the ABS resonance frequency starts to appear, one usually knows that contact has occurred.

For flying sliders, air bearing surfaces are designed to provide a stiff air bearing to help the slider maintain a small air gap between the head and disk and to avoid unjustifiable flying height (FH) changes. However, such an air bearing will produce high contact forces and is insensitive to friction-induced bounce and off-track motion of the recording head. In the past, AE has been a popular method to characterize slider dynamics. However, information provided by AE measurements alone is often not sufficient to study slider dynamics. One reason is because AE measurements cannot provide directional information. In this case, the LDV is preferred since the information obtained is usually vibrations in the direction of the laser beam.

2.3.3 Reader-Based Contact Detection

The amplitude of the readback signal is affected by head media spacing. If the head is flying higher, the amplitude of readback signal will decrease or vice versa. From this relationship, it can be inferred that contact starts to occur and induces flying height modulation, where readback signal modulation can also be observed as well. This modulation is often modeled by amplitude modulation with sidebands appearing near the readback signal frequency. One way to characterize readback signal modulation is by obtaining the readback signal envelope. This can be done by using a simple demodulation circuit and will be discussed in Chapter 4 of this thesis.

Temperature dependence of GMR/MR sensor's resistance can be used to detect contact and dynamics of slider. In general, the resistance of an MR sensor can be modeled by the relationship with temperature as [28]:

$$R = R_0(1+\alpha\Delta T) \ , \qquad (2.1)$$

where R_0 is the sensor-averaged resistance at ambient temperature T_0 and α is the temperature coefficient of R. This property of MR sensor has been extensively applied in detecting Thermal Asperities (TA) on disk media. Thermal asperity is an event registered when the MR read element of the slider touches the disk surface. Since this contact takes place at high speed, some element heating takes place (resistance of reader changes) and the baseline of the raw readback magnetic signal moves away from its normal position. Ramesh *et al* [29] builds TA sensors (similar to that of MR sensor) on sliders to enhance disk defect detection. In his experiments, the customized head with built-in TA sensor is also used to characterize disk run-out and contact induced vibration. Compared to other methods such as AE and LDV, it is found that TA sensor's sensitivity is limited to the slider's flying perturbation with MR sensor interaction.

Abraham [30] has modeled MR head's thermal signal with respect to head-disk spacing given by (2.2)

$$e(t) = C_0 + C_1\beta I^3 R^2 d(t) \ , \qquad (2.2)$$

where $e(t)$ is the MR thermal voltage, t is time, C_0 and C_1 are constants, b is the temperature coefficient of resistance, I and R are the MR bias current and electrical resistance respectively, and d is head disk spacing. It is shown by Gordon [31] that flying height measurement using thermal signal is less sensitive to track misregistration as compared to the conventional readback signal amplitude modulation. One limitation of this method is that the model is only valid when the flying height change is at least 50% of the nominal flying height of the MR head. This method is further explored by Leng *et al* [32] to characterize laser zone texture bumps uniformity in media manufacturing.

2.3.4 In-situ Head Media Spacing Measurement

When a slider vibrates or is perturbed, the head media spacing changes. One way to characterize slider dynamics is to monitor the head media spacing or the flying height. Phase Metrics' Dynamic Fly Height Tester (DFHT) has been widely used to measure steady and dynamic FH, but only with glass disks. Fly height modulation (FHM) should be measured on commercial media or real media. One cannot assume that FHM is the same over the actual magnetic hard disk with different surface topographies, lubricants, and other variables. In fact, FH should be measured with the slider flying over an actual HDD product disk. There are several methods in the literature to measure head media spacing. Klaassen *et al* [33] uses the readback signal pulse width at half maximum amplitude or PW_{50} to estimate spacing. This method is simple to implement but does not have a high sensitivity and accuracy. The readback signal pulse of a longitudinal recording mode can be approximated by a Lorentzian pulse which is given by

$$e(t) = \frac{e(0)}{1 + \left(\frac{2t}{PW_{50}} \right)^2}, \tag{2.3}$$

where $e(0)$ is the peak amplitude, t is time , and PW_{50} is the pulse width at half maximum amplitude. The PW_{50} can also be expressed as functions of head media spacing, head gap length, media thickness, and media transition length by the expression [5]:

$$PW_{50} = \sqrt{g^2 + 4(a+d)(a+d+\delta)}, \tag{2.4}$$

where g is the head gap length, a is the media transition length parameter, d is the head media spacing, and δ is the media thickness. W.K Shi *et al* [34] proposed a method of calculating change in head media spacing by using a readback amplitude change approach. In

this method, Wallace spacing equation for readback voltage amplitude of a sinusoidally recorded signal [35] is given by (2.5)

$$E = C\exp\left(-\frac{2\pi(d+s)}{\lambda}\right), \qquad (2.5)$$

where E is the amplitude of readback signal, C is a constant, d is head media spacing, l is the wavelength of recorded signal, and s represents the "virtual spacing variation" introduced by the non-uniform remanent magnetization and medium thickness. Note that E, s, d are functions of time or location. If the spacing variation is defined as $y = d - d_0$ and it is assumed that we ignore s and d_0 (an arbitrary reference spacing), from Wallace equation we will get

$$y = -\frac{\lambda}{2\pi}\ln\frac{E(d)}{E(d_0)} \quad . \qquad (2.6)$$

Subsequently,

$$\Delta y = -\frac{\lambda}{2\pi}\ln\frac{E(d(t_1))}{E(d(t_2))} = -\frac{v}{2\pi f}\ln\frac{E(d(t_1))}{E(d(t_2))} \quad . \qquad (2.7)$$

The drawback of the amplitude method is that variations of remanent magnetization, s, cannot be simply ignored as it can cause error. Moreover, if the written signal is not purely sinusoidal, the assumption in (2.5) will not be valid. This method is later extended to the harmonic ratio method where the ratio of two harmonics of readback signal will easily cancel the effect of non-uniform variation of media magnetic moment. In particular, Liu *et al* [36] had proposed the triple harmonic ratio method which could yield high sensitivity to spacing variation as compared to the conventional harmonic ratio method using all 1's pattern. The readback signal harmonic can be expressed as functions of spacing, media thickness and head gap length

$$E(k) = Ce^{-k(d+a)}\frac{1-e^{-k\delta}}{k\delta}\frac{\sin(kg/2)}{kg/2} \quad , \qquad (2.8)$$

where $E(k)$ is the readback signal harmonics, C is a constant, k is wavenumber, d is head media spacing, a is the media transition length parameter, δ is media thickness, and g is the head gap length. The head media spacing expressed by the triple harmonic ratio is given by

$$d = -\frac{3\lambda}{4\pi}\ln\left(\frac{E(k_1)}{E(k_3)}\right) + C \ , \qquad (2.9)$$

where $E(k_1)$ is the first harmonic, $E(k_3)$ is the third harmonic, C is a constant, d is head media spacing, and λ is the wavelength. The triple harmonic ratio method uses 111100 pattern to obtain two harmonics of almost equal amplitude and high SNR so that a more accurate flying height measurement can be obtained.

2.4 Tribocharging at the Head Disk Interface

Spurious charge build up at the head disk interface (HDI) is known as the tribocharging phenomenon. This has been a concern especially when there is direct contact of head and disk surface in either start or stop flying conditions. As flying height continues to decrease, tribocharging may also occur as a result of intermittent contacts. Tribocharging is the process whereby charges exist on a material after the parting of solid/solid or solid/fluid contacts [37] [38]. This phenomenon can lead to changes to the surface potential of slider or disk, which will induce attractive electrostatic force at sub-10 nm flying height (which is still valid since it is of a longer range as compared to Van-der-Waals force). This can lead to head-disk contact. Other consequences of tribocharging may include lubricant degradation [39], reader sensor damage [40], and contamination [41]. Therefore, it is important to be able to study and characterize the tribocharging process.

In studies by Feng *et al* [42] and Dae-Young *et al* [43], the intensity of tribocharging can be influenced by environmental factor such as humidity. It is found that tribocurrent is

higher at low humidities. Apparently, patches of water formed on surfaces due to high humidity help to suppress charge build up. Through experiments by Feng *et al* [42], it is also found that tribocharge intensity is affected by several aspects of HDI conditions. In a typical test, tribocurrent and AE are being monitored during slider take-off and flying. Take-off test is used to measure tribocurrent from head disk interface along with AE and voltage buildup is measured during flying. It is concluded that carbon overcoat with higher electrical resistivity and composition of carbon overcoat with higher hydrogenated carbon content will lead to higher tribocurrent. The level of tribocurrent also causes degradation of Femblin-Zdol lube type as it could start at electron energies as low as 3 eV [42]. In the later study, Feng *et al* [43] introduces an in-situ method of characterizing electrical charge at HDI using the readback signal pulse width, PW_{50}. In the study by Park *et al* [45] in Figure 2-4, tribocharge decay time is characterized by (2.10)

$$V \alpha \frac{V_0}{\sqrt{t}} \quad , \tag{2.10}$$

which shows that charge value V is inversely proportional to the square root of the slider's flying time, t. This interface property is important for the study of contamination build up due to electrostatic.

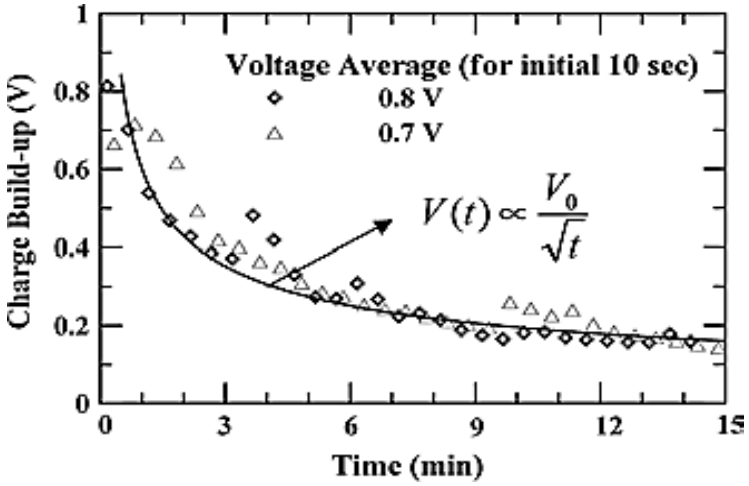

Figure 2-4: Tribocharge delay time, charge value is inversely proportional to the square root of the slider flying time [45]

CHAPTER 3: Setup Development for HDI Characterization

Currently, most head disk interface & tribology characterization methods are indirect, and each method shows part of the phenomenon. For HDI/tribology study, it is preferred to have multi-channel observations via different methods simultaneously, especially for a single transient process. One of the well-known testing platforms is the Guzik spinstand. The spinstand is a comprehensive platform to test the magnetic recording system at component level. It is dominantly used in component level testing in failure analysis laboratory, quality analysis laboratory, as well as recording tests and demonstration. As the areal density of HDDs approach 1 Tb/in^2, improved media testing and HDI characterization become more crucial. Currently, the industry uses two standard tools, namely the spinstand and the media certifier. These commercial testers usually provide limited testing functions as compared to the modified setups in research laboratories or universities, and may not be able to support concurrent testing functions as compared to the modified setups. As such, they are not able to support concurrent testing methodologies commonly applied for slider and head disk interface measurements.

Concurrent testing has been shown to be useful. For example, a combination of laser LDV and AE was used by Weissner and Talke [46] for studying the load/unload motion of a slider, and by Knigge and Talke [23] to measure slider dynamics and air bearing vibration. Yuan *et al* [47] combined the in-situ flying height measurement and AE to study slider's dynamic response to disk surface microwaviness. Recently, Liu *et al* [48] used AE and LDV to explore lubricant surfing recording. This work contributes to the development of a multifunctional media tester or a spinstand developed at the Data Storage Institute (DSI) [49], and in particular, on the author's efforts in tester integration, electronics, and software development. This tester is developed to close the gap between commercial testers and

laboratory modifications, while providing systematic and reliable testing with built-in support for concurrent testing and measurement. This provides a wide repertoire of functionality including tribocharge measurement, AE, Missing pulse, LDV, and in-situ FH measurement. This is in addition to the common magnetic read-back based measurements such as signal-to-noise ratio, track profile, missing extra pulse, thermal asperity, and other parametric tests, *etc*. The key strength of the system is the capability for concurrent measurement and mapping using a combination of the above functionalities. With the LDV probe mounted on the translation stage, systematic experiments to measure slider/disk vibration at any radius and skew combination are now possible without realignment of LDV as the LDV probe can now track the slider position without change in focus or alignment conditions. Such systematic and repeatable measurements are usually possible only on a custom-designed multifunctional tester.

3.1 Mechanical Integration of the Multifunctional Spinstand

The primary functionality of a spinstand is to integrate both head and media for magnetic recording tests. Basic components of a spinstand include an air bearing spindle, a load/unload bearing, a cartridge with Head Gimbal Assembly (HGA) mount, a set of head preamp electronics, head-positioning systems, *etc*. There are two types of air bearing spindles available. One is the aerostatic type; in which a separate external supply of air is fed under pressure between the two surfaces being kept apart, and the other is the aerodynamic type; where the separation of two surfaces is kept by a supporting thin film generated by the relative motion of two surfaces. If an external compressed air supply is available, the aerostatic air bearing spindle is preferred due to its high reliability. However, the constant supply of air must be kept clean from contamination. This is done using an air filter and the air pressure must be kept constant using an air pressure regulator, typically with a pressure range between 5 to 7 bar.

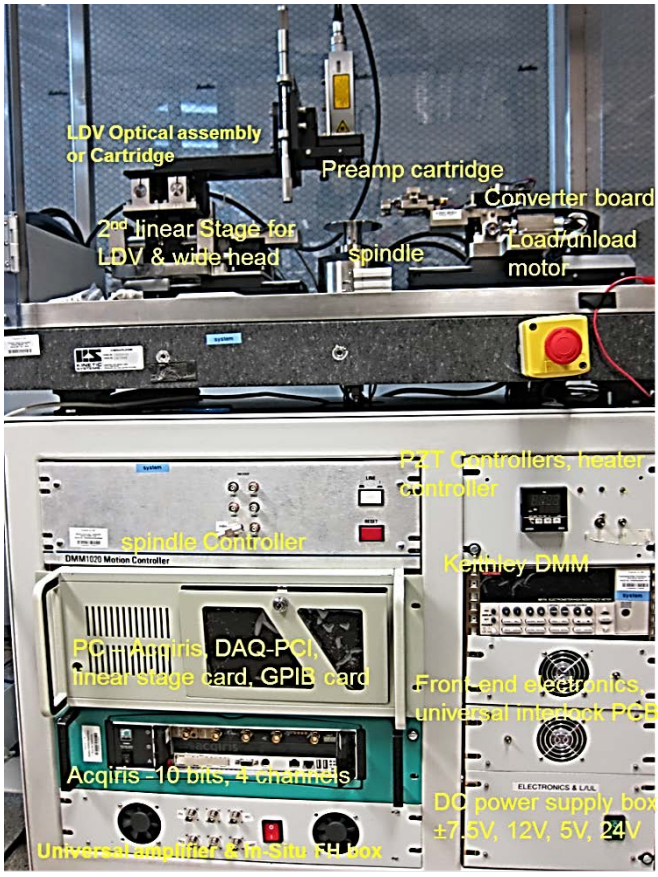

Figure 3-1: A multifunctional spinstand

Two M505 linear translation stages manufactured by Physik Instrumente are used to position a slider in Cartesian coordinates. These linear stages are driven by DC electric motors and have a coarse travel resolution of 100 nm, with maximum achievable travel velocity of 3 mm/s as well as a maximum travel range of 100 mm. The positions in HDD are in polar coordinates and the slider is attached to an actuator arm which also moves according to the magnitude and direction of current flow in the voice coil motor (VCM). Head position in HDD is usually specified according to parameters such as the radius and skew angle.

Figure 3-2 shows the polar coordinates positioning system which is now used in hard disk drives.

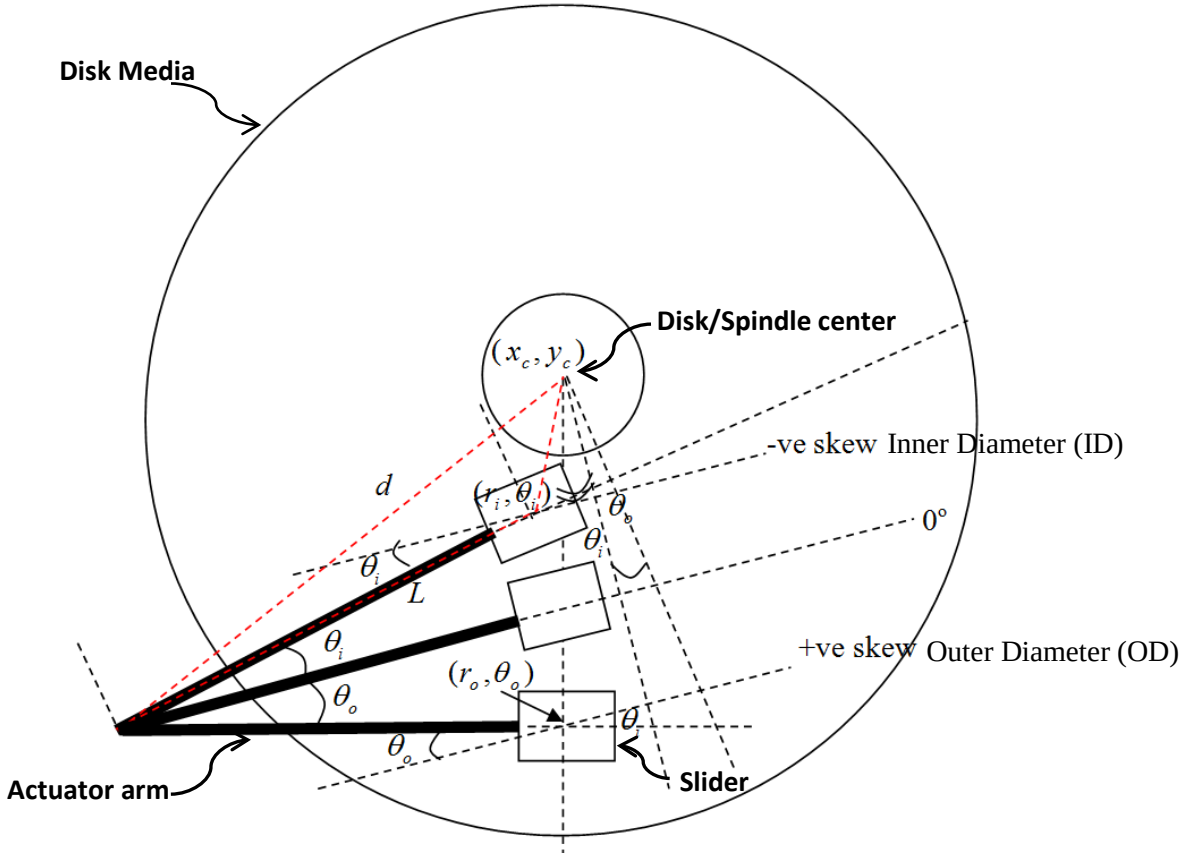

Figure 3-2: Polar coordinates system in a hard disk drive

where, (x_c, y_c) is the center coordinates of disk or spindle chuck, d is the length of actuator arm (from VCM) to rotational center (motor spindle center) of magnetic media, L is the length of actuator arm, r_i is the inner diameter (ID) radial position from the center of the disk, r_o is the outer diameter (OD) radial position from the center of the disk and θ_o is the positive skew angle and θ_i is the negative skew angle. If d and L are known parameters, the skew angle can be easily determined by cosine rule using the radius location of the slider.

In the development of tester using linear stages, we need to be able to simulate the positioning of slider as that in a HDD. Therefore, input control parameters are specified in

polar coordinates (r, θ). The Cartesian coordinate positioning of the tester is illustrated in Figures 3-3 and 3-4.

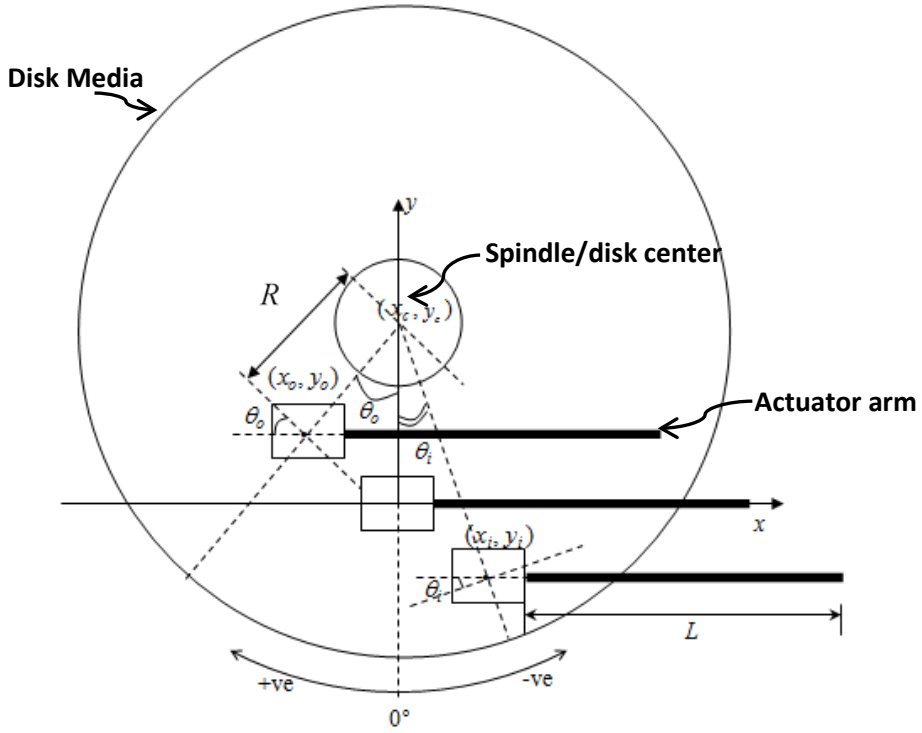

Figure 3-3: Cartesian form of positioning on a multifunctional spinstand

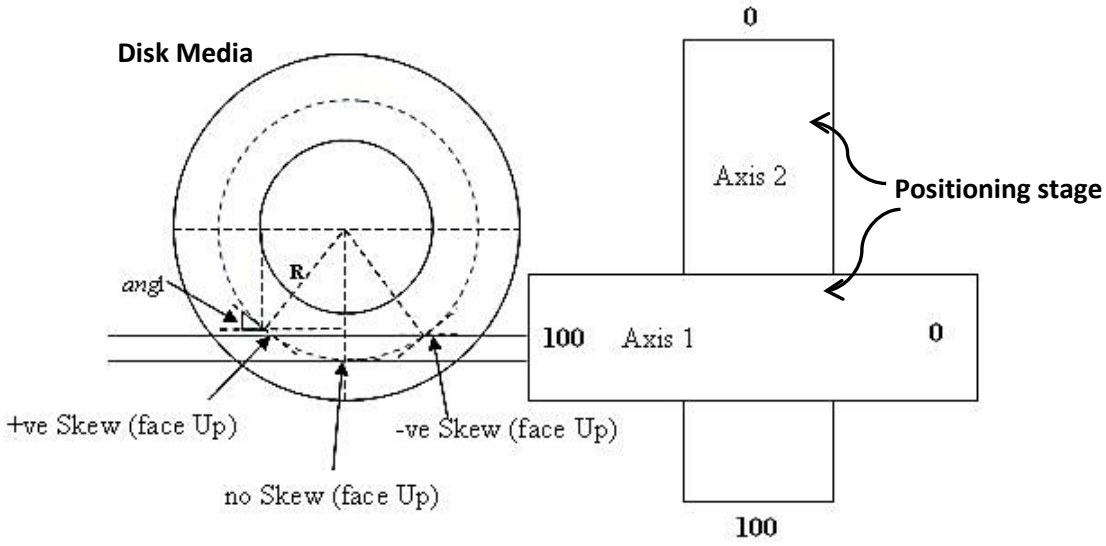

Figure 3-4: Schematic of linear stages position with respect to media

Conversion of polar coordinates to Cartesian coordinates is given by equations (3.1) and (3.2):

$$x = (x_c - L) + R\sin\theta, \tag{3.1}$$

$$y = y_c + R\cos\theta, \tag{3.2}$$

where (x_c, y_c) is the center coordinates of disk or spindle chuck, x is axis 1 position (as shown in Figure 3-4), y is axis 2 position (as shown in Figure 3-4), L is the length of actuator arm, R is the position of slider in terms of radius of magnetic media, and θ is the skew angle. From (3.1) and (3.2), it is clear that (x_c, y_c) needs to be determined. Figure 3-5 shows the setup to determine the position of media or spindle center coordinates (x_c, y_c) relative to the position of linear stages. A camera is positioned perpendicular to the plane of the disk media and guiding lines are drawn within the acquisition window to align the edge of the cartridge body to the spindle center. The alignment procedure can be carried out by controlling the position of the linear stages. When the edge of the cartridge body aligns well with the guiding lines, the values of the center coordinates are recorded.

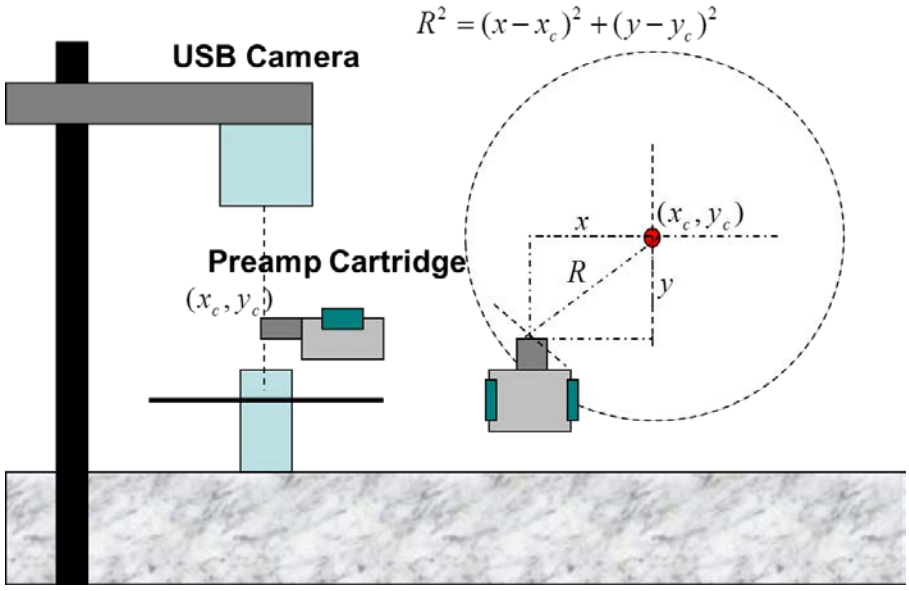

Figure 3-5: Determination of centre spindle coordinates using a USB camera

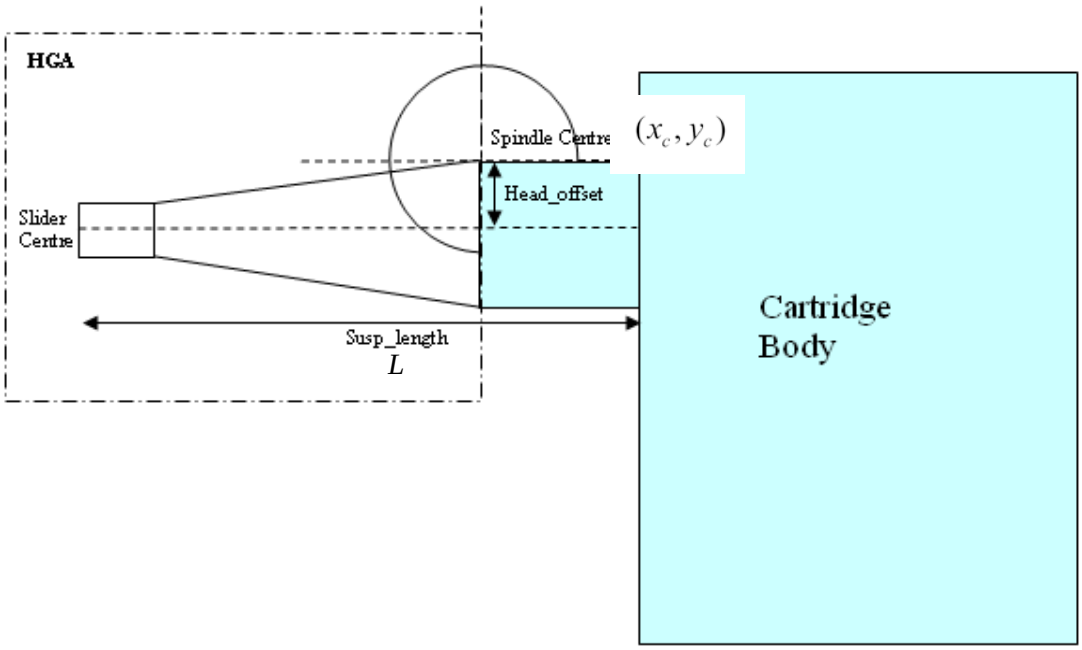

Figure 3-6: Alignment of cartridge body to the spindle center (x_c, y_c)

Figure 3-6 shows the structure of slider mounting cartridge body and Figure 3-7(b) shows the integration of cartridge body with the tester system. Since the reference of the spindle center coordinates (x_c, y_c) is relative to the edge of the cartridge body's slider mount structure, head offset needs to be considered in the calculation of the slider center position. The head offset only affects the y-axis positioning, therefore (3.2) is revised as

$$y = y_c + R\cos\theta - \text{Head\_offset}, \qquad (3.3)$$

where y_c is the center y-coordinate of disk or spindle chuck, y is the position of axis 2 (as shown in Figure 3-4), R is the position of slider in the form of radius of magnetic media, θ is the skew angle, and Head_offset is the distance from the edge of the cartridge body's slider mount structure to the slider center.

Fine-positioning in cross-track direction is crucial to implement track scanning functions such as the track profile. At a track width of 100 nm and below, positioning resolution must be of the order of 5 nm and below to achieve optimum accuracy with

minimal backlash. Therefore, positioning at this resolution is achieved using controlled deformation of piezoelectric transducer. Piezoelectric transducer used in our system is P752 single axis nano-positioning stage with a travel accuracy of 0.1 nm and a travel range of 15 µm. This is shown in Figure 3-7(a).

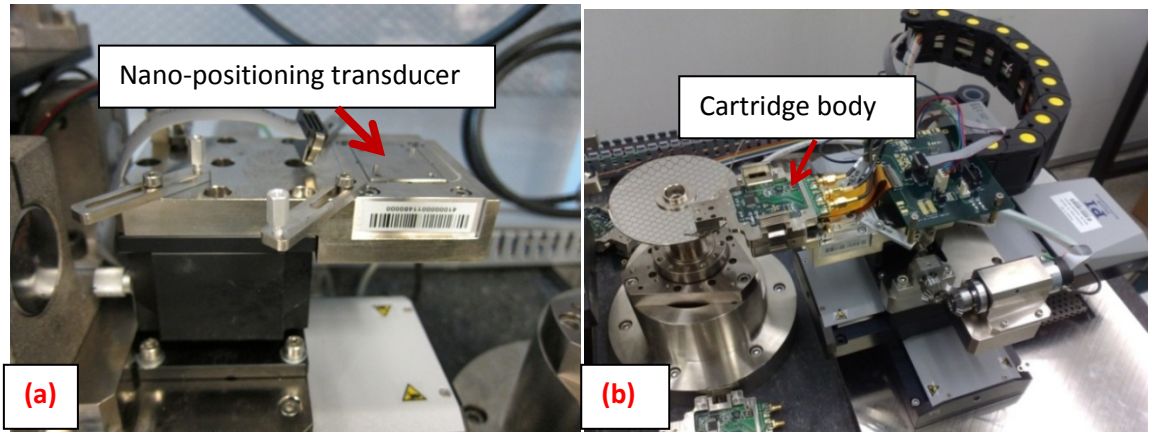

Figure 3-7(a): Piezo transducer P752

Figure 3-7(b): Spinstand platform

As shown in Figure 3-8(b), the vertical load/unload system is implemented using a DC motor with controlled load/unload speed. The DC motor drives a rotational motion of two gears which interfaces with an oval cam and subsequently lifts or lowers the cartridge body mount.

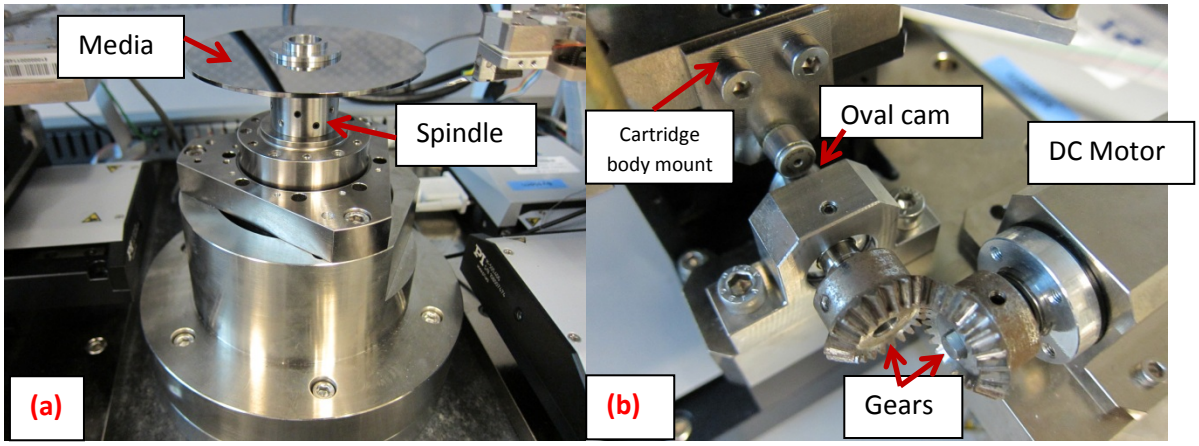

Figure 3-8(a): Media and spindle
Figure 3-8(b): Load unload system

Components for signal processing include data acquisition system manufactured by Acqiris Systems, National Instruments, and a universal amplifier electronics module.

Table 3-1: Measurement modules for HDI characterization

	Specification	Probe Location	Nature of Test
Acoustic Emission	Probe bandwidth: up to 574.22 kHz	Attached to cartridge fixture side just above the HGA suspension mount	Mechanical vibration detection
LDV	OFV-2700 50 nm/V, 20 MHz displacement decoder	Measurement beam shines directly on media or slider flexure	Surface topography change (media defect, media runout), slider vibration and dynamics
Readback Envelope	80 MHz envelope resolution	Reader-based	Magnetic readback envelope, head medium spacing change, missing pulse
In-situ FH	Measurement frequency: 90 MHz	Reader-based	Triple harmonic, head medium spacing change

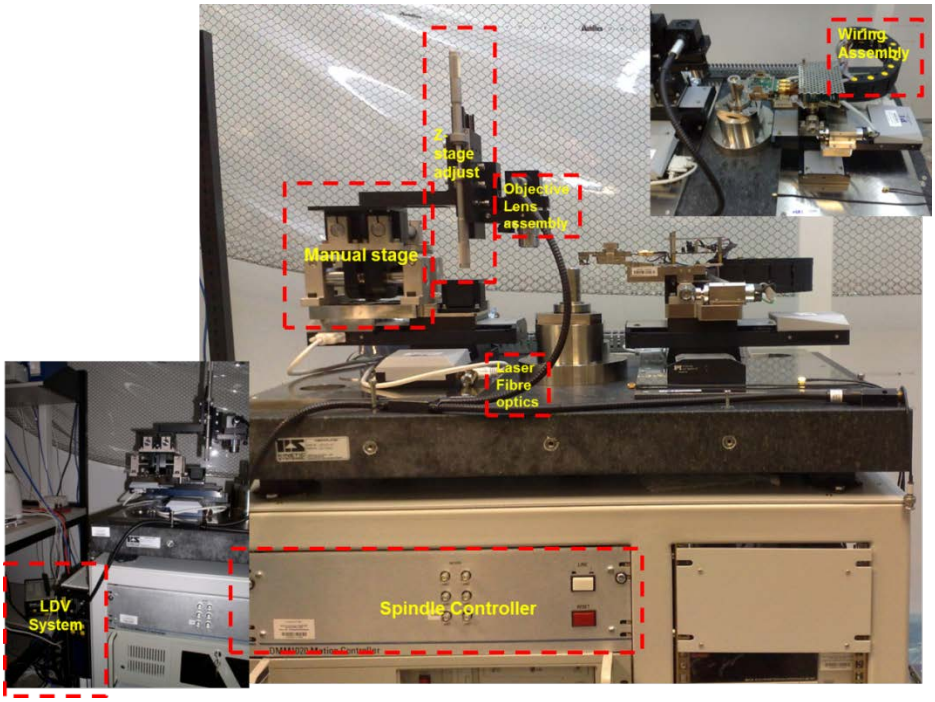

Figure 3-9: LDV system integration on spinstand

Other modules such as the LDV system (as shown in Figure 3-9), the acoustic emission sensor, and the in-situ FH measurement module facilitate a more comprehensive characterization of the head disk interface. A summary of these modules is given in Table 3-1 and further details of this work are discussed in Chapter 4. Read/write testing is performed on a commercial media with ring head writer and TGMR reader. Figure 3-10 shows a commercial perpendicular media with pre-written all 1s pattern at 68 MHz. Figure 3-11 shows that the pre-written track is successfully overwritten with all 1s pattern at 40 MHz and 56 mA writing current.

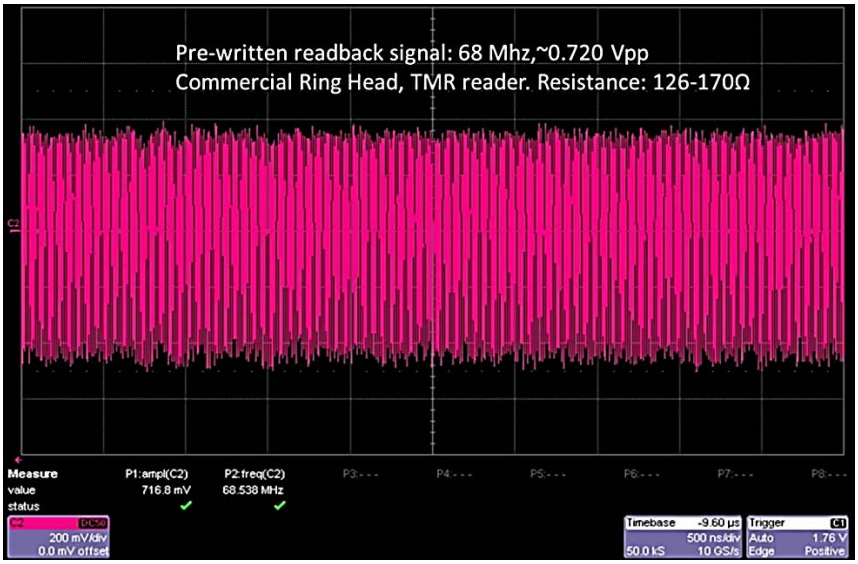

Figure 3-10: Pre-written data on commercial medi

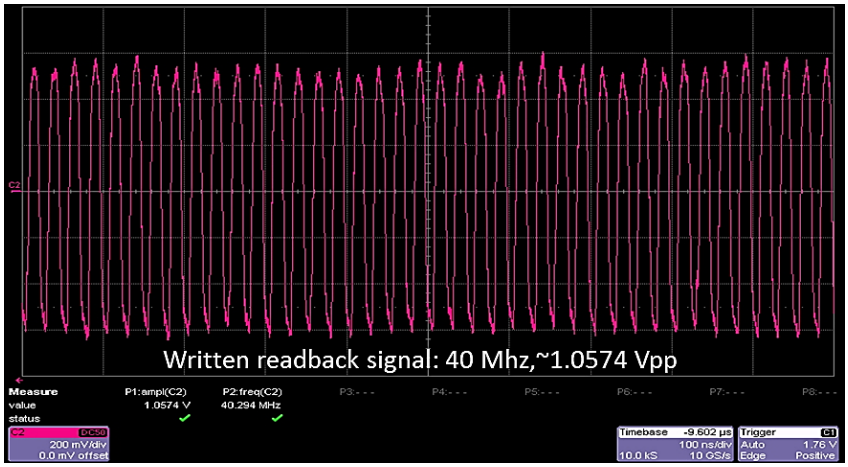

Figure 3-11: Overwritten data with 40 MHz all 1s pattern

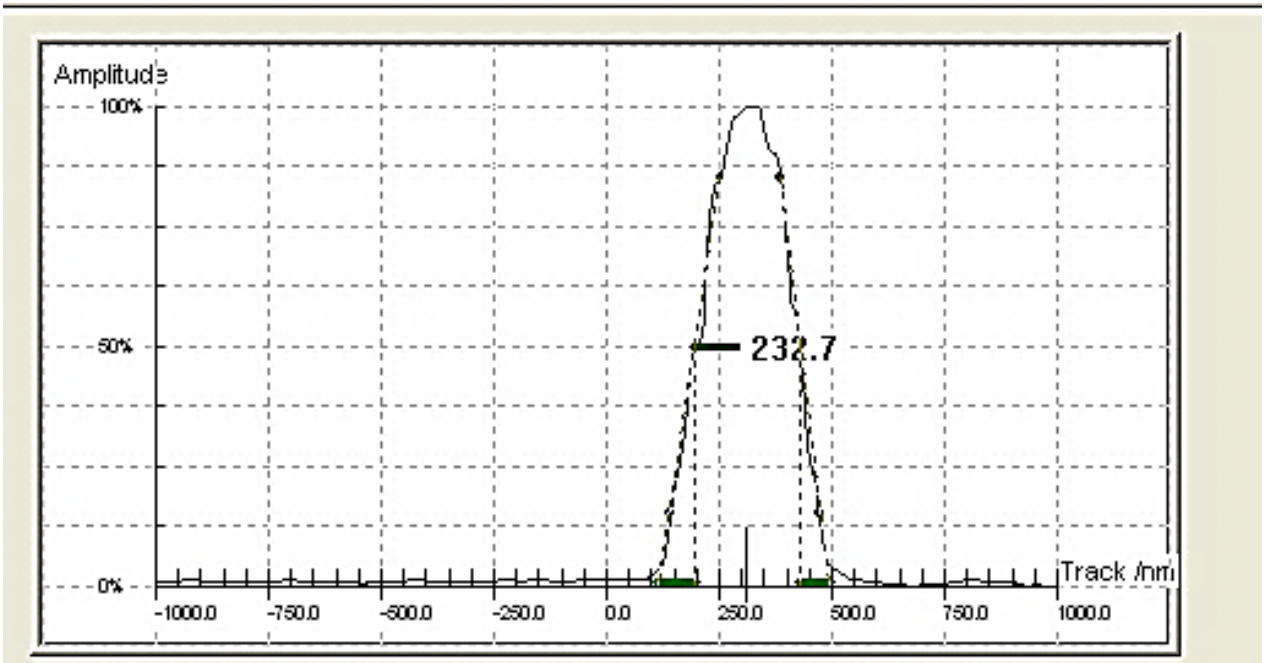

Figure 3-12: Track profile

Figure 3-12 shows a track profile measurement with measured magnetic read track width of 232.7 nm.

3.2 Electronics Development

3.2.1 Head and Preamplifier

A commercial preamplifier provides the capability to supply current or voltage to various transducers in the read/write head. The preamp is integrated on a PCB board as shown in Figure 3-13 and Table 3-2 lists the key specifications of the preamplifier.

Table 3-2: Preamplifier specifications

Read	- Current or voltage biasing - 6 bit programmable voltage (40 mV – 180 mV) bias - 6 bits programmable (95 µA – 3 mA) current bias - MR resistance 60 – 500 Ω - Read BW: 500 kHz to 1 GHz (min), 3 bits programmable.
Write	- 4 bit programmable write current (10 mA – 60 mA) - Programmable writer current overshoot and duration.

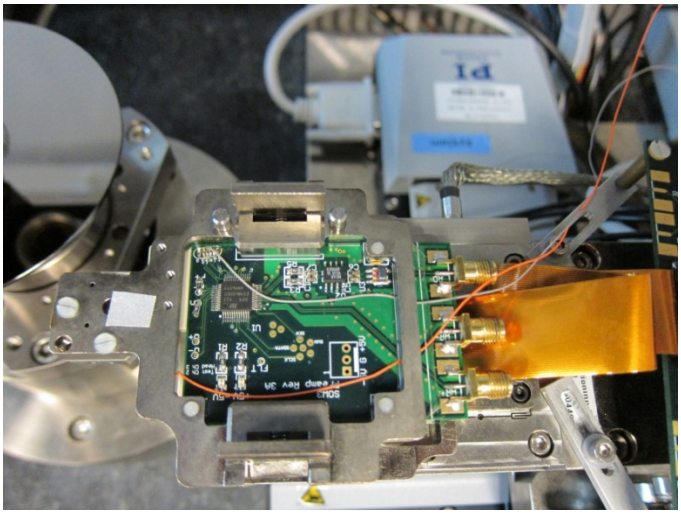

Figure 3-13: Preamp electronics PCB and cartridge

Preamplifier control is implemented through the serial communication port via a microcontroller unit (MCU) and 16 bits of SDATA are being sent together with SCLK and SEN to form Serial Peripheral Interface Protocol (SPI). As shown in Figure 3-14, programmable digital-to-analog converters (DAC) form major building blocks of a preamplifier. The analog outputs of the DACs are buffered to supply sufficient current drive to the transducers.

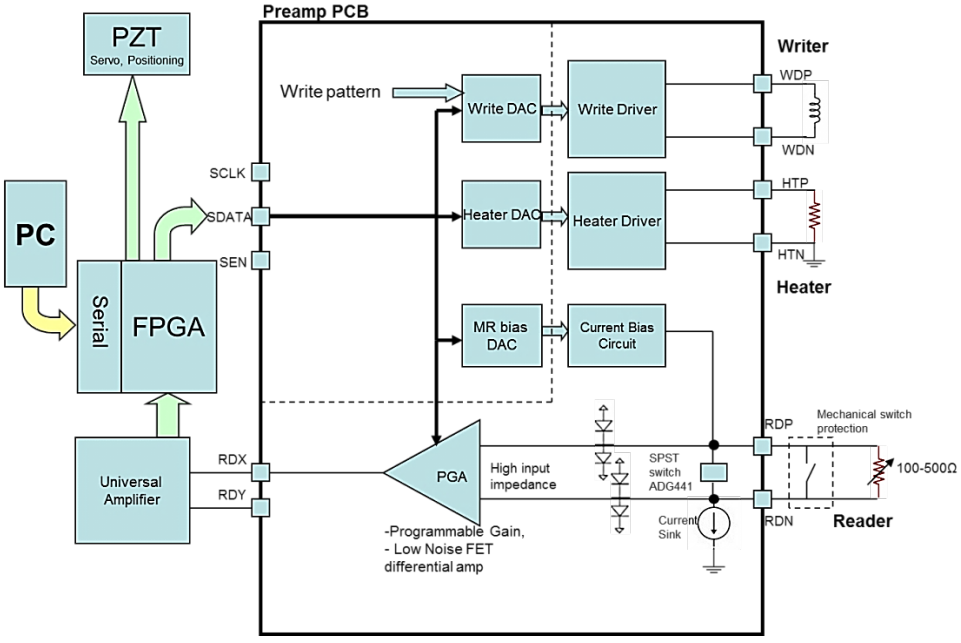

Figure 3-14: Schematic of preamplifier functional blocks

3.2.2 Universal Amplifier

The readback voltage obtained from GMR head sensor approximately ranges from 10 to 20 mV (stronger for TGMR head). In order to implement signal processing for further application, it is crucial to be able to provide enough signal amplification. Figure 3-15 shows a basic schematic of a hard disk drive system. The readback signal is amplified using a pre-amplifier which is attached to the end of the head stack suspension before being passed to the signal processing electronics (read channel detection and servo module).

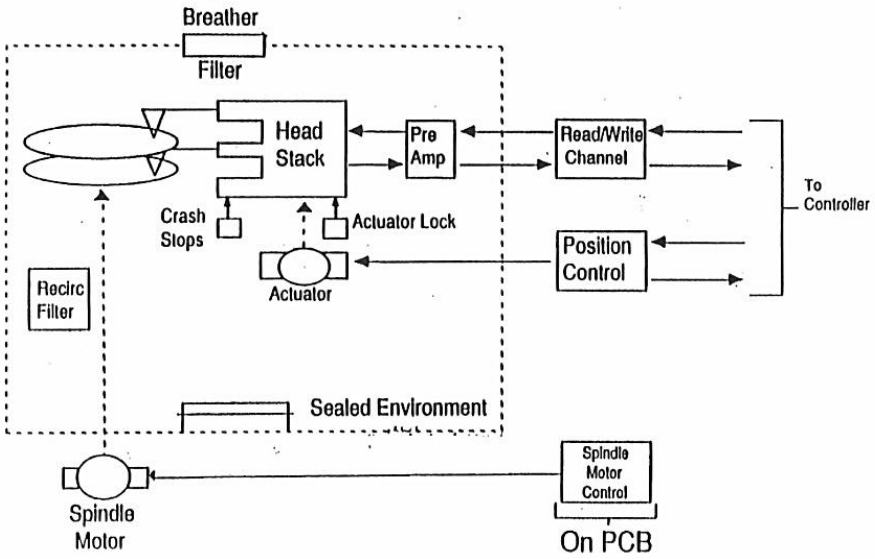

Figure 3-15: Schematic diagram of basic hard disk preamp, actuator and motor inside the hard drive

The multifunctional spinstand focuses on HDI related failures which include TFC power calibration and contact detection, media defect mapping or Thermal Asperity (TA) mapping, SNR measurement, as well as tribocurrent measurement. Though most of the above-mentioned failures are physical in nature, they can be detected through the observation of the readback signal. For example, the presence of a TA produces sudden surges or hikes in the readback signal possibly due to heating of the MR sensor. This will then cause an extra pulse beyond the normal peak-to-peak signal level as illustrated in Figure 3-16.

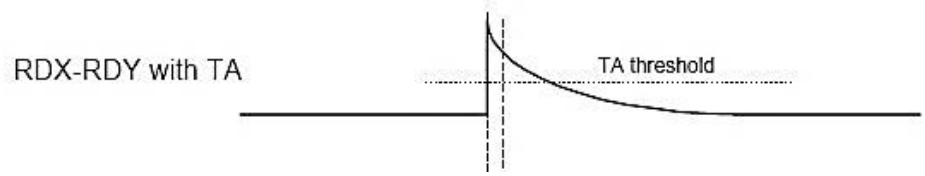

Figure 3-16: Readback signal of TA with threshold indication

To provide multiple signal channels for various functions, it is necessary to design a signal splitter. Generally, the preamp PCB has an amplifier with voltage gain of around 30-40 dB, which amplifies the signal by approximately 100 times. This implies that the readback signal produced by the preamp is approximately 200 mV peak-to-peak. The designed amplifier cum signal splitter is expected to provide enough amplification and at the same time, to avoid signal saturation. For general amplification purposes, either operational amplifiers or differential amplifiers can be used depending on the type of input requirement - single or differential inputs, respectively. The gain of the amplifier can usually be tuned by changing the value of the feedback resistor.

Operational amplifier is an analog device used primarily to perform mathematical operations such as addition, subtraction, *etc*. Operational amplifiers can also be used as building blocks in the construction of complex circuitry such as active filters. In general, operational amplifiers are differential amplifiers which ideally have the characteristics of infinite voltage gain, infinite input impedance, and zero output impedance. The extremely high open loop gain of an op-amp creates an unstable situation because a small noise voltage on the input can be amplified to a point where the amplifier is driven out of its linear region. As such, op-amps are operated with negative feedback to stabilize the gain and increase frequency response.

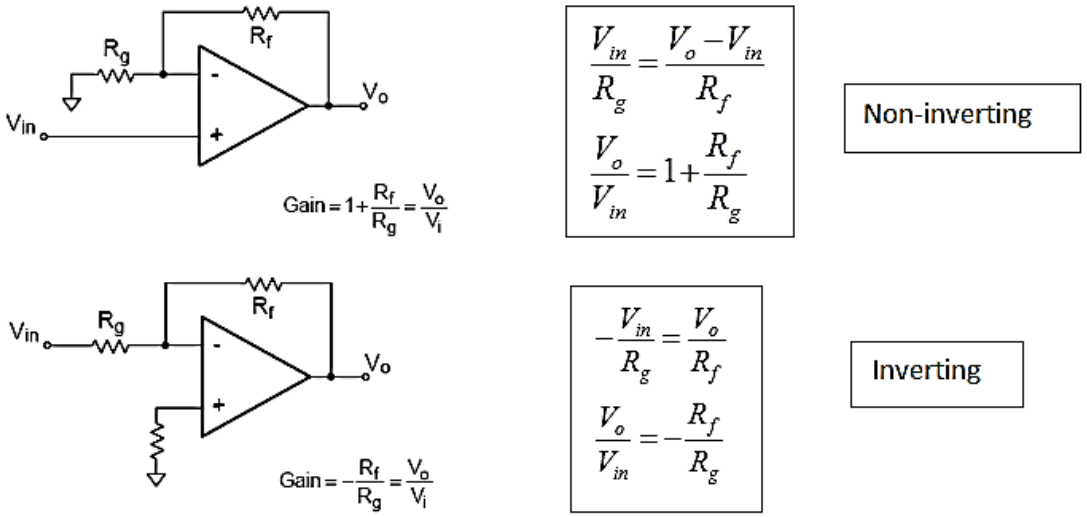

Figure 3-17: Inverting and non-inverting op-amp configurations

The difference between the utilization of current and voltage feedback amplifiers are not apparent in a design. Depending on the requirements of the circuit, either current or voltage feedback amplifiers may be utilized. In general, voltage feedback amplifiers have lower noise, better DC performance, and feedback freedom. On the other hand, current feedback amplifier has faster slew rates, lower distortion, and feedback restriction. When analyzing its open loop response, gain-bandwidth independence is a major advantage of the current feedback amplifier as compared to its counterpart. This implies that it is possible to get high gain and good bandwidth with current feedback amplifiers. In voltage feedback amplifiers, gain and bandwidth have to be compromised due to its constant gain bandwidth product.

Figure 3-17 shows the inverting and non-inverting configurations of operational amplifiers. The closed-loop topology for current feedback and voltage feedback designs are similar. However, the value of feedback resistor is limited for current feedback amplifier and is usually specified in the datasheet. The op-amp typically consists of two or more differential amplifiers. Differential amplifier is a simple transistors circuit which is able to amplify small

signals applied between its two inputs while achieving good Common Mode Rejection Ratio (CMRR). The schematic of a differential amplifier is illustrated in Figure 3-18.

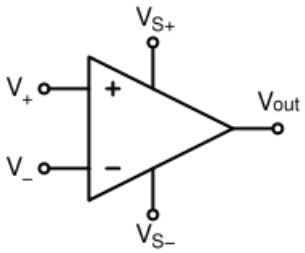

Figure 3-18: Differential amplifier

The output voltage of a differential amplifier is given by (3.4)

$$V_{out} = A_d (V_+ - V_-) + A_C \left(\frac{V_+ + V_-}{2} \right), \qquad (3.4)$$

where V_{out} the output voltage of the amplifier, V_+ is the positive input terminal, V_- is the negative input terminal, A_d the differential gain and A_c is the common mode gain. Each of the critical function needs to be supplied by one channel of amplified signal. Hence, the general layout of the circuit is shown in Figure 3-19.

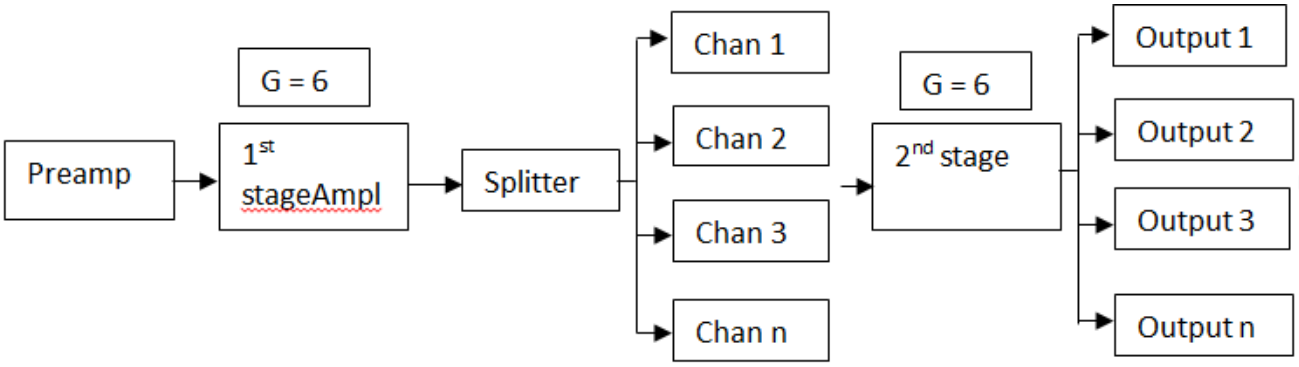

Figure 3-19: Block diagram of universal amplifier schematic outline

Due to the impedance matching at the splitter input, the effective overall gain is equal to 3. The choice of amplifiers requires a -3 dB bandwidth greater than 500 MHz in our application. Three boards are designed using these 3 types of amplifiers.

3.2.2.1 Design using AD8350

The AD8350 is high performance differential amplifier that has a wide bandwidth operation of up to 1000 MHz, and is even suitable for RF circuit design. It is available in two gain versions: G = 15 dB and G = 20 dB and input/output resistance of 200 Ω. Figure 3-20 shows the frequency response of AD8350. The left chart shows the characteristics of device with gain of 15 dB and the right chart shows the characteristics of device with gain of 20 dB. It is observed that frequency response is better with higher power supply level, but with greater overshoot. Higher gain overshoot is not desirable in our design and power supply of 5V is used. The characteristics of input and output impedance with frequency correlate with the overall frequency response of the system.

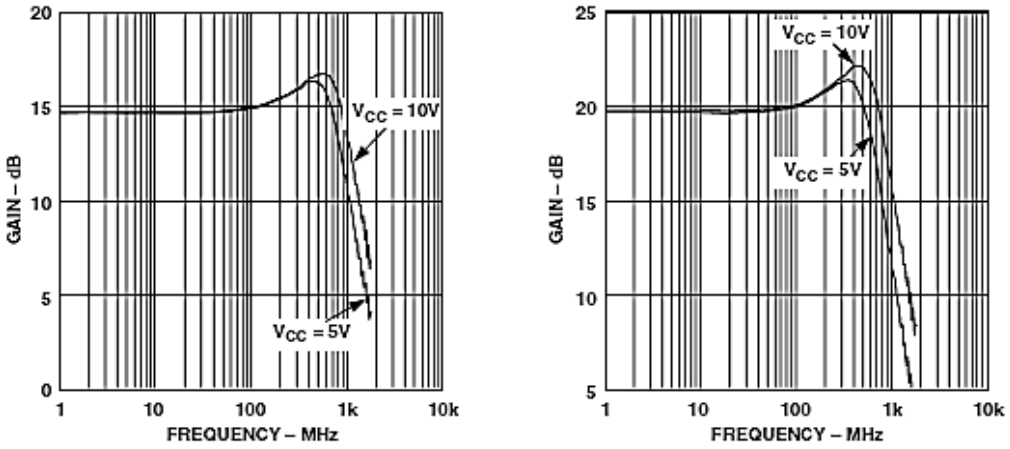

Figure 3-20: AD8350 gain vs frequency charts [74]

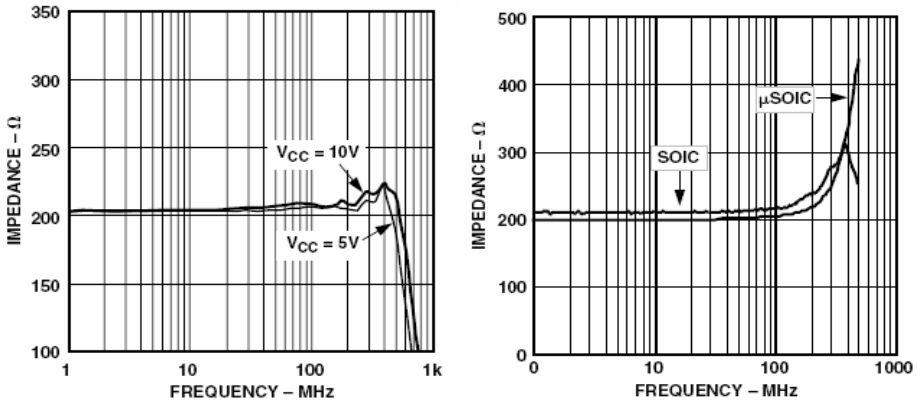

Figure 3-21: AD8350 input (left) and output (right) impedance vs frequency chart [74]

Figure 3-21 shows the characteristics of input and output impedances of AD8350 with respect to frequency. In our design, a typical input/output impedance interface is 50 Ω. The consideration of maximum power transfer is crucial in any circuit's design (where interfacing between source and load is involved). Maximum power transfer theorem requires that the resistance of the load must be equal to the resistance of the source. This is called impedance matching between the source output and load input impedances.

Impedance mismatch in RF circuits creates a more complex problem, particularly due to the propagation of waves in transmission lines. If there is a mismatch in source and load impedance, reflection of waves can occur and may cause interference of the transmitted signal, *i.e.*, power loss. Most commercial amplifier chips have typical input/output impedance of 75 Ω or 150 Ω that is used in typical video applications. Therefore, impedance matching technique is required in our design.

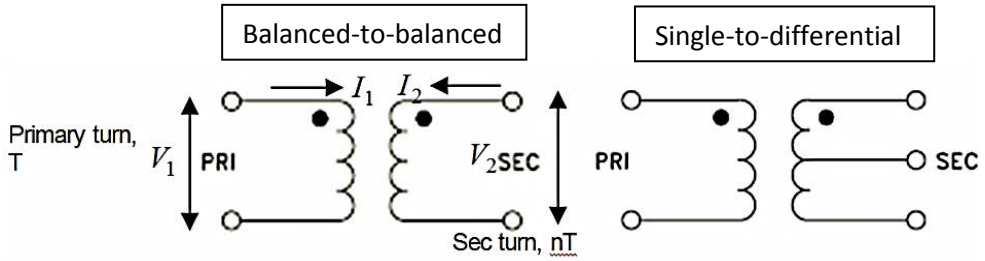

Figure 3-22: Balun transformer for impedance matching

A balun transformer as shown in Figure 3-22 can be used as an impedance matching network between a signal source output and the input of AD8350. In the design, single-to-differential balun (Figure 3-22, right schematic) is used to provide single to differential input interface to the amplifier. Generally, transformers can be used as voltage step up/down, to provide DC isolation for circuit protection while maintaining AC continuity. They also reject the common mode voltage. In general, for balanced-to-balanced balun transformer

$$\frac{V_2}{V_1} = \frac{I_1}{I_2} = n, \qquad (3.5)$$

$$Z_2 = \frac{V_2}{I_2} = \frac{nV_1}{I_1 / n} = n^2 \frac{V_1}{I_1} = n^2 Z_1, \tag{3.6}$$

where Z_1 is impedance of primary coil, Z_2 is impedance of secondary coil, V_1 is the potential at the primary coil terminals, V_2 is the potential at the secondary coil terminals, I_1 is the current flowing through primary coil, I_2 is the current flowing through secondary coil and n is the coil turn ratio. For 50 Ω to 200 Ω matching, a transformer with primary and secondary coil ratio of 2 is utilized.

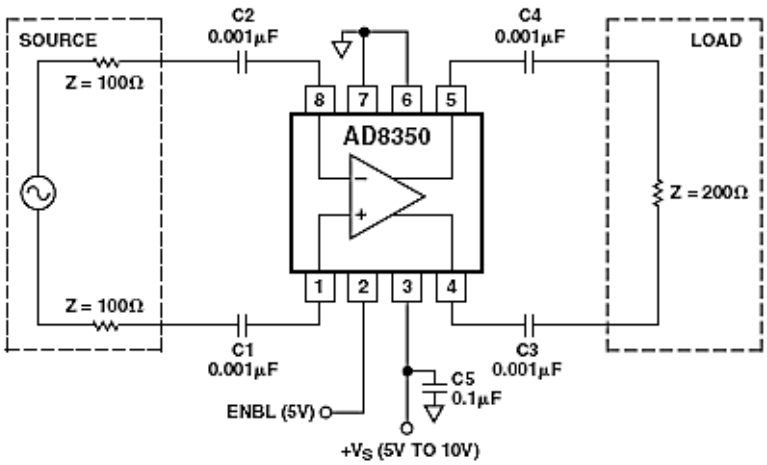

Figure 3-23: Basic connection of AD8350 [74]

Figure 3-23 shows the basic differential drive connection of AD8350. Note that both input and output have a DC bias level at mid-supply range and therefore need to be AC-coupled. Using two single-to-differential balun transformers with input/output impedance ratio of 1:4, we have connected two impedance matching networks to interface both input and output of AD8350 as illustrated in Figure 3-24. Figure 3-25 shows the design schematic which is drawn using PCB design software, the Altium Designer. Table 3-3 is used as a reference to route connections from AD8350 input/output pins.

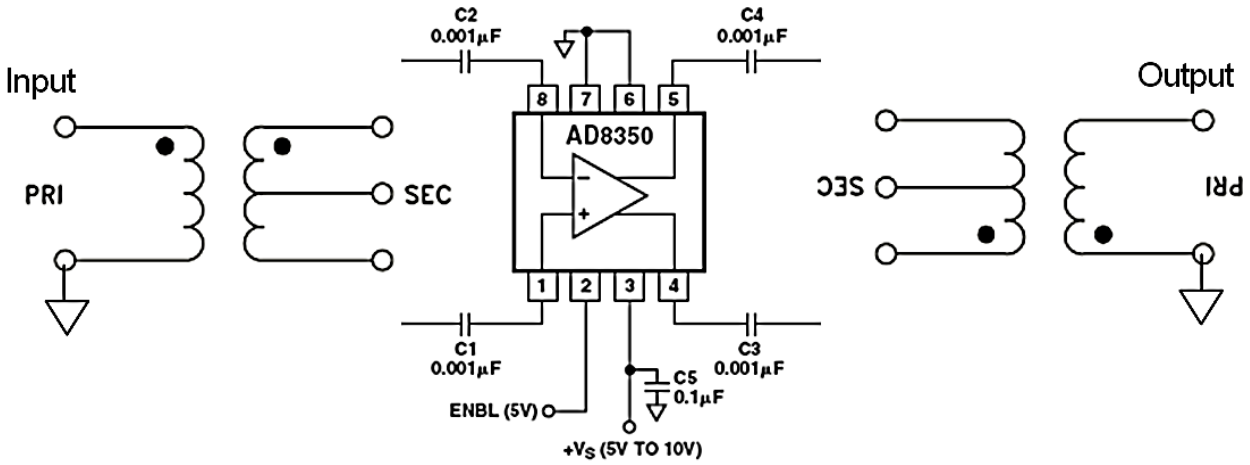

Figure 3-24: Interfacing AD8350 with impedance matching transformers [74]

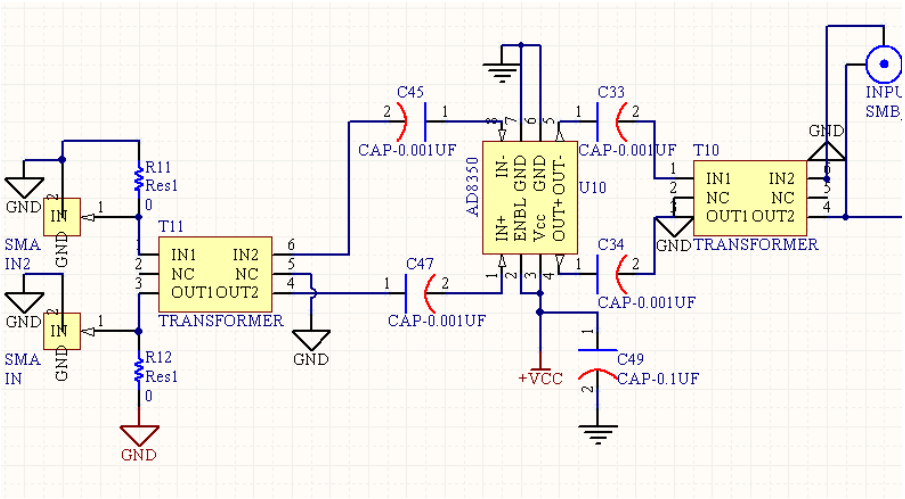

Figure 3-25: Schematic drawn for AD8350

Table 3-3: AD8350 pins legend [74]

PIN FUNCTION DESCRIPTIONS

Pin	Function	Description
1, 8	IN+, IN–	Differential Inputs. IN+ and IN– should be ac-coupled (pins have a dc bias of midsupply). Differential input impedance is 200 Ω.
2	ENBL	Power-up Pin. A high level (5 V) enables the device; a low level (0 V) puts device in sleep mode.
3	V_{CC}	Positive Supply Voltage. 5 V to 10 V.
4, 5	OUT+, OUT–	Differential Outputs. OUT+ and OUT– should be ac-coupled (pins have a dc bias of midsupply). Differential input impedance is 200 Ω.
6, 7	GND	Common External Ground Reference.

3.3.2.2 Design using AD8351

The AD8351 is a differential amplifier useful in RF applications up to 2.2 GHz. The benefit of utilizing this amplifier is that the voltage gain can be set using an external resistor. The range of tunable gain is from 0 to 26 dB. However, since the component is primarily designed for use in video applications, it has a high input impedance and a 150 Ω differential output impedance. Several issues to be tackled in the design include: input/output impedance matching, and optimized compromise between good frequency response with wide enough bandwidth and high voltage gain. Table 3-4 cites the values of external resistor R_G for various voltage gain values.

Table 3-4: Values of resistor, R_G for different gain [75]

(Load Resistance Is Specified as Single-Ended)

Gain, A_V	R_G (R_L = 75 Ω)	R_G (R_L = 500 Ω)
0 dB	680 Ω	2 kΩ
6 dB	200 Ω	470 Ω
10 dB	100 Ω	200 Ω
20 dB	22 Ω	43 Ω

For arbitrary values of gain, R_G can be obtained using the following expression:

$$A_V = \frac{R_L \times 5.6R_G + 9.2 \times R_F \times R_L}{R_G \times R_L \times 4.6 + 19.5 \times R_G + (R_L + R_F) \times (39 + R_G)} = \left| \frac{V_{OUT}}{V_{IN}} \right| , \qquad (3.7)$$

where A_V is gain, R_F is 350Ω internal resistance, R_L is the single-ended load resistance, and R_G is the gain setting resistance. Figure 3-26 shows the frequency response of AD8351 with respect to gain and R_G. From Table 3-4, it can be seen that higher gain corresponds to lower R_G and as gain increases, the bandwidth decreases as shown in Figure 3-26. This performance is thus undesirable.

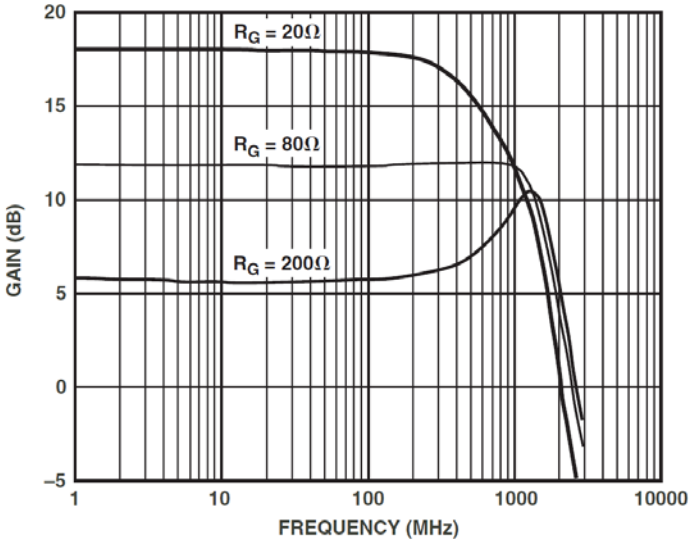

Figure 3-26: Gain vs frequency chart with different R_G values [75]

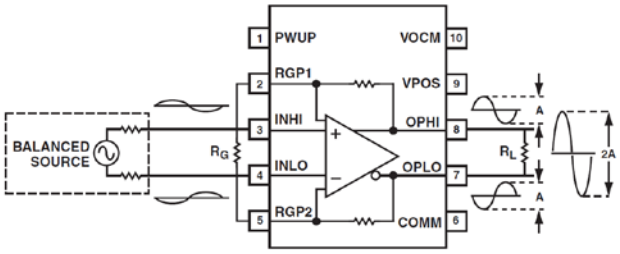

Figure 3-27: Basic connection of AD8351 [75]

The basic connection structure of AD8351 is shown in Figure 3-27. Impedance matching at the input pins requires termination resistors to match the source resistance. Impedance matching at the output requires impedance transformation of 150 Ω to 50 Ω. This can be done in two ways. One way is to have a transformer with turn ratio of 1.5 and another is to use matching passive components network (simplest would be resistor network, on the account of signal amplitude attenuation). The schematic of the matching network is illustrated in Figure 3-28.

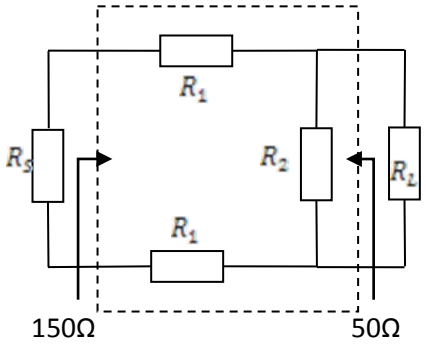

Figure 3-28: Resistor network for impedance matching

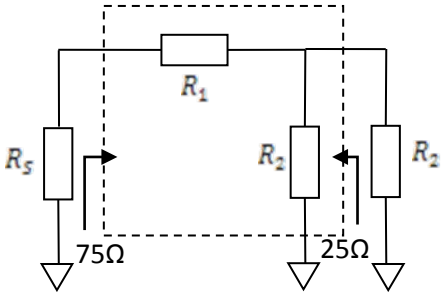

Figure 3-29: Resistor network for impedance matching (single-ended)

To simplify our analysis, we can consider only the single-ended segment of the network as shown in Figure 3-29. At the input,

$$R_1 + (R_2 \,//\, 25) = 75\,, \tag{3.8}$$

$$R_1 + \frac{25R_2}{25 + R_2} = 75\,, \tag{3.9}$$

$$R_1 = 75 - \frac{25R_2}{25 + R_2}\,. \tag{3.10}$$

At the output

$$R_2 \,//\, (R_1 + 75) = 25\,, \tag{3.11}$$

$$\frac{R_2(R_1+75)}{R_2+R_1+75}=25, \tag{3.12}$$

$$R_1R_2+75R_2=25R_2+25R_1+1875. \tag{3.13}$$

Substituting (3.10) in (3.13),

$$\left(75-\frac{25R_2}{25+R_2}\right)R_2+75R_2=25R_2+25\left(75-\frac{25R_2}{25+R_2}\right)+1875 \tag{3.14}$$

Solving (3.14) yields $R_1=43.2\Omega$ and $R_2=86.6\Omega$. With the calculated values of R_1 and R_2, an impedance matching network is constructed as shown in Figure 3-30.

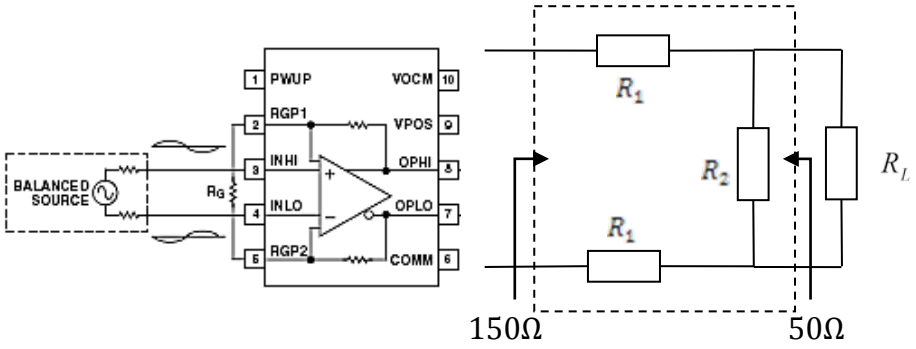

Figure 3-30: AD8351 with matching resistors

When the gain is set at 6 dB, and $R_G=200\,\Omega$, frequency response yields -3 dB bandwidth of 450 MHz.

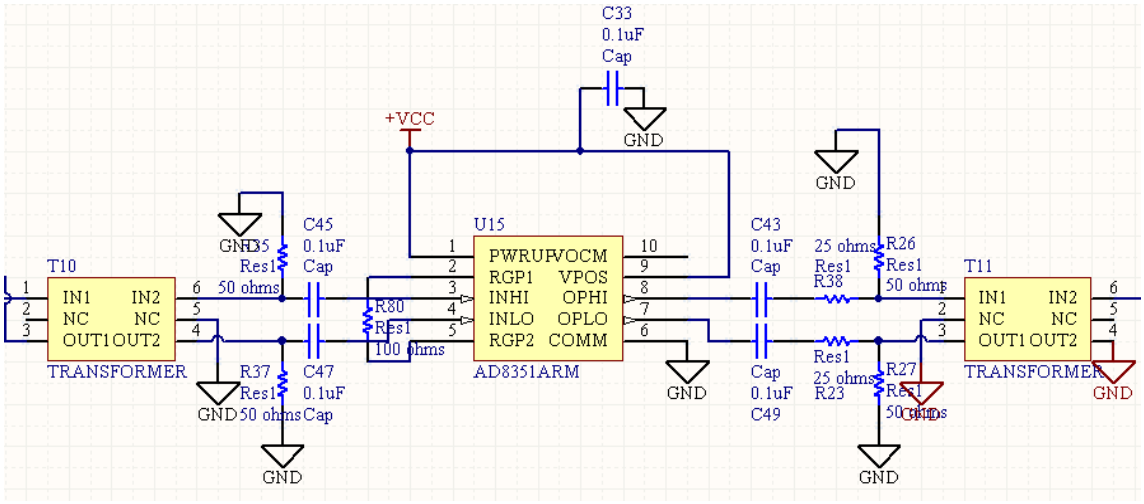

Figure 3-31: Drawn schematic of AD8351

Figure 3-31 shows the drawn schematic of AD8351 with the impedance matching networks using Altium Designer PCB design software.

3.3.2.3 Design using LMH6703

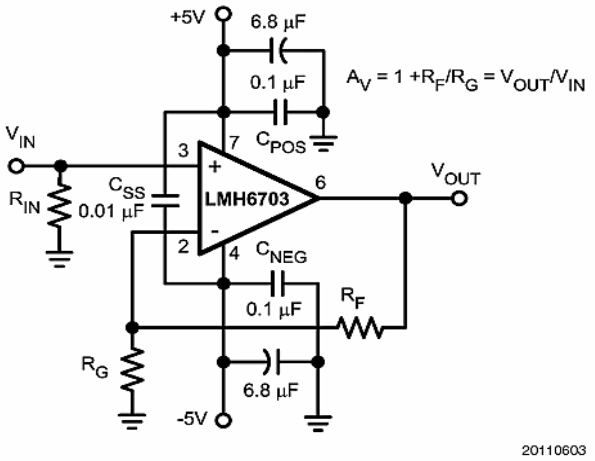

Figure 3-32: Non-inverting configuration of LMH6703 [76]

The LMH6703 is a wideband, DC-coupled, monolithic operational amplifier by National Instrument. The amplifier has a current feedback topology and has a practical gain range of ±1 to ±10, depending on the configuration setup. It has a maximum supply rating of ±6.75 V and has large input impedance (for non-inverting configuration as shown in Figure

3-32) with very small closed-loop output impedance. As discussed in the previous section, the configuration used for our design is non-inverting amplifier. From the datasheet, the optimized value for R_F is 560Ω for SOT23 6-pin package (used in our PCB) [76].

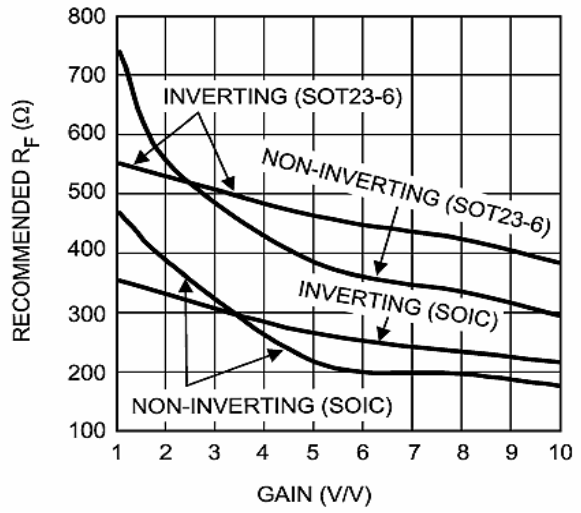

Figure 3-33: Recommended R_F vs gain chart [76]

According to Figure 3-33, increasing value of gain requires a decrease in the recommended R_F preserving a similar bandwidth performance. It is noted that if R_F is lowered too far from the recommended value, there will be signal overshoot with ringing oscillations. On the other hand, the effect of lowering R_F increases the frequency response. Therefore, an optimization of the amplifier's performance involves tuning the gain resistor R_G and selecting an appropriate R_F value which is referenced from Figure 3-33. In our design, R_F and R_G are selected to be 300Ω and 56Ω respectively with an effective gain of 5. Figure 3-34 shows the drawn schematic of design using LMH6703 using the Altium Designer software.

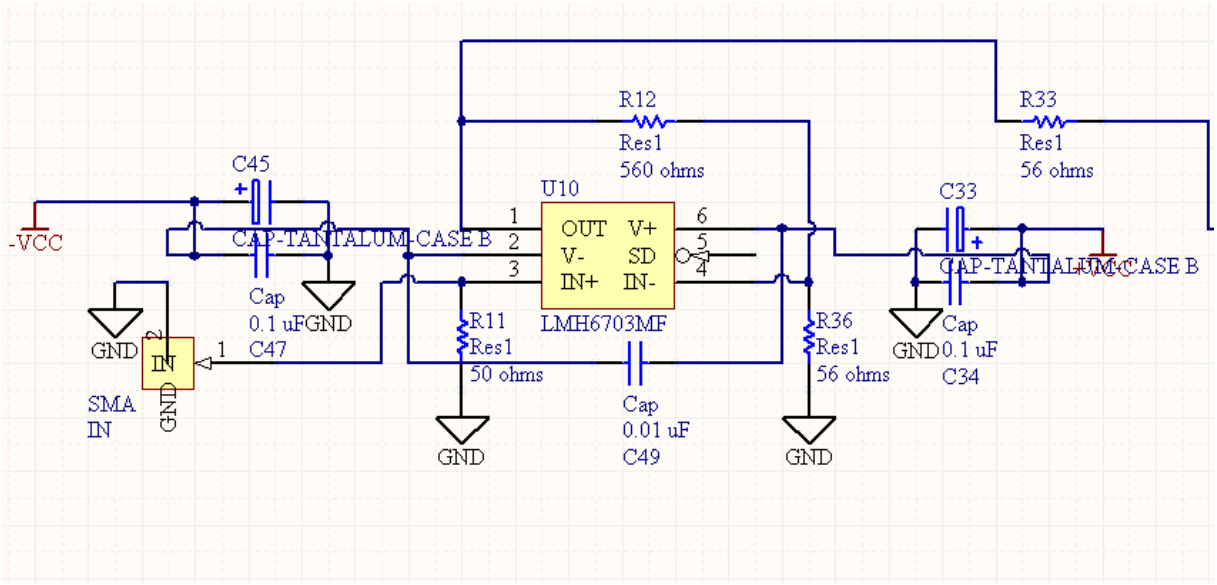

Figure 3-34: LMH6703 drawn schematic connection

With the discussion of various options of the available amplifiers, the next step is to consider various channel requirements from the amplified output signal. In this design, an eight channel signal splitter is used. Component JCPS-8-10+ (manufactured by Minicircuits) power splitter meets the sufficient requirement in terms of bandwidth and the number of output channels. In this case, eight output channels are provided. From the datasheet, the operating bandwidth ranges from 5 MHz to 1 GHz [76]. Input and output impedances of the component are 50Ω each.

3.3.3. PCB Design and Overall Signal Requirement

A printed circuits board (PCB) is fabricated with 4 layers structure to ensure good signal quality. This includes a ground plane which provides shortest current return path and minimizes extra impedance which can induce signal reflection of high frequency signals. The signal track width is set to 20 mil with characteristic impedance of 50 Ω. Power track width is set to 50 mil to minimize high frequency noise. As recommended in most datasheets, ground planes and power planes were removed near the input and output pins to reduce

parasitic capacitance. Components in the feedback path are placed as close to the device as possible to minimize parasitic capacitance. Bypass capacitors should also be placed as close to the device as possible, and the larger electrolytic bypass capacitors should be located further from the device. Frequency response of the AD8350 can reach up to 700 MHz (in two stages) with power supply of ±7 V.

The frequency bandwidth of AD8351 is even higher; reaching up to 800 MHz. LMH6703 bandwidth performances is similar, only that two-stage LMH6703 configuration shows frequency response peaking at higher end frequency which is not as desirable. For the final board implementation, the AD8350 is chosen for our application. This is because despite higher bandwidth of other amplifiers (in terms of magnitude of amplification), the AD8350 provides a more stable performance. As discussed in the previous section, the AD8351 tunable gain is between 0-26 dB. However, due to the implementation of a resistor matching network for loading, there is signal attenuation at the output. The overall gain of the two stages using AD8350 is 15 dB due to signal/loading or matching at the splitter.

Signal attenuation at the input is needed to prevent over-saturation of subsequent stages. In this case, a 7 dB attenuator is included at the input stage. In-situ FH input signal requires a small magnitude of approximately 200 mV, an attenuator of 20 dB is included at one of the channel output. If the magnification of the channel is 15 dB, effective attenuation for in-situ FH signal would be 5 dB. Note that the maximum input voltage level for AD8361 chip is 660 Vrms. For missing pulse outputs, two channels for lower and higher frequency selections are provided through the use of a multiplexer. This is to facilitate band-stop filtering of missing/extra pulse signal to eliminate very low frequency modulation.

In all, electronics design of a universal amplifier with various analog module implementations had been carried out. The back-end electronics box includes two universal

amplifier boards with missing/extra pulse low pass filter of 30 MHz, two universal amplifier boards with missing/extra pulse low pass filter of 90 MHz, one signal conditioning board, one position error signal (PES) board, one microcontroller board and two multiplexer boards. Figure 3-35 shows the PCB design layout of Universal Amplifier in Altium Designer software. Gerber files are generated and sent for PCB fabrication. The PCB is integrated in a custom-build enclosure which also houses the in-situ FH PCB, the MCU PCB and the power supplies as shown in Figure 3-36.

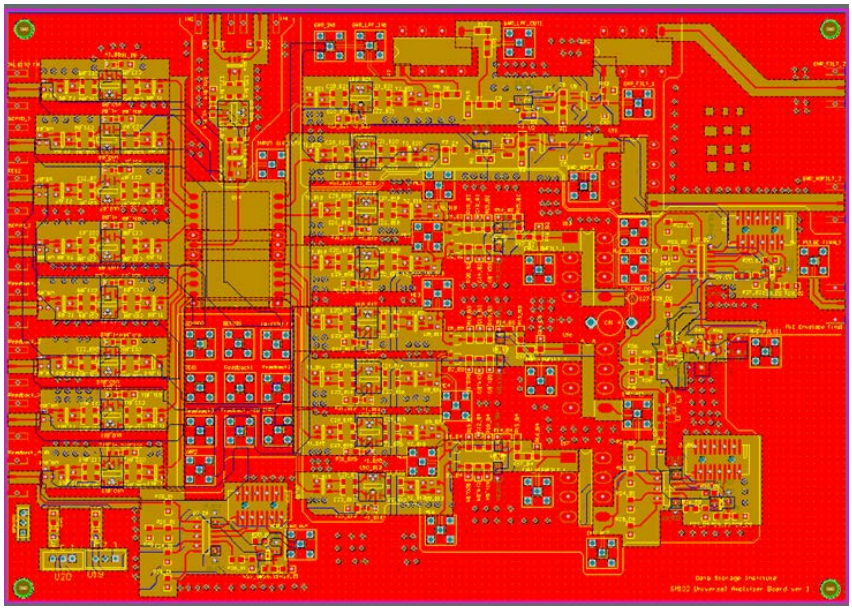

Figure 3-35: Universal Amplifier PCB design

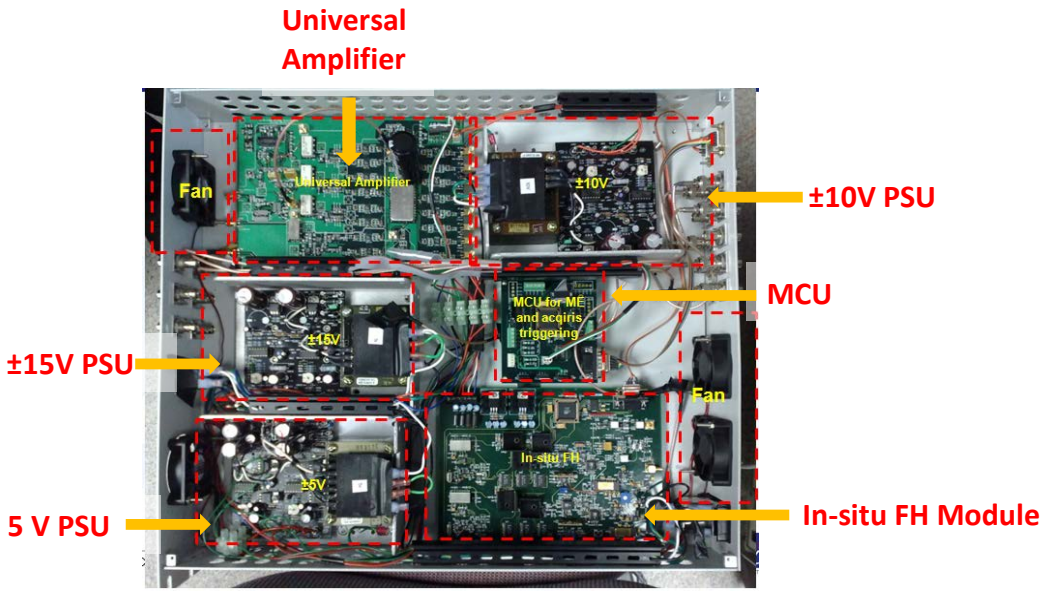

Figure 3-36: Backend Electronics integration

3.3 Software Development

Devices are generally controlled via microcontroller unit (MCU), programmable logic converter (PLC) or field programmable gate array (FPGA) hardware. These controllers are usually embedded on PCB with various PC interface implementation such as serial communication port or Peripheral Component Interconnect (PCI) technology. In serial interface, device controllers are connected to serial communication ports of PC. Serial communications usually involve handshaking where devices give response to PC if the strings of command are correct. For controllability using external software, the equipment vendor will usually package their hardware with a set of software modular functions in the form of Dynamic Link Libraries (DLL), ActiveX or General Command Set (GCS). DLLs are created in windows environment where it is convenient for programmers to use the functions without having to re-write applications. The ActiveX is an object developed under the Component Object Model (COM) environment in Windows platform that can be used independently as control to build applications. The usage of ActiveX requires manipulation of pre-defined control properties and programmers cannot alter the basic functionality of the object. The simplest form of hardware control language is the General Command Set (GCS) which in general, a device's firmware can understand. This General Command Set is transmitted as ASCII character and transmission can usually be done using a standard telnet application or serial communication programs such as Realterm or ProCom.

Labview is a high-level programming language, where the programming language syntax is described using graphical function blocks. Due to its visual methodology, it is easier for software developers to build sets of customized functions which are ready to be used by other Labview users. If Labview users do not have good understanding of Labview's resource management and execution, Labview programs can sometimes be less computationally efficient than C or C++.

The GUI implements hardware control through common hardware interfaces such as RS232, USB, GPIB and IEEE488. In this case, the Virtual Instrument Software Architecture (VISA) platform is used as standard for configuring, programming, and troubleshooting instrumentation systems comprising of GPIB, VXI, PXI, Serial, Ethernet, and/or USB interfaces. Utilizing VISA input-output standards with Labview requires NI-VISA software libraries. In this way, software development will no longer become obsolete as the instrumentation hardware interface changes. The main graphical user interface (GUI) focuses on integrating the sub-system functions and making use of the control access functions to implement test routines. The GUI should also display the desired result of testing in the form of charts or output raw data via text or spreadsheet files. When the program starts, it will first perform communication port initialization. Subsequently, manual initialization of individual hardware is performed. The spindle controller and the load/unload controller are initialized using GCS commands and the E752 PZT controller is initialized using DLL call method in Labview.

The DLL contain functions (written in C++ in our case) which can interact directly to hardware via serial port or other interfaces and perform front-end routines. In our case, control of the FPGA system is accessed with C++ coding through serial communications and microcontroller and thus, the functions developed for these routines can be compiled into DLLs. In our case, DLL for PZT controller is provided by the manufacturer. In Labview, the DLL can be easily accessed by 'Call Library Function Node' module as shown in Figure 3-37.

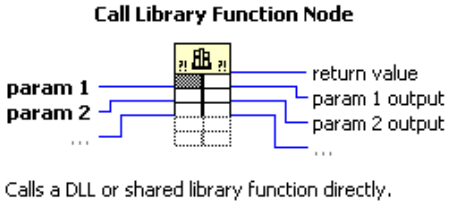

Figure 3-37: Labview DLL call

It is essential to have the information of DLL functions as definitions of input as output parameters need to be configured manually and have to be consistent with DLL documentation. Most of the DLLs will use stdcall (WINAPI) calling convention. For example, to invoke the PZT controller for connection to PC, the Call Library function setting is shown in Figure 3-38. The function prototype definition needs to be known and is referred from the user programming reference manual.

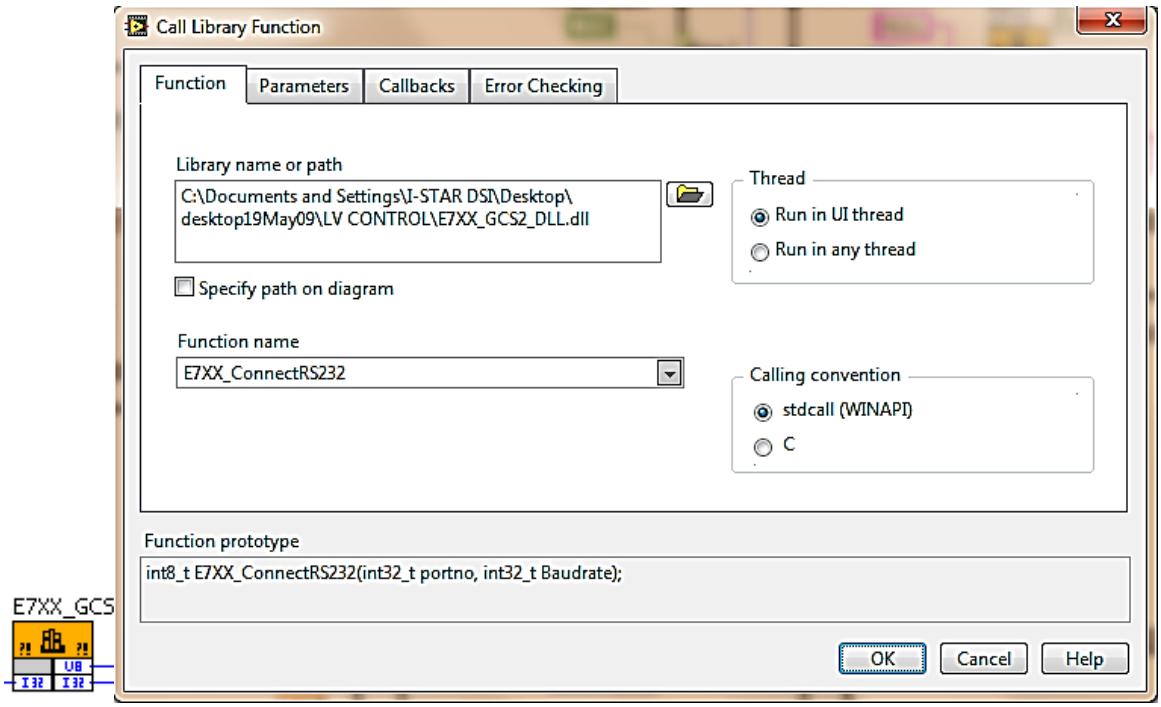

Figure 3-38: DLL block and setting

The input is a long (32-bit) signed integer and the output is an unsigned 8-bit integer as indicated in the block functional diagram. The graphical code is shown in Figure 3-39.

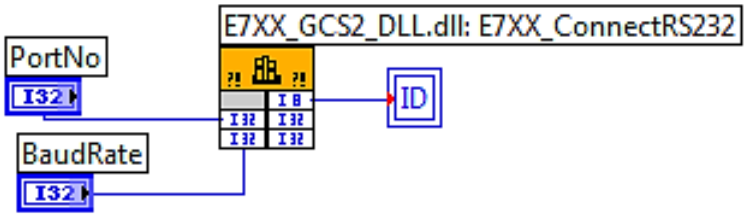

Figure 3-39: DLL call graphical code

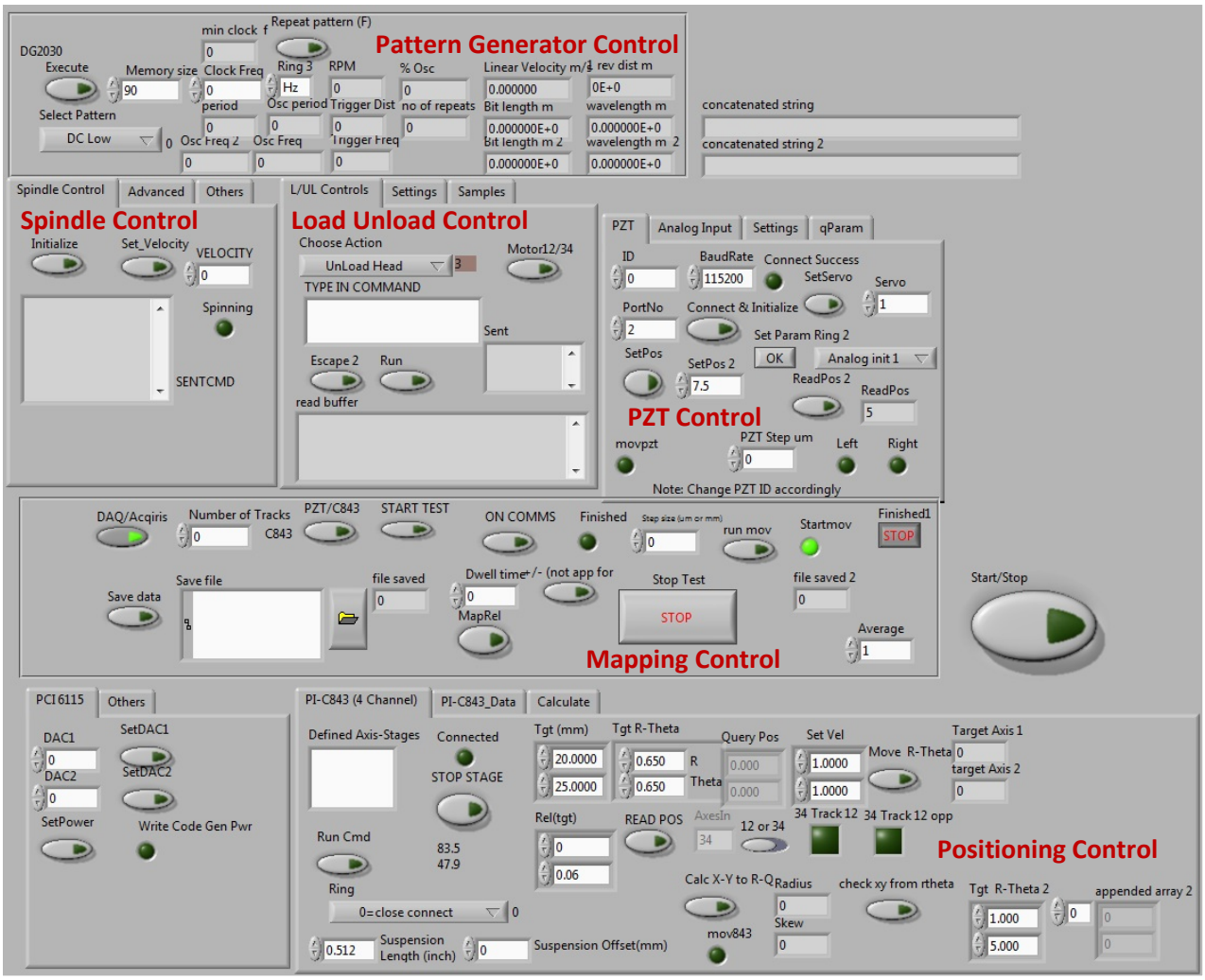

Figure 3-40: Tester GUI

Figure 3-40 shows the final tester GUI.

3.4 Summary

In this chapter, the author's contribution to the development of a multifunctional spinstand was described. Firstly, integration of basic key components of the spinstand has been discussed. This includes an overview of the load-unload system, spindle, linear motion stages, and PZT transducer for fine-positioning. The rotating spindle is chosen to be an air bearing aerostatic type due to its high reliability as long as constant compressed air supply is available. A vertical load-unload system has also been realized with the implementation of

two DC motors and an oval cam. In this way, the speed of load-unload can also be controlled with more precision. A calibration method to position the slider on the media in the Cartesian coordinates corresponding to the polar coordinate system used in hard disk drives has also been described in detail. Finally, the addition of HDI measurement tools such as the AE sensor, in-situ FH module and LDV helps to increase the capability of the developed tester to characterize the head disk interface more accurately.

The goal of electronic development of the integrated media tester is to process the readback signal so that it meets the requirement of back-end signal processing. Therefore, the major electronic design work involves analog RF signal conditioning to achieve appropriate signal amplification and to obtain good frequency response. This includes good impedance matching techniques and alternative component selections. The design of multiple readback signal splitter with uniform power outputs is also achieved to cater for backend signal processing.

Good hardware and software integration is critical to deliver an optimum control of the instrument through the graphical user interface. Labview has been used as the main development software for the GUI and various hardware control methods, *i.e.*, DLLs, GCS commands, *etc*. The GUI also includes major testing routines such as track profile, readback mapping, *etc*. Finally, electronics development for backend testing functionality such as the universal amplifier and servo implementation had been discussed.

Finally, a printed circuits board (PCB) is fabricated with 4 layers structure to ensure good signal quality with minimal noise. The frequency bandwidth of the universal amplifier is also increased by 200 MHz by boosting its power supply input. The integration of the back-end electronics box is also completed which includes two universal amplifier boards with missing/extra pulse low pass filter of 30 MHz, two universal amplifier boards with

missing/extra pulse low pass filter of 90 MHz, one signal conditioning board, one position error signal (PES) board, one microcontroller board and two multiplexer boards.

CHAPTER 4: Media Mechanical Defects Measurement and Slider Dynamics

The development of multifunctional spinstand brings additional capabilities for more comprehensive testing of the head disk interface. Since the developed spinstand offers unique combination of LDV, AE, and in-situ FH, two major applications are being developed in this thesis. The first part of this chapter reports on the author's effort to explore new media defects detection method using combined optical and magnetic methodologies. Optical method offers fast scanning time while read head-based scanning offers high lateral resolution. The unique combination of these two methods, with special arrangement of the spinstand setup, will increase overall testing time and increase testing throughput.

The second part of this chapter explores TFC slider dynamics measurement using concurrent measurements of LDV, AE, missing pulse, and in situ FH. Contact induced slider dynamics are being analyzed when slider encountered media defect as well as during thermal protrusion contact.

4.1 Missing Pulse Method for Media Defect Detection

This work implements the missing pulse method on the integrated spinstand as one of the characterization tools for the head disk interface. Missing pulse detection is an electrical measurement which can be used for mechanical defect measurement with high lateral resolution. This test has been a standard by The International Disk Drive Equipment and Materials Association (IDEMA) since 2005 to test for media defects using a readback waveform. Media defects (anomalies in the otherwise homogeneous magnetic layer) may cause distortion in the readback signal, which interferes with proper data recovery. Depending on the size, shape, type of the anomaly, and its location with respect to the

recorded transitions, the defect may cause differing effects on the readback signal. The effects can even vary from one write pass to the next. The types of signal distortion caused by media defects include sudden decrease and increase in amplitude, generation of signals where none were written, shift in time, and various combinations of the above. The missing pulse test is used to isolate mechanical defects which cause changes in amplitude of the readback signal.

According to the specified method by IDEMA [50], the media must first be preconditioned using high frequency signal for one revolution. Subsequently, the readback signal is analyzed to a specified missing pulse threshold (positive or negative values). A missing pulse is defined as any anomaly in the analog read signal that does not reach a specified level of amplitude. This missing pulse threshold is specified as a percentage of mean track average amplitude. The implementation of missing pulse in our system utilizes the readback signal envelope to quantify the positive and negative peak amplitude values. This implementation can be done using an amplitude modulation (AM) wave demodulation circuit to rectify the readback signal. Figure 4-1 shows a half wave rectifier envelope detector. In this design, the diode retains the maximum peak value of a carrier waveform, followed by low pass filter to smooth the envelope ripples.

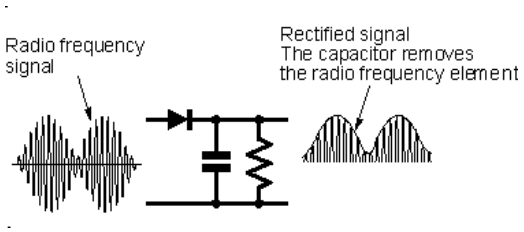

Figure 4-1: Amplitude demodulation

In the configuration shown in Figure 4-1, the diode polarity is sensitive to positive voltage. The diode is chosen to have small forward voltage to cater for small signal input (typically, $400mV_{peak\text{-}peak}$, maximum readback signal amplitude $1V_{peak\text{-}peak}$) and also the

reverse recovery time has to be in the order of 1 ns and below to cater for fast rapidly changing pulses. The rectified signal is then low pass filtered using a first order filter configuration which consists of a capacitor in parallel with a resistor as shown in Figure 4-1. Lower *RC* or time constant is desirable for faster response time and less signal attenuation at higher frequency. *RC* value needs to be optimized to allow output waveform to follow the waveform peaks. If *R* is chosen to be 1000 Ω at 30 MHz low pass filter cut-off frequency, then the value of capacitor is calculated as

$$C = \frac{1}{2\pi(1000)(30\times10^{6})} = 5.3\,\text{pF}. \qquad (4.1)$$

An increase in linear density requires a readback envelope with higher resolution. Lower capacitor value can be chosen to increase the cut-off frequency of the low pass filter to allow higher frequency components of the readback envelope. The top trace in Figure 4-2 shows a readback waveform with amplitude modulation frequency of 50 kHz and the resulting readback envelope is shown as the bottom trace of the oscilloscope window. Figure 4-3 illustrates the readback envelope at higher resolution with higher frequency components.

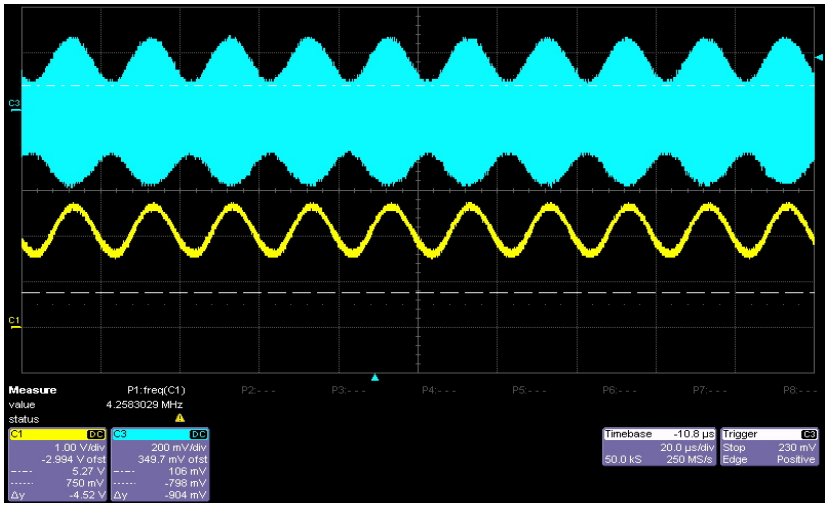

Figure 4-2: Readback modulation

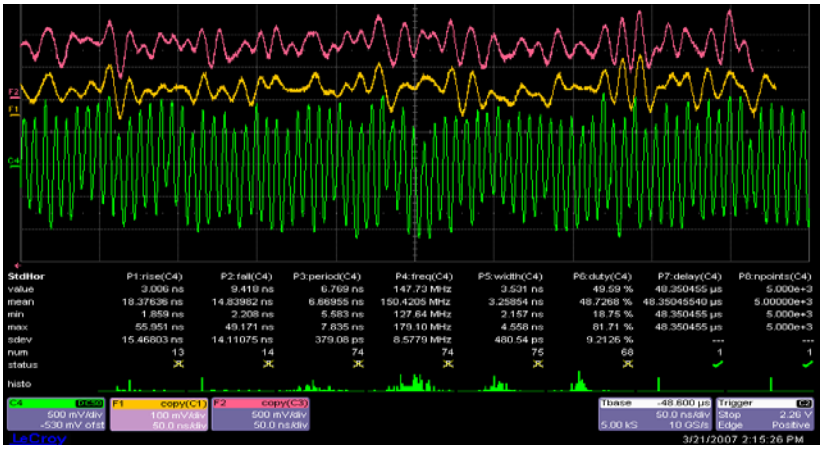

Figure 4-3: Readback signal envelope

In order to have a stronger sensitivity, the missing pulse signal should also use the negative envelope; as such, a similar circuit with inverted polarity diode is constructed. Note that the DC level resulting from the envelope detection is crucial in missing/extra pulse analysis. Assuming a symmetrical readback waveform, the two envelopes can be subtracted by a differential amplifier, AD8130, with unity gain to achieve the final result. The schematics of missing pulse circuits are shown in Figure 4-4.

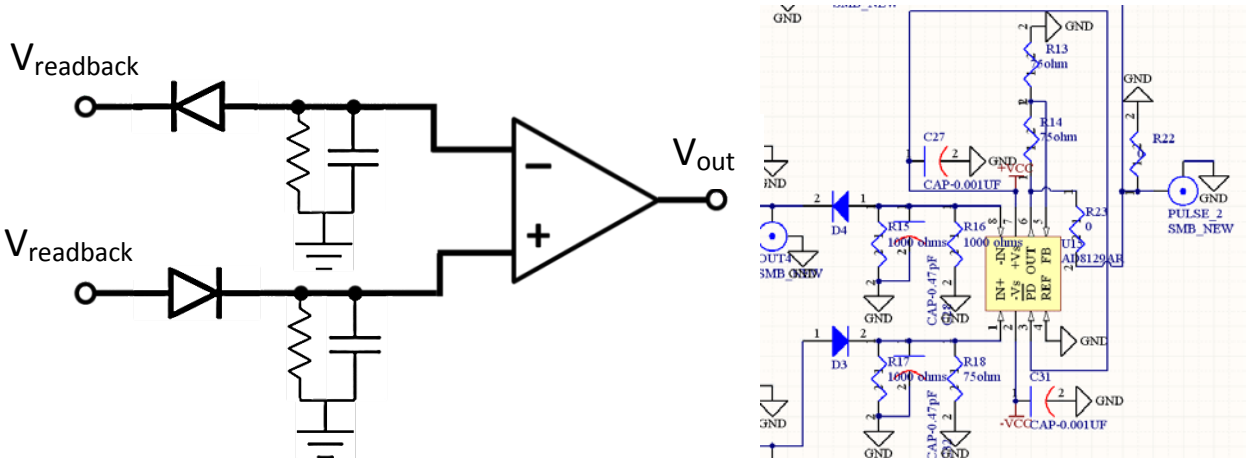

Figure 4-4: Missing pulse circuit schematics

To test the implementation of envelope detection and to investigate its potential for media defects detection, two experiments are performed to detect and characterize both large and small defects. Figure 4-5 shows the experimental setup. A readback waveform is

obtained from the Guzik spinstand which is then amplified using a universal amplifier. The amplified signal serves as input to a missing pulse circuit and the missing pulse signal output is digitized at 1GS/s using an 8-bit digitizer.

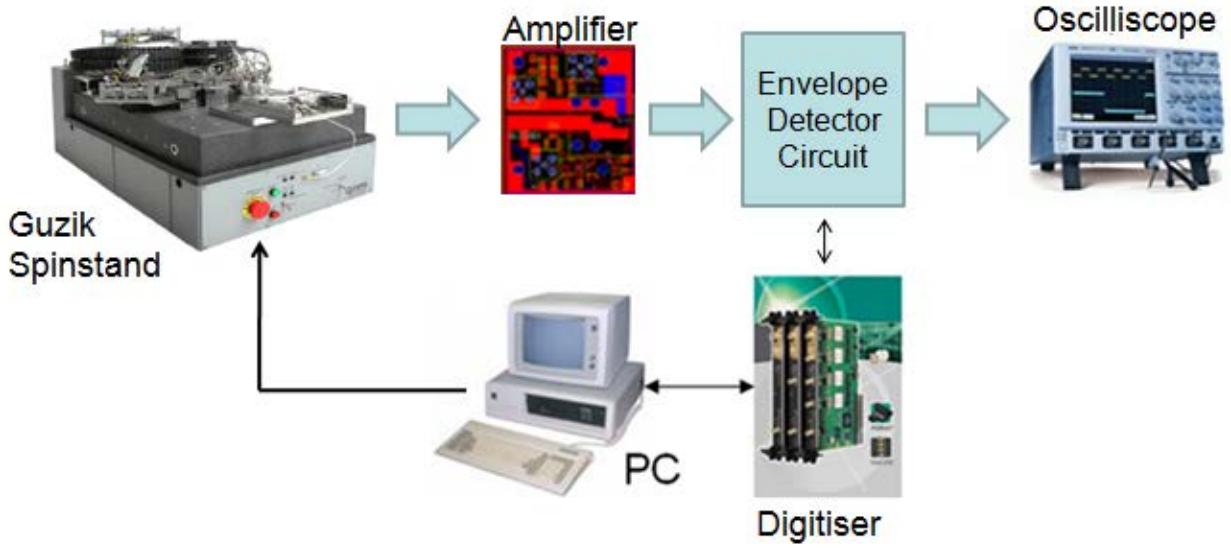

Figure 4-5: Schematic of missing pulse measurement

To test the detection of large defects, the slider is flown over the laser zone texture (LZT), which is usually located at the inner diameter (ID) zone of a magnetic media. In this region, large bumps are fabricated with laser pulses in regular pattern along the circumferential direction. The main purpose of these bumps is to provide the slider with non-smooth surface to park when it is not flying. This reduces stiction during contact start-stop sequences and increases reliability. In our test, the LZT region is located at the radius of 0.6 to 0.7 inch of a 3.5 inch commercial media. The laser bumps on a disk simulate large physical defects of approximately 8 µm in diameter. A missing pulse signal map given in Figure 4-6 shows that the readback magnetic signal is present and is different over the laser bump region. As a result of different magnetic readback signal at each laser bump, individual laser bumps are clearly resolved, suggesting that missing pulse method (although a dominantly

magnetic approach), can also be used for indirect detection and measurement of physical morphology changes.

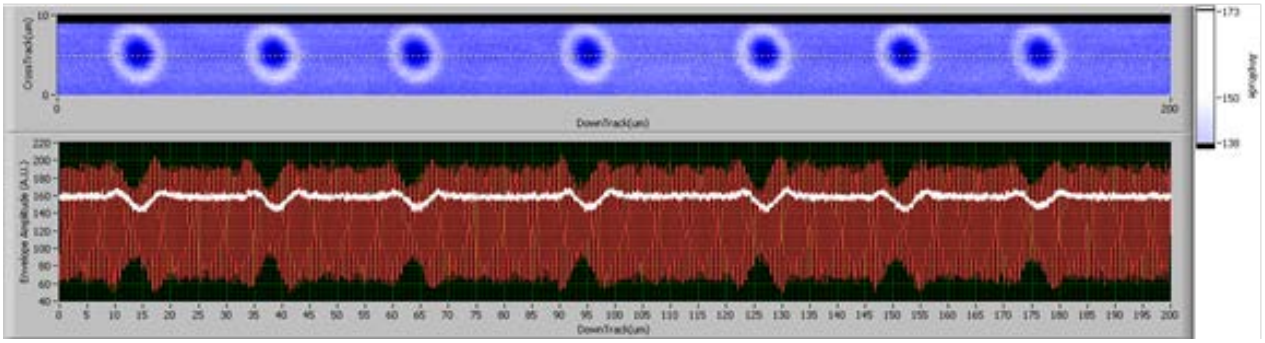

Figure 4-6: Laser bumps mapping

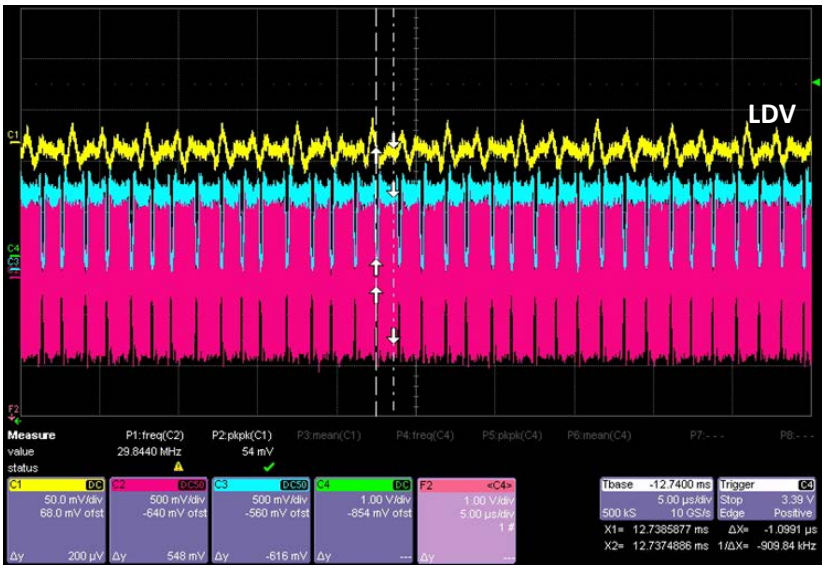

Figure 4-7: Missing pulse signal of laser bumps at 0.69" and 600 kHz frequency.

Figure 4-7 shows the testing result of missing pulse measurement which is performed on laser bump region with a commercial wide writer head. A wide writer head has typical write track width of 50 µm and read track width of 200 nm. All 1s 30 MHz data pattern is written at 0.69 inch radius and bump frequency is measured to be 600 kHz at 7200 RPM. At this frequency, the bump separation width can be calculated to be

$$\text{Bump separation width} = \frac{1}{600000 \times 8.3 \times 10^{-3}} \times 2\pi \times 0.69 \times 25400 = 22.1\mu m. \quad (4.2)$$

LDV controller OFV3000 is utilized with velocity measurement at 1 mm/s/V. The raw LDV signal is then bandpass filtered between 200 kHz to 800 kHz to isolate the signal corresponding to disk bump as shown in Figure 4-7 (top oscilloscope trace).

Figure 4-8 shows the detection capability of the missing pulse method for various defect sizes. The defect patterns were tested under the developed tester using the missing pulse method and compared to optical Kerr results using the optical surface analyzer (OSA). Mapping of missing pulse is done using a digitizer with sampling time of 1 ns and step size of 10 µm. Resolution of missing pulse method is governed by the detection bandwidth (1 GHz ~ 1 nm). In addition, the detection capability of magnetic mapping is solely dependent on missing magnetic information and is independent of the etch depth. From the mapping, missing pulse method is able to clearly distinguish each defect and provide good estimate of defect width, whereas for OSA, individual defect widths and especially their separations are not well resolved. The depth and width information also appear mixed in the OSA line profiles, whereas the missing pulse case provides consistent determination of correct width and depth.

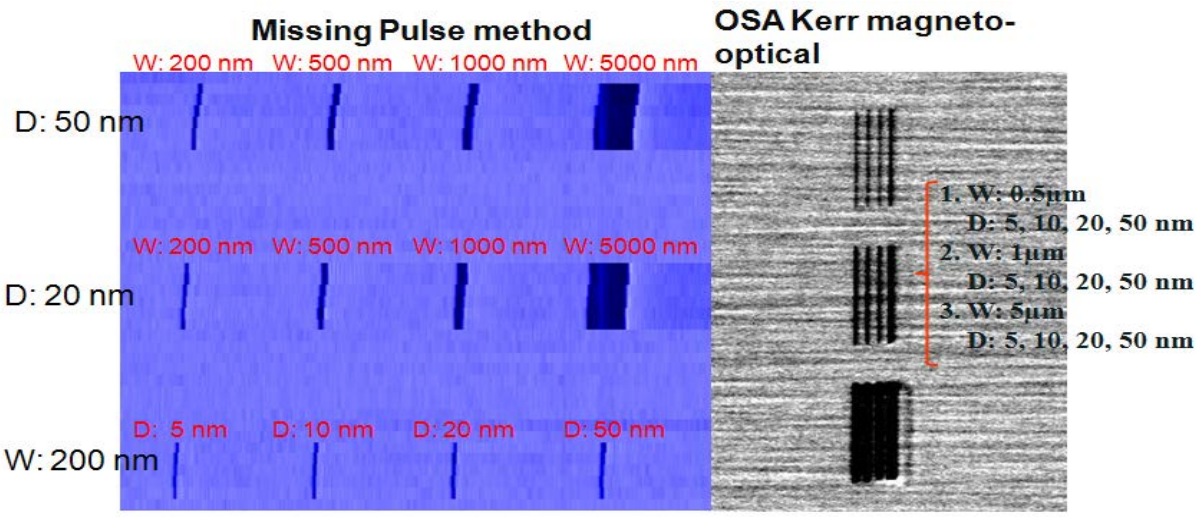

Figure 4-8: Comparison of MP and OSA Kerr effect mapping

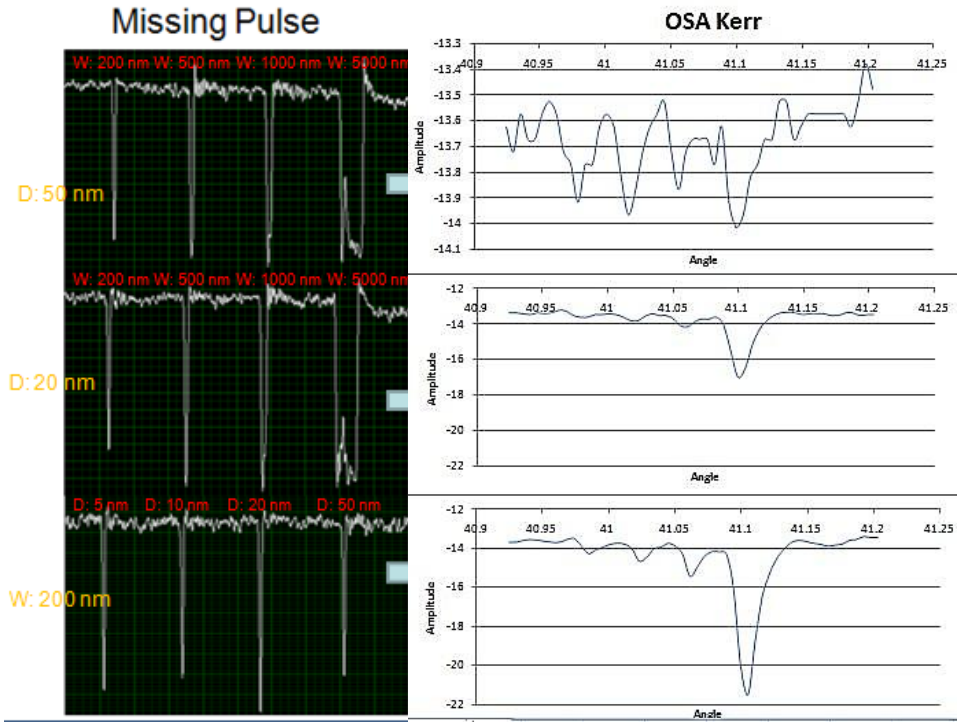

Figure 4-9: Line profile comparison of MP and OSA Kerr, D: depth and W: width

Figure 4-9 shows the line profiles of both missing pulse and OSA measurement. It can be seen that the magnetic missing pulse image shows sharp groove walls even for the width of 200 nm. This shows superiority (resolution and accuracy) of the proposed magnetic approach over the optical approach.

4.2 Defects Detection using Laser Doppler Vibrometer (LDV)

Laser Doppler Vibrometry (LDV) has contributed significantly to the growth of hard disk drive industry. It is a non-contact measurement device, which can quantify velocity or displacement in terms of its magnitude and frequency. Figure 4-10 shows the schematic of a heterodyne vibrometer. In heterodyne configuration, an acousto-optic modulator, known as Bragg cell, is inserted along one of the laser paths to shift the frequency of reference beam, f_0 by f_B. The detector receives frequency and phase modulated signal with f_B carrier frequency. As such, it will only detect the carrier frequency f_B if there is no object motion.

Subsequently, any object motion will increase or decrease f_B depending on the direction of the object motion. This phenomenon is known as Doppler frequency shift.

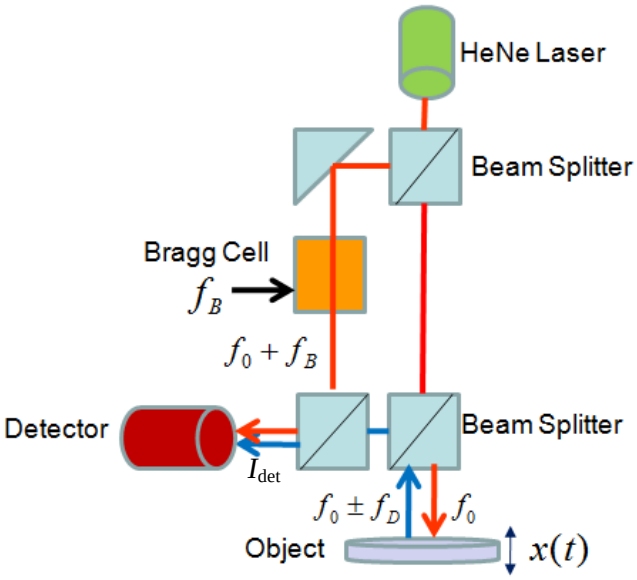

Figure 4-10: Principle of LDV, heterodyne interferometer.

The LDV focuses the laser beam spot onto the surface of an object to be tested; the reflected beam is collected back and recombined with the frequency shifted reference beam. Doppler frequency shift is then demodulated to produce measurement of velocity or displacement in the direction parallel to the beam [51]. From Figure 4-10, the intensity at the detector is given by (4.3) [51]

$$I_{\text{det}} = I\left[1+\cos\left(2\pi f_B t+\varphi_m+\varphi_0\right)\right], \qquad (4.3)$$

where I_{det} is the intensity of the laser at the detector, f_B is Bragg cell frequency, φ_m is the movement phase and φ_0 is the fixed initial phase. Any change in displacement, $x(t)$ as a fraction of laser wavelength will give rise to displacement change of $2x(t)/\lambda$. Considering both forward and return direction of laser path, the phase of the movement can be expressed as

$$\varphi_m = \frac{2x(t)}{\lambda} \times 2\pi = \frac{4\pi x(t)}{\lambda} \quad , \qquad (4.4)$$

where φ_m is the phase of the movement, $x(t)$ is the displacement and λ is the wavelength. Phase demodulation gives displacement information. In this case, a repetitive movement of object with vibration frequency of f_{vib} will give rise to

$$\varphi_{vib} = \varphi_m \cos(2\pi f_{vib} t + \varphi), \qquad (4.5)$$

where φ_{vib} is the repetitive change of phase, φ_m is the movement phase, f_{vib} is the vibration frequency, and t is time. Therefore the frequency modulation is given by (4.6)

$$f_m = \frac{\text{no of cycles}}{\text{time}} = \frac{\varphi_m \cos(2\pi f_{vib} t + \varphi)}{2\pi t} = \frac{2v}{\lambda} \cos(2\pi f_{vib} t + \varphi) \ , \quad (4.6)$$

where φ_{vib} is the repetitive change of phase, φ_m is the movement phase, f_{vib} is the vibration frequency, and t is time. Frequency demodulation gives velocity information.

4.2.1 LDV Study of Defect Detection

To investigate the detection of small defects, a systematic study is conducted using special patterns on flyable disk media with known dimensions. The tester setup is modified as shown in Figure 4-11. In this setup, the laser probe of the LDV is mounted on the secondary linear stages and an objective lens is required to reduce the beam spot size to 1 μm.

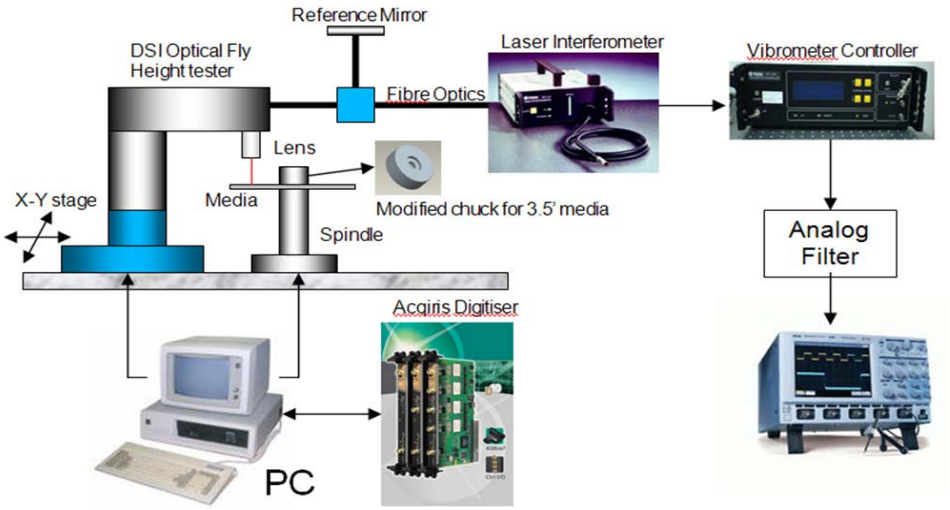

Figure 4-11: Setup for LDV study of defect detection

The test pattern consists of arrays of etched grooves of different widths and depths as shown in Figure 4-12. The range for width and depth are 80 nm to 5 um and 5 nm to 50 nm, respectively. These patterns are fabricated using the focused ion beam (FIB) and the dimensions of the patterns are further verified using the Atomic Force Microscope (AFM) to ensure accuracy. The systematic variations in both depth and width of the pattern help to test detection sensitivity and accuracy.

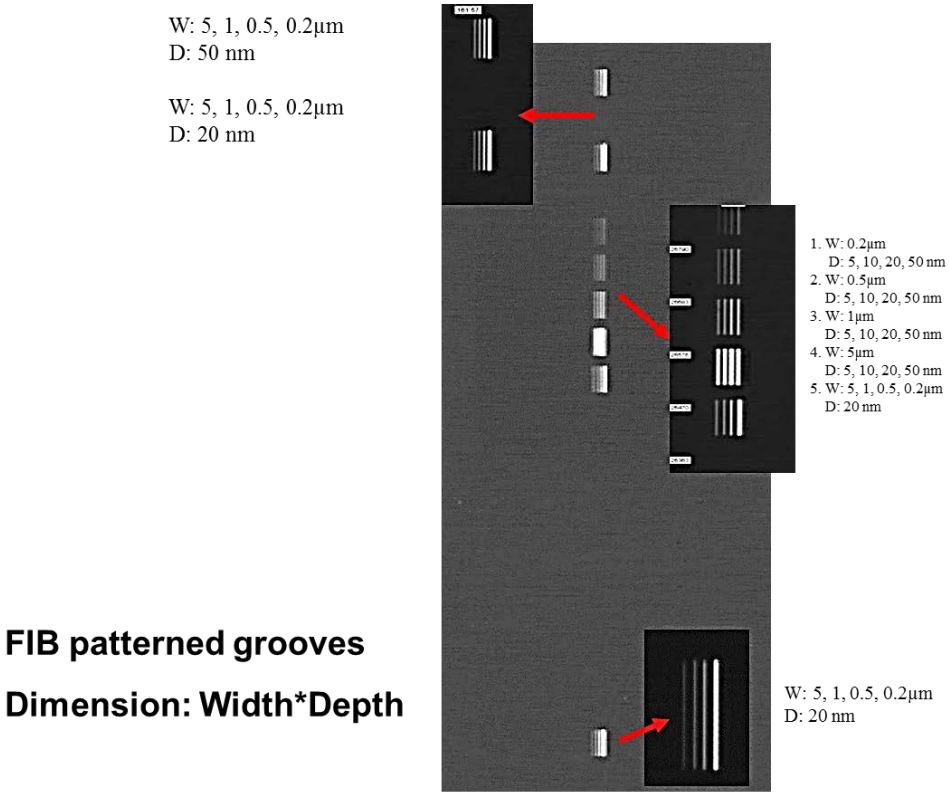

Figure 4-12: Systematic preparation of defect sample using the FIB

With known pattern topography, it is simpler to interpret the measured signal and it is possible to derive the dependence of LDV output signal with respect to the pattern's lateral and depth dimensions. Figure 4-13 and Figure 4-14 show the expected signal output of LDV displacement and velocity mode measurement respectively. Displacement mode signal maps out the feature dimension while its signal gradient corresponds to velocity signal (range of change of defect slope). It can be seen that velocity signal produces spikes which correspond to the slope edge of the pattern topography. As illustrated in Figure 4-13, the intensity of signal amplitude is also dependent on laser beam spot size. Ideally, the beam spot size should be as small as possible to achieve very high signal-to-noise ratio (SNR) with higher output signal intensity.

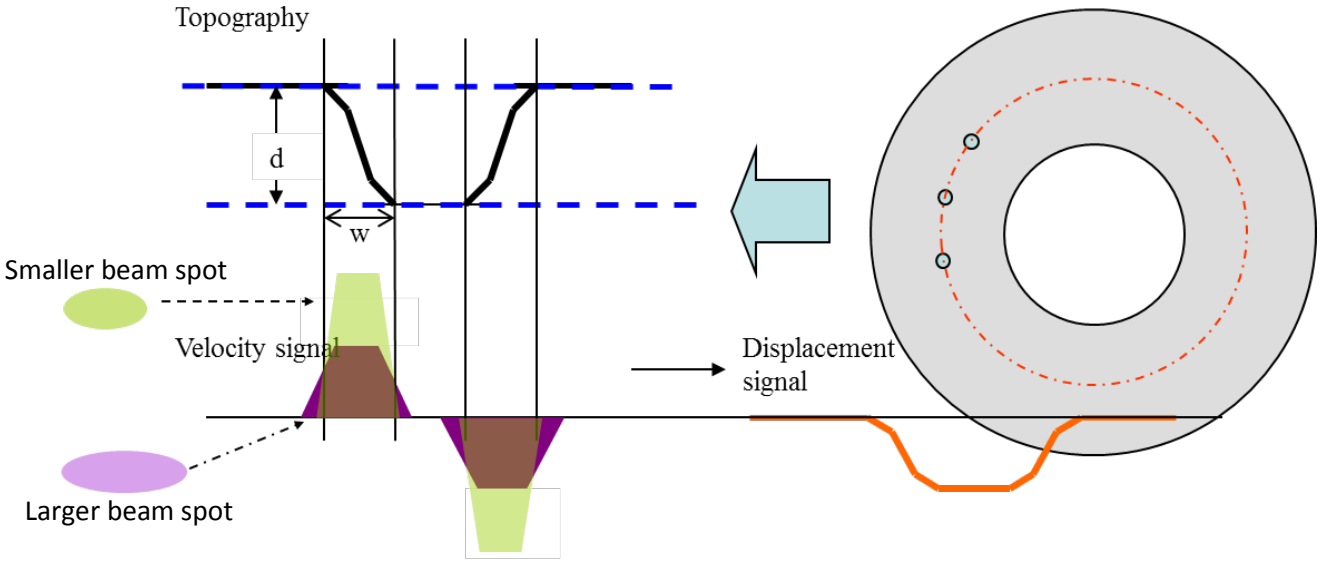

Figure 4-13: Illustration of LDV defect measurement

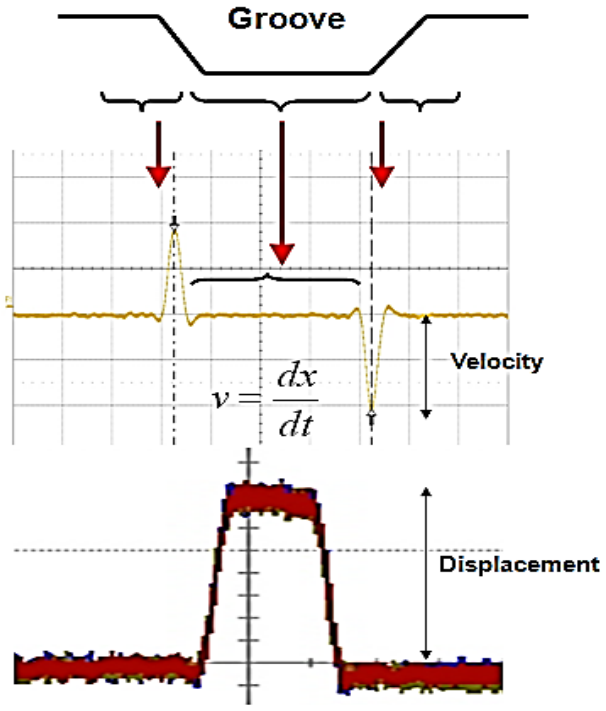

Figure 4-14: LDV signal of defect sample

To have simpler understanding of detection mechanism, the defect can be modeled as a regular rectangular groove or bump with physical depth, d and width, w. The velocity

measurement is sensitive to defect slope feature. Therefore, a velocity mode signal for a groove-shaped defect will produce two pulses corresponding to the slopes at the two slope edges. We can model the amplitude of pulse corresponding to a particular slope of velocity measurement as

$$V = \frac{d}{w} LV , \tag{4.7}$$

where V corresponds to detected velocity signal, d is defect depth, and w is defect slope width. LV is the linear velocity of rotating media. It can be seen that the deeper the defect, the smaller the defect slope width; and the larger the linear velocity, the larger the signal amplitude. For larger and deeper features, the displacement mode measurement is a better choice.

The resolution of a signal is determined by its amplitude and noise. There are several factors which affect the strength of signal amplitude in the LDV detection system. Firstly, the limitation from bandwidth capability of decoder system can affect the limit of spatial resolution. At higher RPM or for smaller feature width, non-linearity of signals can occur and signal amplitude may get saturated or reduced. Secondly, the effect of beam-spot size limits the capability of detection from the ideal case. Thirdly, the system noise level will affect the ease of detection capability if the signal amplitude is small. From theoretical calculation of (4.5), the detection limits of signal detection can be analyzed according to Figure 4-15.

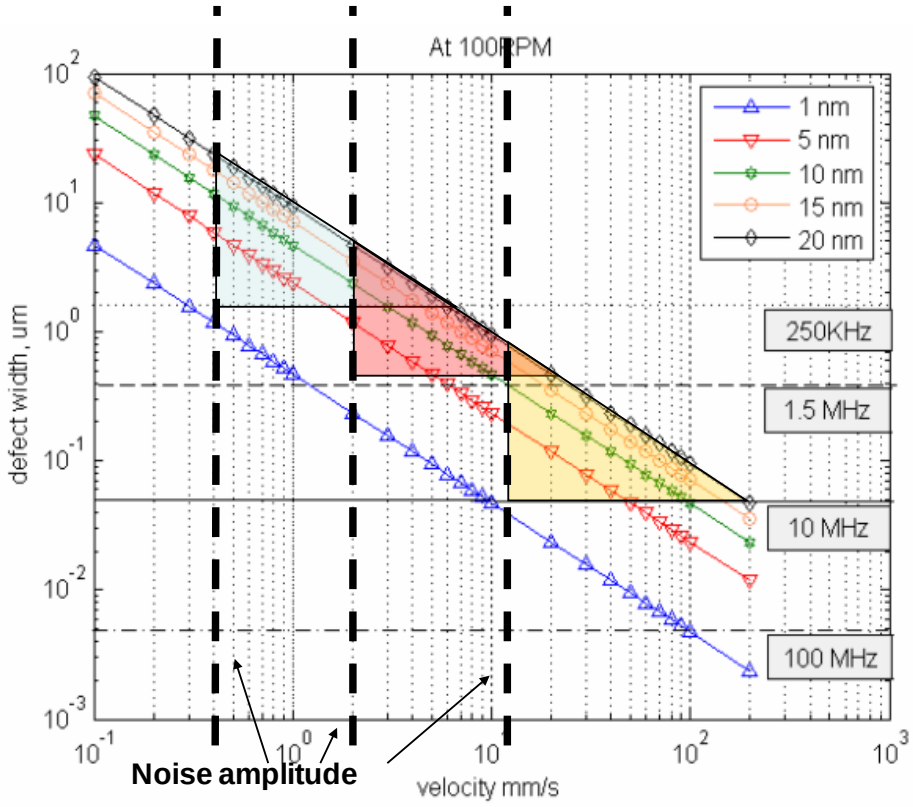

Figure 4-15: Computation of detection limitation by decoder bandwidth and noise.

Bandwidth limitation affects the spatial resolution of measurement. Feature slope width which is smaller than the decoder bandwidth limit will face signal saturation and thus superposition of signals occur which may result in signal nonlinearity. From Figure 4-15, the bandwidth limits are given by the horizontal lines. For defect slope width that is larger than the limit defined by the system's bandwidth (horizontal lines), the detection capability of system is sufficient. The defect slope width is calculated based on radius (1.75 inch) and linear velocity of 100 RPM, the calculated defect slope line represents the maximum velocity signal that can be obtained corresponding to both depth and width of defect feature. Therefore, the range of detectable defect slope width corresponds to the area between horizontal bandwidth limit line and the calculated defect slope line. The range of detection is further limited by system's noise. The vertical dashed black lines correspond to system noise as summarized in Table 4-1. Therefore, the detectable defect capability of the system is

defined by the shaded area (triangle) between the intersections of horizontal bandwidth limit, vertical noise limit and the calculated defect width line.

For a different decoder system, we can identify the respective detectable defect feature from its respective bandwidth specification and noise level. The summary of characteristics of different LDV decoders is shown in Table 4-1.

Table 4-1: Characteristics of different LDV decoders

	Velocity Decoder		**Displacement Decoder**	
Bandwidth (kHz)	0-250	0-1500	30-2000	30-2000
Amplitude Resolution (mm/s/V)	5	25	50	50
Noise level (mV)	117.8	180.52	100	100
Resolution	0.5 mm/s	5 mm/s	5 nm	5 nm

4.2.1.1 Velocity Measurement

Figures 4.16(a) and 4.16(b) show two velocity mode measurements of a 50 µm width and a 20 nm depth groove. As shown in Figure 4.16 (a), the lower amplitude resolution mode of 25 mm/s/V yields higher noise amplitude of 120 mV with smaller signal amplitude as compared to that of 5 mm/s/V. The higher noise amplitude is caused by higher frequency noise since the bandwidth of decoder at 25 mm/s/V resolution is 1.5 MHz compared to 250 kHz for 5 mm/s/V. The measured pulse width is consistent with the calculated value of 0.6 µs. With 25 mm/s/V mode, a higher spatial resolution can be obtained but with higher noise and smaller signal amplitude which is not desirable. In this case, averaging needs to be performed for good signal detection.

Figure 4-16(a): Velocity measurement 25mm/s/V, 5µm, 250 RPM, 20 nm (left)
Figure 4-16(b): Velocity measurement 5mm/s/V, 5µm, 250 RPM, 20 nm (right)

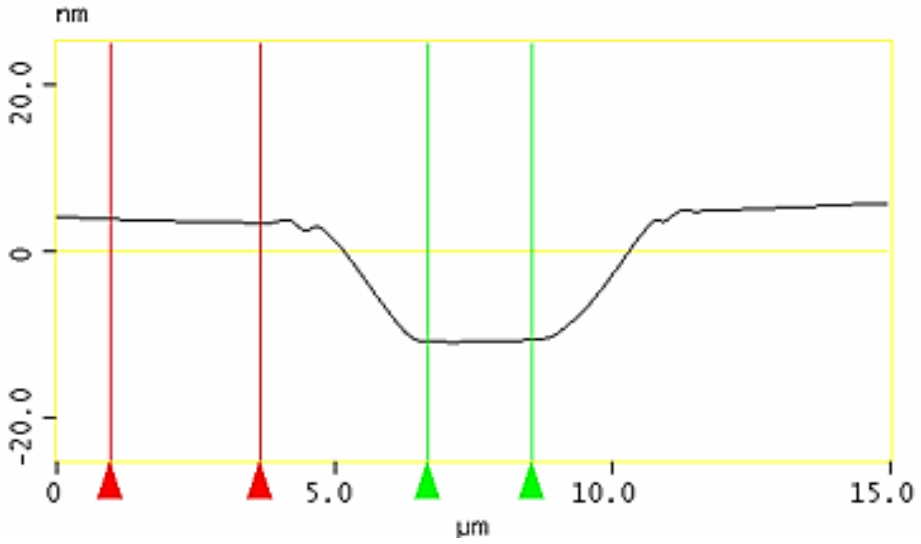

Figure 4-17: AFM measurement of groove profile

The Atomic Force Microscope (AFM) measurement shown in Figure 4-17 is obtained from a groove feature of 5 µm lateral width with measured slope width of approximately 1-2 µm. Based on (4.7), the noise amplitude limit is calculated as 1.89 µm (in terms of defect slope width) for 25 mm/s/V channel at a depth of 20 nm. On the other hand, noise amplitude limit (in terms of defect slope width) for 5 mm/s/V channel is calculated as 18.90 µm. The measurement verifies this result. We can see that the signal amplitude is comparable to the noise level for 25 mm/s/V mode. Considering the defect slope width is about 1-2 µm, the detectable velocity (amplitude) is near to the noise level, whereas the 250 kHz (5 mm/s/V)

give about full range of the amplitude for this size of defect's edge width. Without considering the beam spot size, the decoder with higher frequency response is more sensitive to smaller defect size. If ideally the defect size is smaller than beam spot, there would be reduction in signal amplitude. Reduction of measurement spot size will be a significant breakthrough to the barrier of measuring smaller defect size.

The signal pulse width is related to the change in linear velocity, defect slope width, and beam spot size. The decoder bandwidth limits the pulse width. Detection is still possible beyond the pulse width limit, but signal inter-pulse interference may occur. The pulse width study confirms the decoder bandwidth limitation on detected signal. At high RPMs, it can be seen that pulse width saturates at a calculated pulse period of 4.5µs and 1µs for 250 kHz (as shown in Figure 4-18) and 1.5 MHz (as shown in Figure 4-19) bandwidth, respectively. Comparing with the 250 kHz decoder channel, a higher decoder bandwidth of 1.5 MHz produces smaller pulse width of 1 µs.

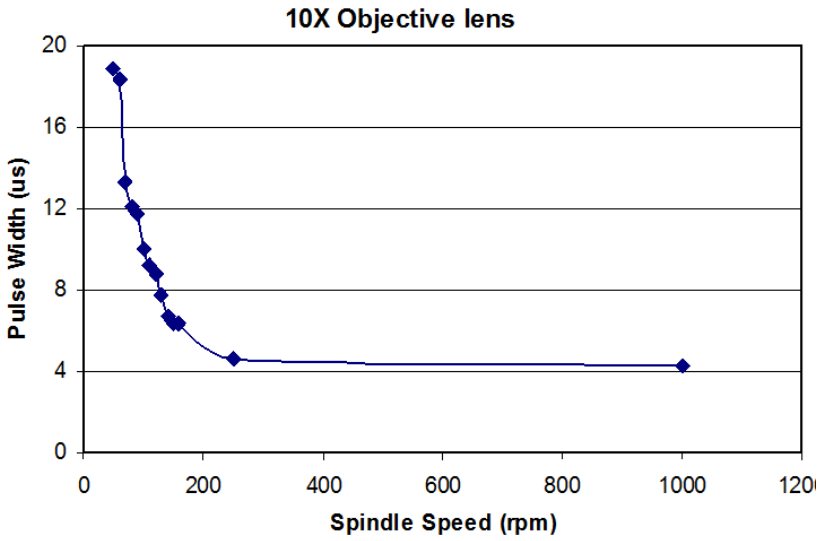

Figure 4-18: Pulse width, spindle speed, 10x objective lens, and decoder bandwidth of 250 kHz

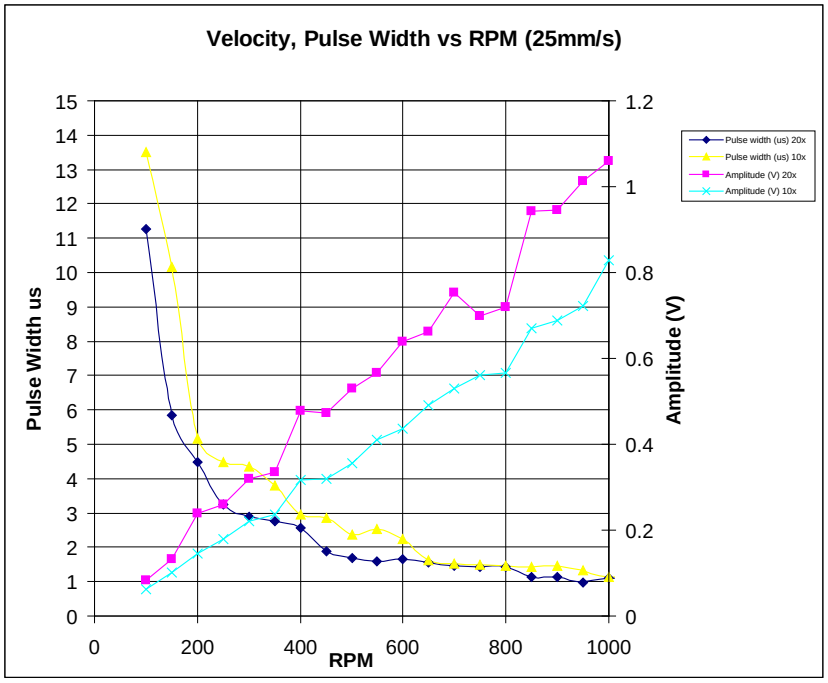

Figure 4-19: Pulse width, spindle speed, 10x & 20x objective lens, decoder bandwidth of 1.5 MHz

4.2.1.2 Displacement Measurement

Displacement measurement is performed using the OFV-2700 decoder which has bandwidth specifications of 2 MHz and 20 MHz. The displacement signal corresponds to the whole feature size, as compared to the velocity mode signal which is only sensitive to the defect slope. Figures 4-20(a) to 4-20(e) show displacement measurements at 1000 RPM. The aim of this study is to compare and quantify the signal amplitude of defects with different width and depth. The results illustrate that the amplitude of displacement signal decreases when either depth or width decreases. Figure 4-20(a) shows the displacement signal of different feature width at 50 nm depth. As feature width decreases, the amplitude of the displacement signal decreases. Figures 4-20(b) to 4-20(d) show the comparison of displacement signal of feature with different depth. As feature depth decreases, the amplitude of the displacement signal also decreases. Figure 4-20(e) shows that the detection of defect with 200 nm width and 20 nm depth is possible.

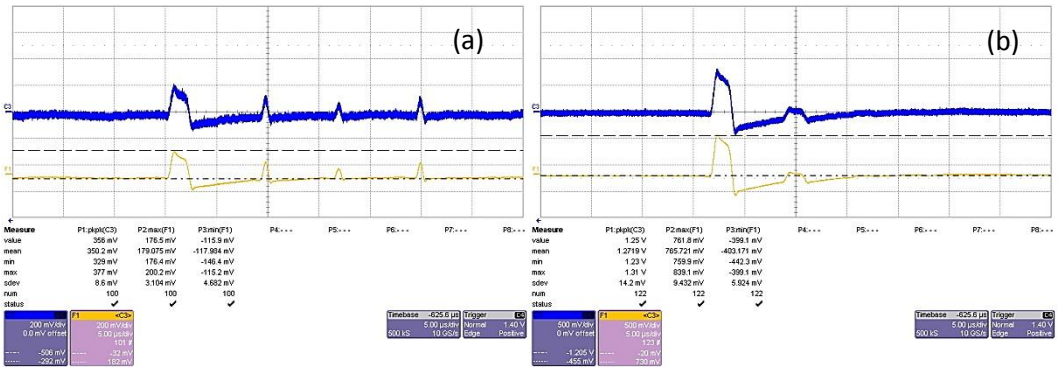

Figure 4-20(a): 1000 RPM, W: 5µm, 1µm, 0.5µm, 0.2µm, D: 50 nm
Figure 4-20(b): 1000 RPM, W: 5µm, D: 50nm, 20nm

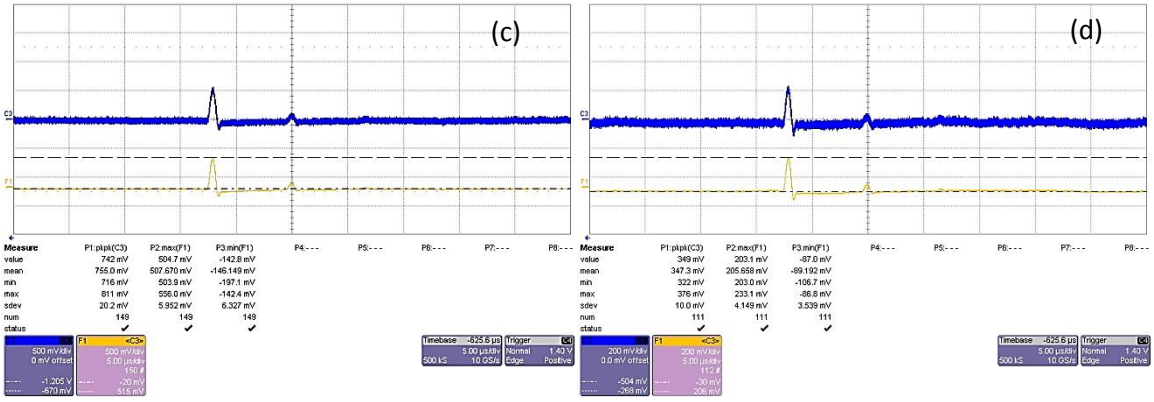

Figure 4-20(c): 1000 RPM, W: 1µm, D: 50nm, 20nm
Figure 4-20(d): 1000 RPM, W: 0.5µm, D: 50 nm, 20 nm

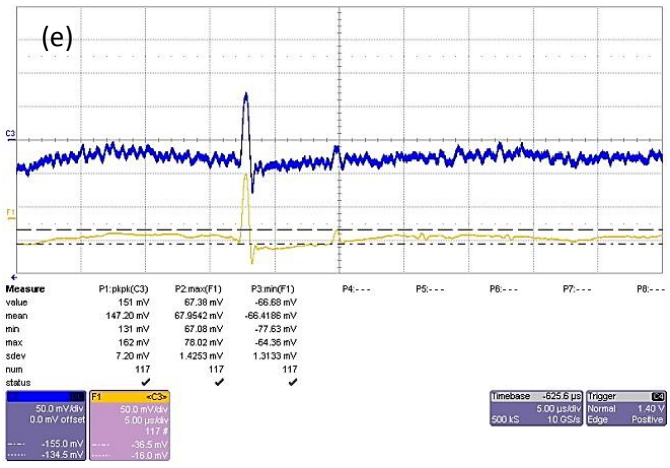

Figure 4-20(e): 1000 RPM, W: 0.2 µm, D: 50 nm, 20 nm

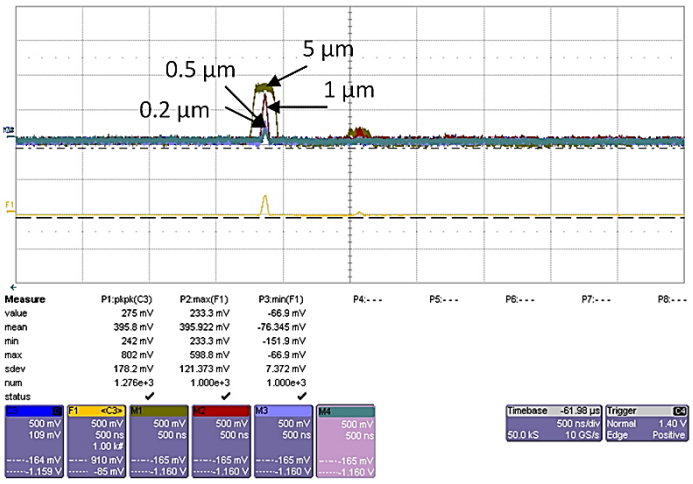

Figure 4-21: 10000 RPM, W: 5 µm, 1 µm, 0.5 µm, 0.2 µm. D: 50 nm, 20 nm, 10 nm, 5 nm.

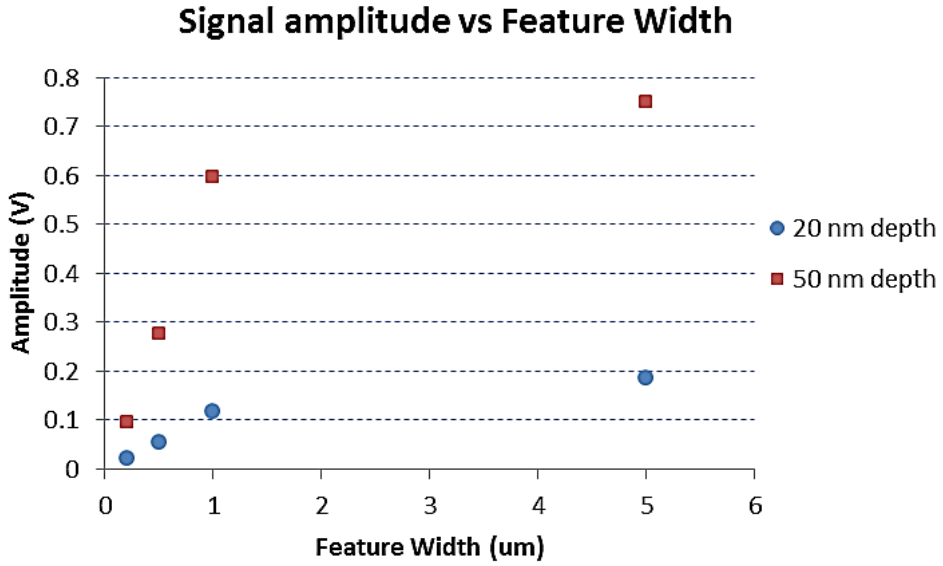

Figure 4-22: Signal amplitude vs feature width

While velocity measurement maps the defect slope feature (sensitive to slope change), displacement measurement maps the whole defect feature (sensitive to depth). The signal amplitudes in Figure 4-21 are plotted and shown in Figure 4-22. As depth decreases, the amplitude of signal decreases almost linearly (approximately 3 times). With the decreasing feature width, the amplitude of signal decreases further. Figure 4-23 shows the measurement of defect at 5000 and 10000 RPM using a decoder with 20 MHz bandwidth. It can be concluded that the signal amplitude of higher bandwidth decoder does not depend on the

spindle RPM. This is because the decoder bandwidth has far enough resolution capability for the available feature sizes.

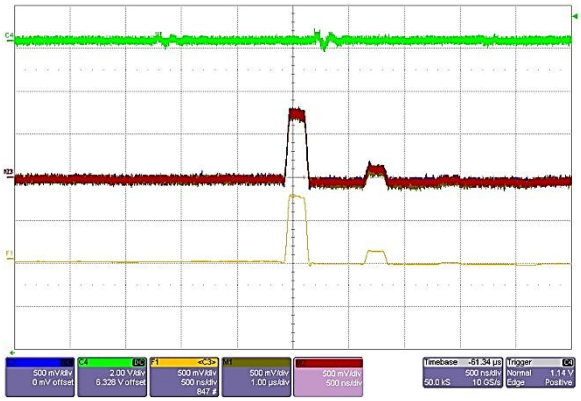

Figure 4-23: 20 MHz decoder, 5000 & 10000 RPM, amplitude comparison

Figures 4-24(a) and 4-24(b) show the effect of decoder bandwidth on the output signal shape. It can be seen that for the 20 MHz decoder, the amplitude of signal does not decrease even at higher linear velocities. The amplitude reduces if a lower bandwidth decoder is used. This is due to decoder bandwidth limitation as well as the low-pass filtering effect of the 2 MHz output signal. The lower bandwidth constitutes a low pass filtering effect in which the signal experiences time delay and distortion due to higher *RC* constant. Figures 4-24(a)-(b) illustrate the effect of decoder bandwidth on signal shape and amplitude with defect measurements of different depths.

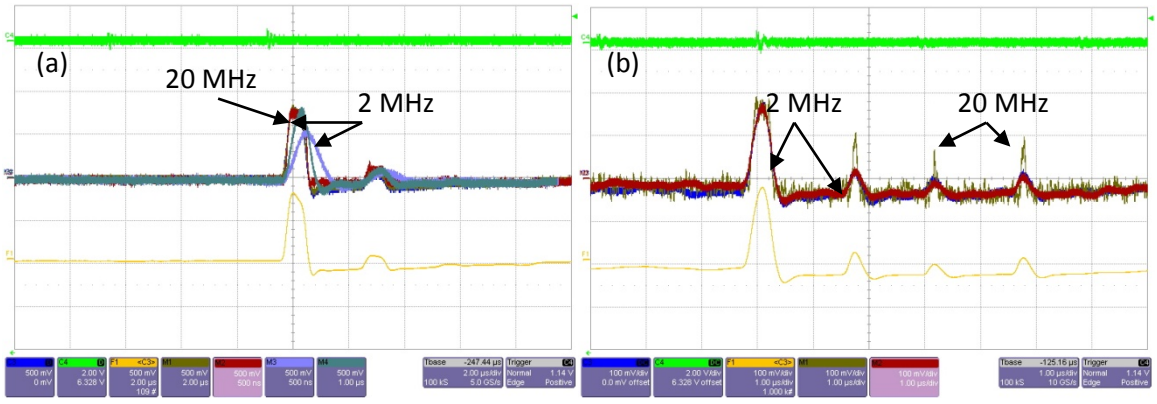

Figure 4-24(a): 5000 RPM D: 50nm, W: 5µm, 1µm, 0.5µm, 0.2µm
Figure 4-24(b): 10000 RPM, D: 50nm, W: 5µm, 1µm, 0.5µm, 0.2µm

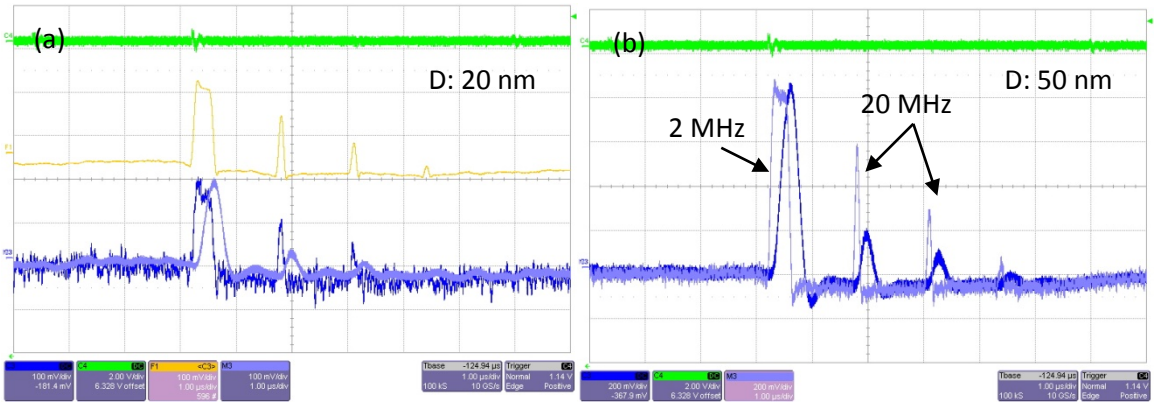

Figure 4-25(a): 5000 RPM, D: 20 nm, 20 & 2 MHz
Figure 4-25(b): 5000 RPM, D: 50 nm, 20 & 2 MHz

4.2.1.3 Detection of Feature Width of 200 nm and Below

The aim of this study is to evaluate on LDV methodology to achieve similar detection resolution of the OSA. Figures 4-26(a) and 4-26(b) show the detection of feature width of 100 nm and 80 nm respectively with 20 nm depth using velocity mode 5 mm/s/V at 500 RPM.

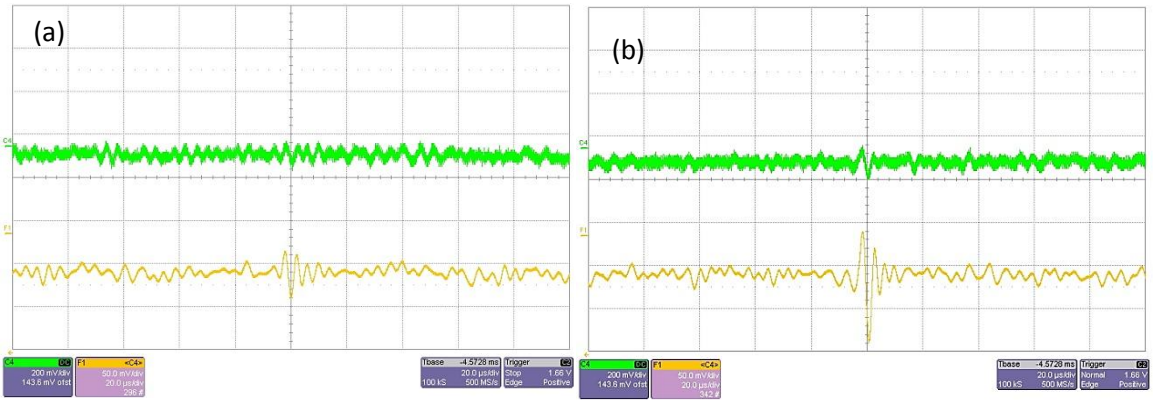

Figure 4-26(a): Velocity D: 20 nm, W: 80 nm
Figure 4-26(b): Velocity D: 20 nm, W: 100 nm

It can be seen that although detection limit of such small features has been greatly exceeded, the detection of signal is possible with multiple averaging. Figure 4-26(b) shows that detection of a 20 nm depth and 100 nm width feature is still very distinct compared to the

background noise. On the other hand, detection of a 20 nm depth and 80 nm feature becomes difficult due to its small amplitude which is comparable to the background noise.

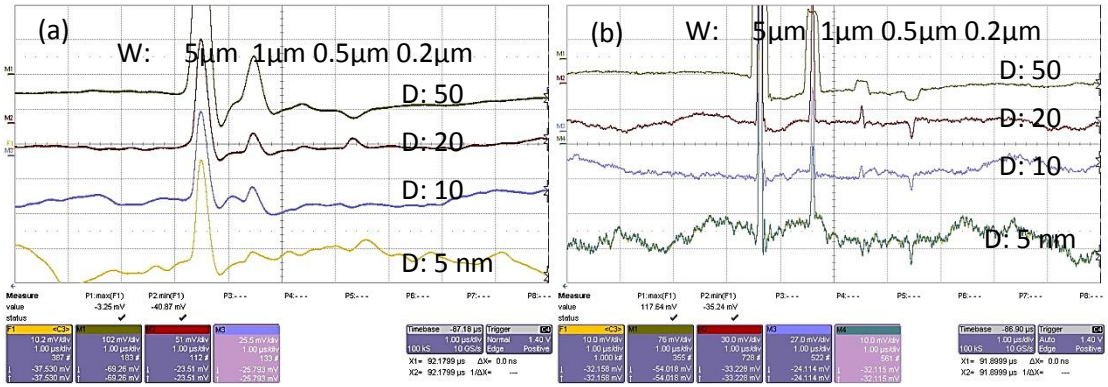

Figure 4-27(a): 2MHz decoder BW (7200 RPM)
Figure 4-27(b): 20MHz decoder BW (7200 RPM)

As shown in Figure 4-27(a), small defect features of 500 nm width and below cannot be resolved with 2 MHz channel at 7200 RPM but is possible to be resolved with 20 MHz channel (Figure 4-27(b)). In order to increase the ease of detection, the sensitivity of decoder can be increased, for example, from 50nm/V to 20nm/V.

4.3 Enhanced LDV detection

Due to limitations of LDV detection capability (limited by the beam spot size), the detection of very small defects less than 1 µm is possible but is relatively difficult. We introduce a new method which enhances LDV detection capability to resolve feature sizes up to 200 nm (W) x 5 nm (D). In this case, the downtrack spatial accuracy is not of main importance. The method should be able to distinguish different types of defect with reasonable precision in downtrack positioning. Figure 4-28 is an example of LDV displacement raw signal of four defect features with different width and depth. The x-scale represents time in downtrack direction and the y-scale represents signal amplitude in Volts.

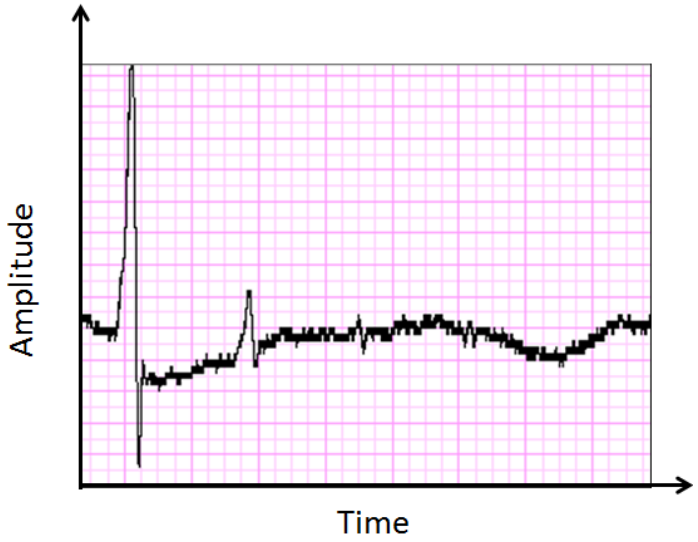

Figure 4-28: Displacement raw signal with 200nm width and various depths

The LDV measurement is sensitive to low frequency information due to disk runout and microwaviness. A defect feature which is smaller than the amplitude of this modulation may be positioned at different DC level.

The method eliminates the low frequency signal morphology by implementing a polynomial line fit. In our method, it is useful to define a small error moving window y_m, in the downtrack direction. The advantage of this is that signal morphology is linear within a small window and it is easy to perform line-of-best fit. More importantly, we enhance the error signal by squaring and accumulating this information across the whole downtrack scanning range. It can be seen that the defect information is now greatly enhanced. By doing surface mapping, it is now possible to detect the difference. The following algorithm is proposed to enhance the detection amplitude of raw LDV signal. Firstly, we define a detection window with time range of x_0 to x_n with the corresponding signal amplitude y_0 to y_n. Line-fit is then performed using a linear line model

$$y_{fn} = ax_n + b\,, \qquad (4.8)$$

where y_{fn} is the fitted line and

$$a = \frac{n\sum xy - \left(\sum x\right)\left(\sum y\right)}{n\sum\left(x^2\right) - \left(\sum x\right)^2}, \tag{4.9}$$

$$b = \frac{\sum y - a\left(\sum x\right)}{n}. \tag{4.10}$$

Applying least-square algorithm, the enhanced data point is given by

$$y_m = \sum_{i=0}^{n}\left(y_n - y_{fn}\right)^2 . \tag{4.11}$$

An illustration of the algorithm is shown in Figure 4-29. Subsequently, this algorithm can be easily implemented real-time via digital signal processing.

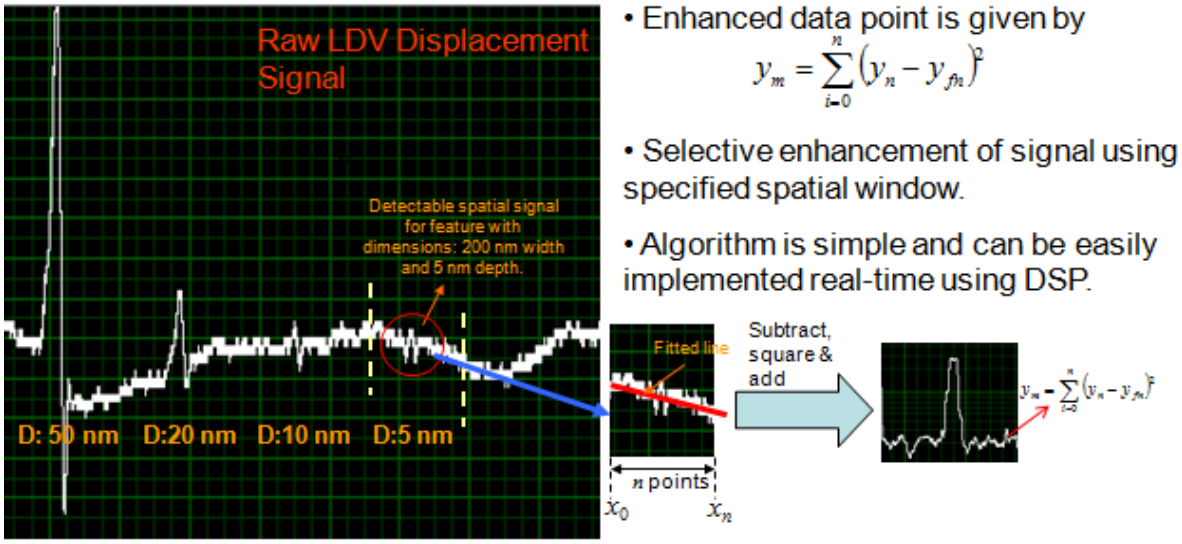

Figure 4-29: Illustration of LDV signal enhancement technique

This method considers a defined window according to the wavelength scale of interest (according to defect), performs first order line fitting, obtains the difference (error) to eliminate any DC, squares the error, and represents every pixel as sum of all errors within the window size n. Figure 4-30 shows the enhancement result.

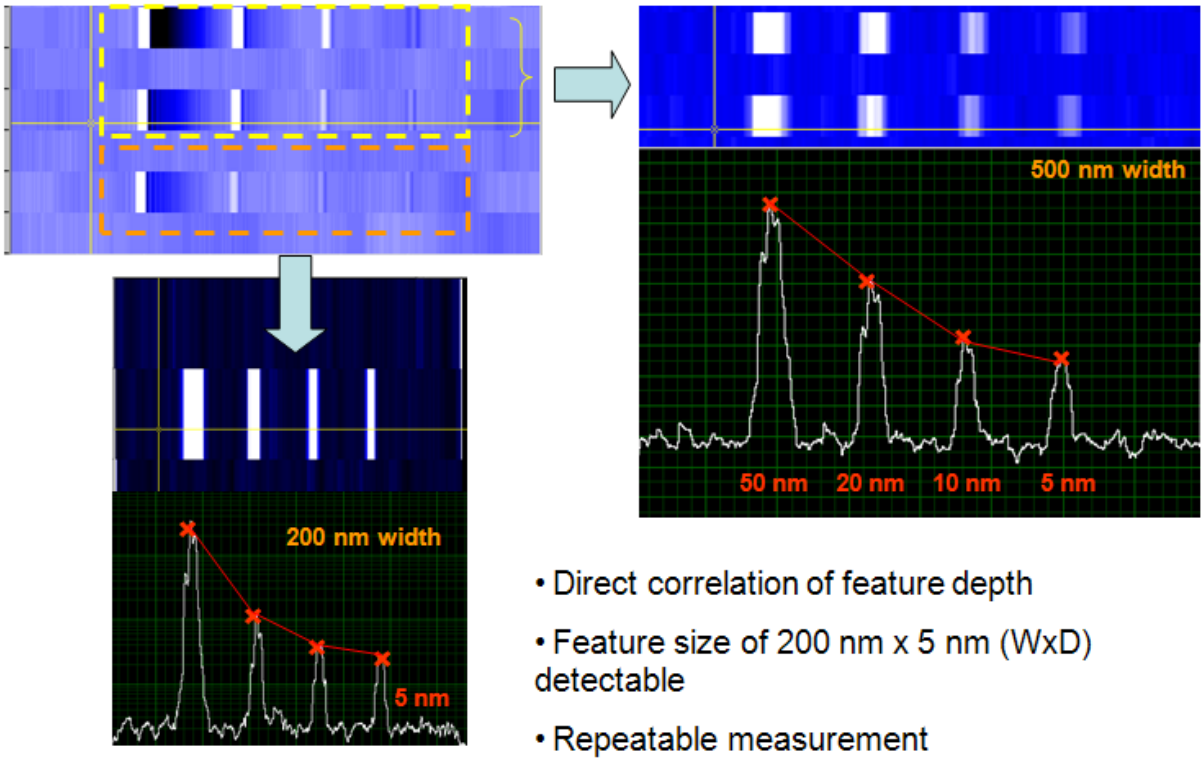

Figure 4-30: LDV enhancement result

The enhancement algorithm gives repeatable measurements with direct correlation of the feature depth. As shown in Figure 4-30, feature size of 200 nm width and 5 nm depth can be clearly resolved and detected.

4.3.1 Comparison of LDV Line Profile and OSA Line Profile

The KLA Tencor OSA6100 Optical Surface analyzer (OSA) and Polytec LDV OFV-2700 are used to compare defect detection capability. Figure 4-31 shows OSA imaging of the fabricated defect sample. Q-phase and P-specular optical channels are used to analyze lubricant and carbon overcoat layers. As shown in Figure 4-32, cross sections are drawn across the image and values of reflectivity are extracted for analysis. It is observed that the relative amplitude of OSA is not consistently distinct as compared to LDV. Surface feature between each defect is not distinguishable. It is also observed that as feature width decreases,

resolution of detection amplitudes of both OSA and LDV decrease. This is due to the limitation in optical beam spot size.

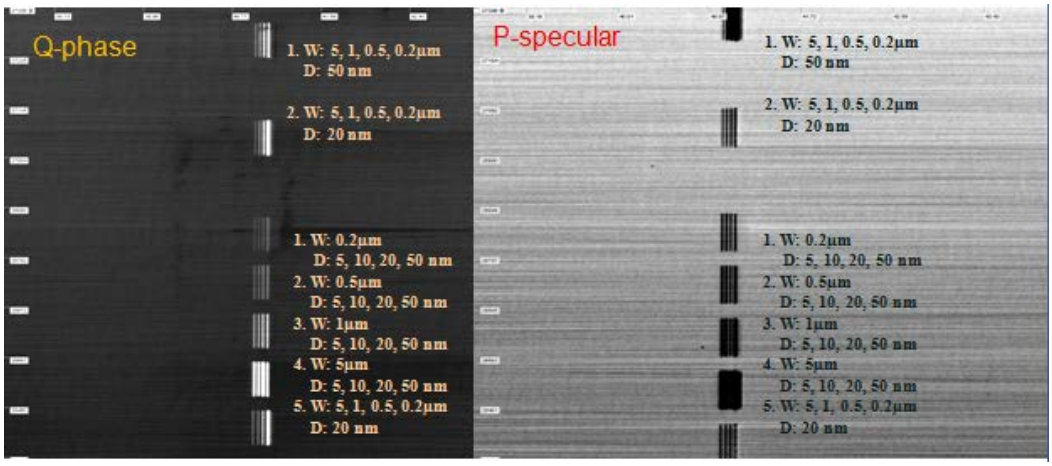

Figure 4-31: OSA images Q-phase and P-spec of the fabricated defect features

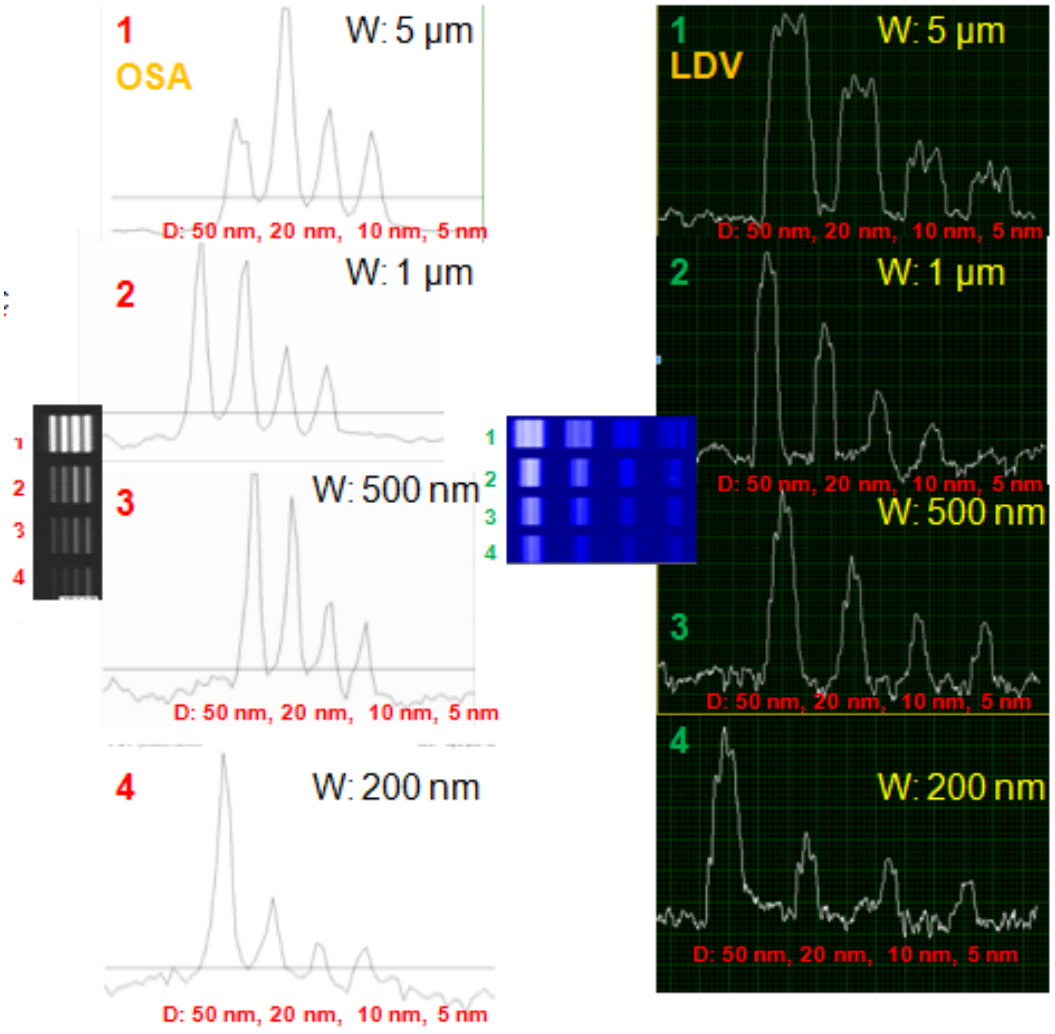

Figure 4-32: Line profile of OSA versus enhanced LDV detection

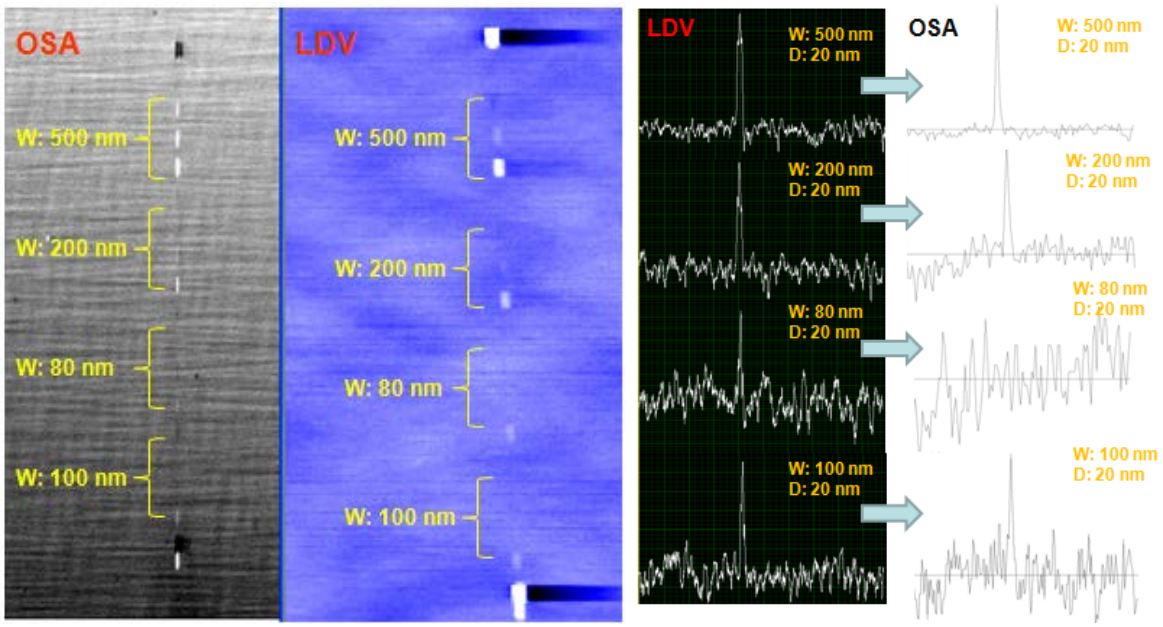

Figure 4-33: Comparison of OSA and LDV for feature widths between 80 nm to 500 nm

Measurement is also performed for smaller feature width ranging from 80 nm to 500 nm width and 5 nm to 20 nm feature length. From the results in Figure 4-33, it is shown that detection of defect feature less than 100 nm width and 20 nm depth is possible with the LDV. OSA detection also reaches its limit for detection of 100 nm width feature and below. Reduction of beam spot size is critical for optical detection of 50 nm and below. The result in Figure 4-33 shows the detection capability of displacement decoder with 2 MHz and 20 MHz channels at different RPM. It can be seen that the smallest feature of 200 nm width and 5 nm depth can be detected by the system with multiple averaging and small amplitude. For 20 MHz, the signal contains high frequency components. The interesting feature from the result is that signal waviness can be obtained (which may correspond to surface roughness), after averaging.

4.4 Media Defect Certification using LDV and MP

Magnetic recording media goes through a variety of final tests before the component is being sent to hard drive assembly line for integration with the head stack assembly (HSA). The process of final tests adds to final cost of production [52]. This cost is attributed to the high cost of test equipment, test heads and labor. Typically, tests usually consist of glide tests to scan asperities, parametric tests to scan for magnetic properties, and flaw scans to test for magnetic defects. As areal density of hard disks increases, bit dimensions on hard disks decrease correspondingly, leading to increased testing time. Conventional media testers for head based certification typically use a flying head with a read sensor to perform glide testing and flaw scan [52]. In order to obtain high resolution, the read sensor needs to be narrow, resulting in longer testing time. The scanning parameter is determined from the width of the reader. The time required to scan per disk is

$$t = \frac{d}{d_r \times rps}, \tag{4.12}$$

where t is time, d_r is the reader width, d is the scan distance per disk, and *rps* is the number of revolution per second.

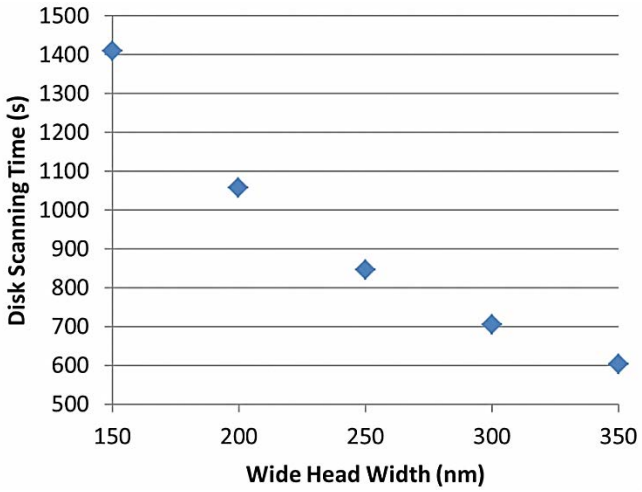

Figure 4-34: Disk scanning time versus read head width

The result is plotted and shown in Figure 4-34. For a read sensor width ranging from 150 to 350 nm, a complete or full measurement time to cover disk radius from 0.6 to 1.6 inch at 7200 RPM will take 10 to 23 minutes, if only one certification head is used. As bit dimension further reduces, read sensors will correspondingly be narrower, resulting in even longer testing times for full disk scanning. In a typical media fabrication process, head based media certifiers are used to detect defects on disk media. As an alternative to head based certification, optical based certification using a Laser Doppler Vibrometer (LDV) provides shorter testing times as shown in Figure 4-35 due to the use of a larger beam spot that allows each disk to be completely tested more quickly. Use of scanning interferometry was reported as early as 1986 by Bogy *et al* [53].

In this work, detection and measurement of defects with lateral size of approximately 500 μm is developed. Since then, increased areal density demands higher resolution detection. In recent years, efforts are being carried out by companies such as THÔT Technologies, KLA Tencor Optical surface analyser, *etc*; to increase defect detection resolution to sub-nm level. Despite the efforts, optical certification has a disadvantage of reduced resolution due to the larger spot size. Furthermore, the detection capability of LDV-based detection is less than that for head based certifiers. Optical certifiers are therefore not usually used alone for defect detection of hard disks. Head-based certifiers are more commonly used although optical certifiers are gaining importance as increasing disk densities will lead to longer certification times required by head based certifiers. Use of optical method to perform disk defect certification offers great time saving and cost. As scan pitch decreases, the time taken to scan per disk increases. For optical certification, scan pitch is closely related to the beam spot size. Let the beam spot diameter be d_b, the required scanning steps needed is

$$step = \frac{d}{d_b}, \tag{4.13}$$

and the scanning time required is

$$time = \frac{step}{rev/s}. \tag{4.14}$$

The testing conditions are 7200 RPM at scanning range of 1 inch. The result is plotted and shown in Figure 4-35.

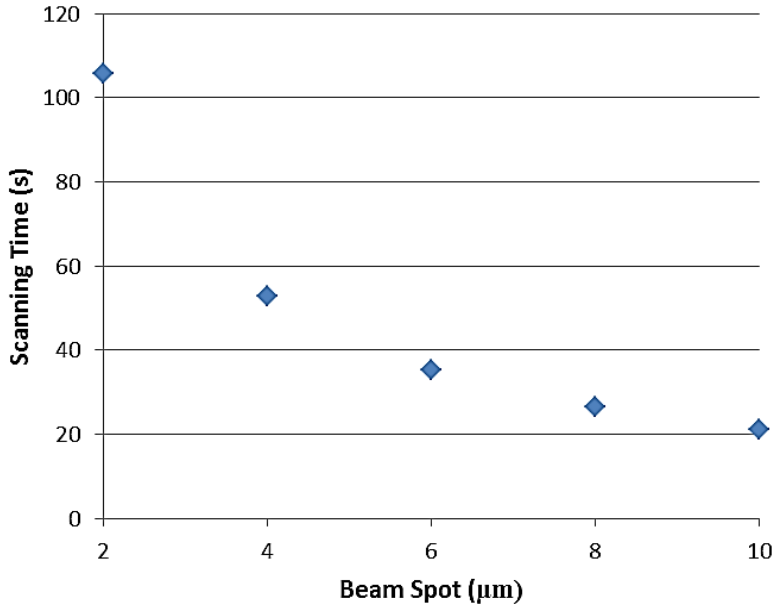

Figure 4-35: Disk scanning time versus beam spot size

Comparing with Figure 4-34, optical certification offers ten times faster scanning time than the read head-based scan.

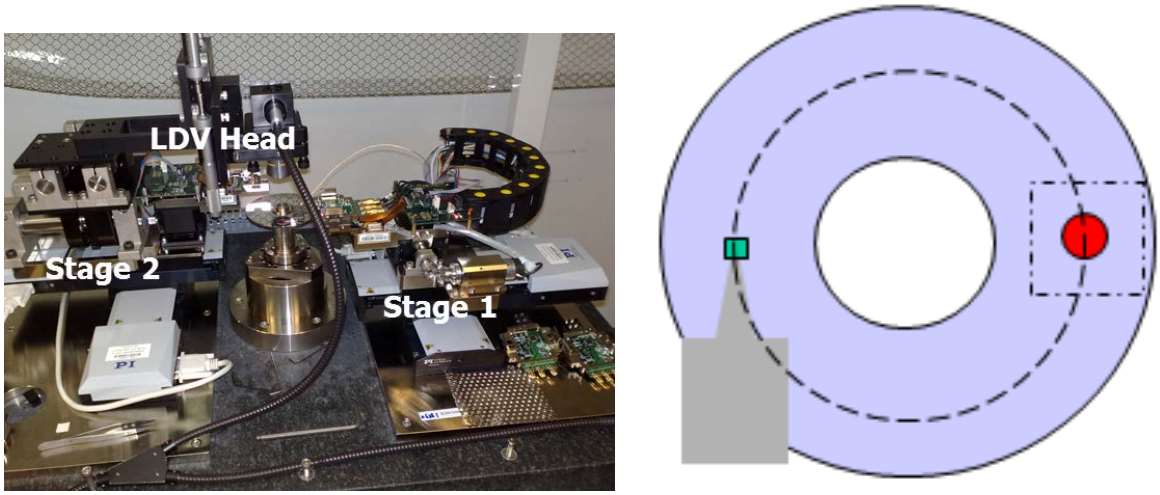

Figure 4-36: Simultaneous measurement setup of LDV and MP for defects certification

The integrated spinstand uses single read head mounted on stage 1 and LDV head on stage 2 as shown in Figure 4-36. Here the LDV beam spot is 180^{o} out of phase from the read head and is positioned along the same track. Assuming the pair of linear stages is perfectly orthogonal to each other; relative positioning of one stage can be easily set to follow the other. However, correlation of read head position and LDV beam spot needs to be verified to ensure that they are both at the same track. A calibration method is proposed. This method uses a specially prepared feature, *i.e.*, a series of groove or laser bumps as shown in Figure 4-37. Here, measurements are performed on laser zone region with 2.66 MHz sampling time and 24000 samples. The scanning step is 300 nm.

Laser bump features are clearly visible. Figure 4-37 shows the calibration position in which LDV position is 180^{o} away from the read head. This is verified in time domain as shown in Figure 4-38. Concurrent scanning of both MP and LDV are obtained, and the special-prepared feature is being identified. Adjustment of positioning is carried out while comparing exact images of the two measurements. Calibration positions of the two pairs of linear stages are also recorded. Subsequent movement of magnetic read head or LDV can be compensated for with respect to the calibrated original positions. Calibration is done only once for every batch of disks.

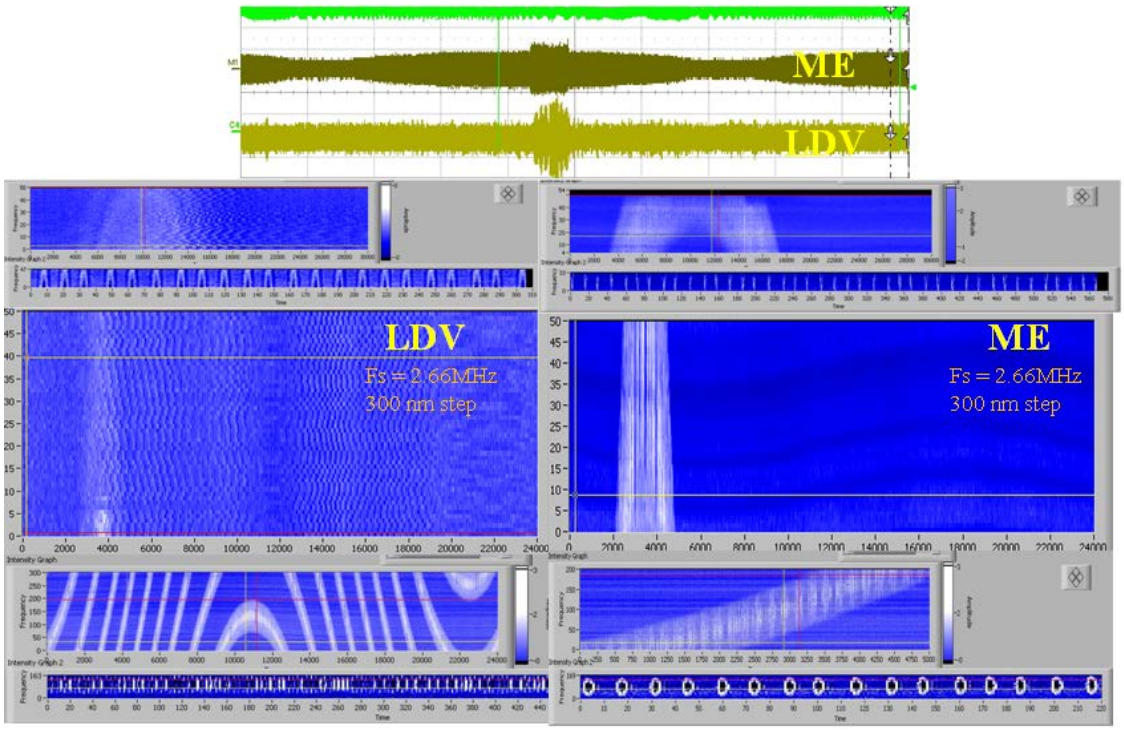

Figure 4-37: Scanning of laser bumps using LDV and MP

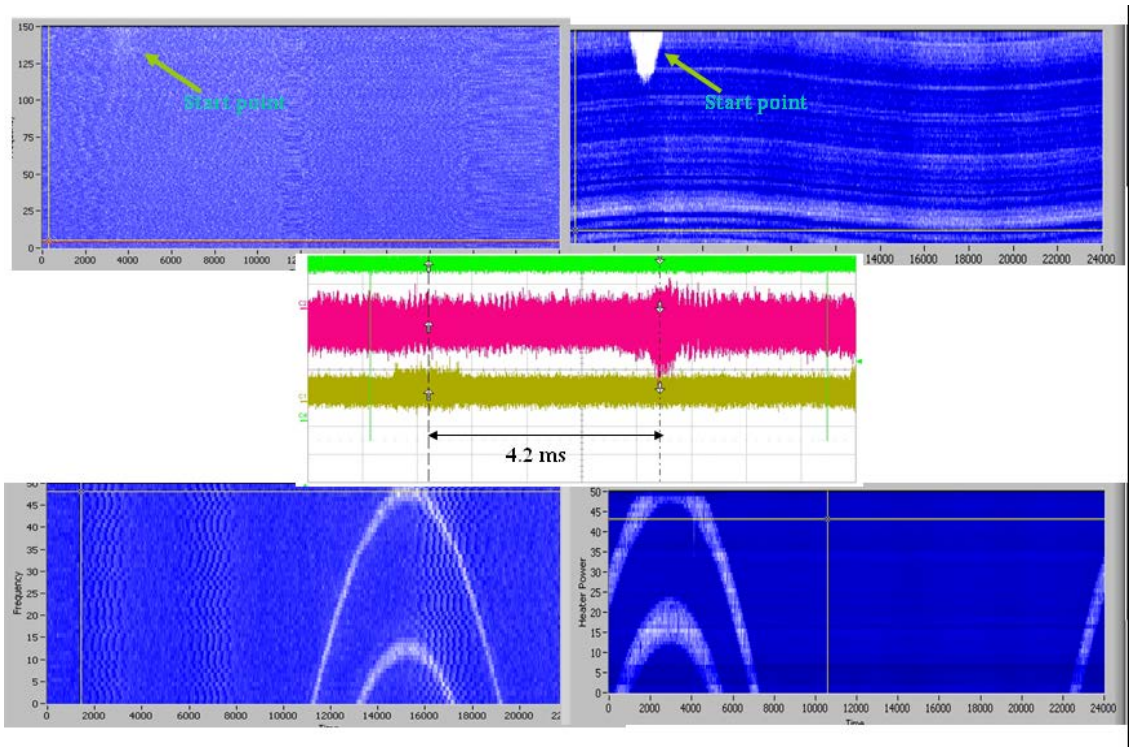

Figure 4-38: Scanning calibration of defect certification

4.5 Measurement of Slider Dynamics.

A key variable of fly-height is the protrusion of the read/write element towards recording media. Protrusion changes with temperature and read/write duty cycle. Thermal Flying Height Control enables direct control of the head read/write element protrusion using an integrated heating element in the head, leading to more consistent spacing between head and disk. When current is applied to the heater element, heating will cause materials at the pole tip region to expand. In this way, reader element can be brought nearer to the disk surface. The amount of current applied to achieve the required change in flying height can be computed from design parameters and simulation. In magnetic recording systems, the slider flies on disk surface with linear velocity of 15-30 m/s. Due to cooling effect of airflow on slider, the degree of pole tip protrusion reduces.

In view of this, the implementation of thermal flying height control has to be performed and measured after head-media integration. The main method is to calibrate the applied heater power versus changes in flying height. Flying height computation is usually performed through the touch down test. Slider touch down or contact on disk surface will cause head to wear or damage disk, resulting in potential loss of data. This excites slider and suspension resonance which often results in head disk crash. In this section, head instability measurements due to contact induced vibration is being measured and characterized.

4.5.1 Defects and Slider Dynamics

The missing pulse method showed a high resolution defect detection capability. However, as the methodology depends on the flying read head, it is found to be susceptible to spurious information. Figure 4-39 presents the concurrent LDV and missing pulse measurement carried out on the tester. Besides the specially fabricated defects of different widths in both mappings, the missing pulse map shows a rectangular dark region compared

to a thin line feature in the LDV. Based on the missing pulse alone, it is not possible to identify the defect or disturbance. The LDV map of the disk surface with testing spot just ahead of slider reveals the nature of the defect in this case a scribe mark made by OSA for marking. This shows that measurements based on one single method is subject to spurious effects that may be misinterpreted. By combining the information from the two concurrent mappings, the nature and extent of the defects can be made clear.

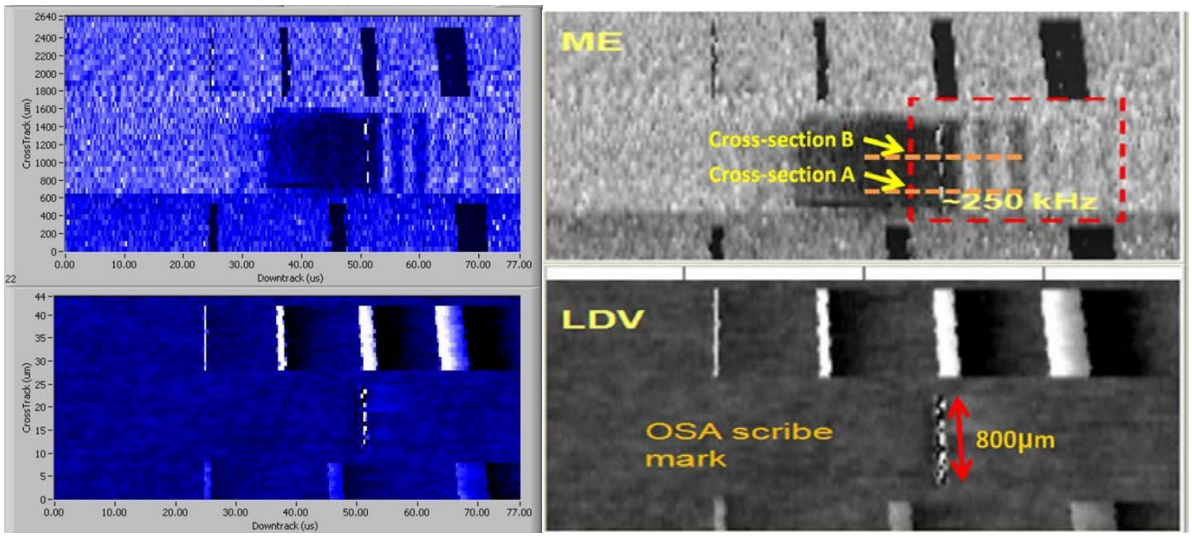

Figure 4-39: Mapping of MP and LDV of defect media surface.

Beside proper characterization of disk defects, concurrent measurement also provides information on measurement conditions. In Figure 4-39, once the OSA scribe mark defect has been recognized in the LDV scan, further information relating to slider and its flying instabilities can be obtained from the missing pulse mapping. Measurement was performed using a pico-slider of dimension 1 mm width and 1.25 mm length. This scribe mark is 800 µm wide. It becomes obvious that the apparent elongated dark region in the missing pulse mapping is not a defect but arises from the slider interaction with the OSA mark. Since resulting feature is a convolution between the interacting features, it first experiences an increase in flying height or head-media spacing, as the envelope signal in the missing pulse is

reduced (darker contrast). The onset of the dark region is the point where the flying slider or part of flying slider first experiences significant surface interactions. The end of the region is when the interacting slider part "clears" the defect.

The missing pulse signal is proportional to the readback amplitude. Assuming the MP signal drop is purely due to head media spacing increase; we can use the readback equation to compute changes in head-media spacing. Generally, the relationship between the amplitude of readback signal *V(t)* of a sinusoidal recorded signal and the head media spacing *d(t)* at time *t* [35] is given by (4.15)

$$V(t) = C \exp\left(-\frac{2\pi d(t)}{\lambda}\right), \qquad (4.15)$$

where C is a positive constant and λ is the wavelength of the signal. Figures 4-40 (a) and (b) show the changes in magnetic spacing at the onset of slider interaction with the defect edge (cross section of readback signal along cross sections A and B in Figure 4-39). It is seen that the slider dynamics at cross section A (partial interaction) and cross section B (slider is fully interacting with defect) is different. The former shows the onset of cross-track interaction where only a small area of slider is interacting and changes in magnetic spacing are gradual. When a larger part of slider interacts with the defect, a sharp change in magnetic spacing is observed.

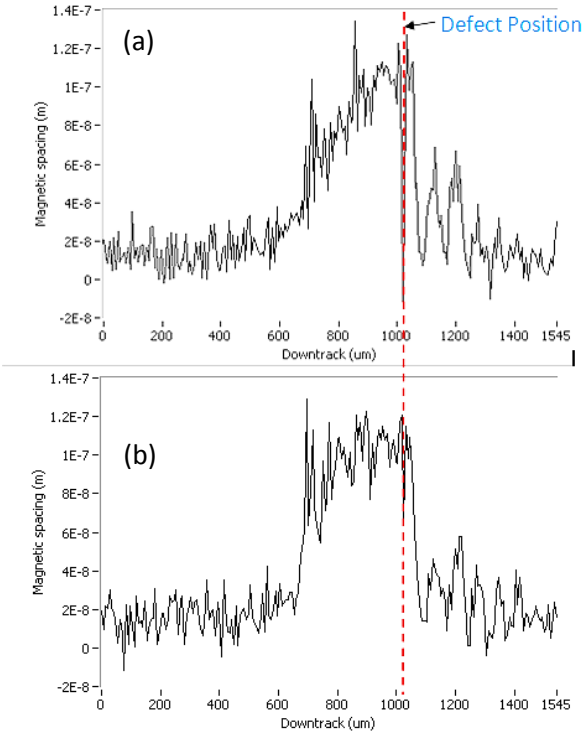

Figure 4-40(a): Magnetic spacing change at cross section A of figure 4-39
Figure 4-40(b): Magnetic spacing change at cross section B of figure 4-39

Because the obtained measurement is a mapping across different disk radii, it is now possible to estimate the size of the interaction region from both cross track and down track information, unlike single time domain MP or LDV captured at a single disk radius. In addition, the latter also reveals the dynamic flying instabilities of the slider (alternating light and dark lines of down track fly height modulations in the MP map). These can provide information on the slider vibration modes. In Figure 4-40(b), the alternating lines are calculated to be 250 kHz for a 7200 RPM disk rotation. These modulations are attributed to the pitch mode of the slider, and are excited when the slider is flying over the defect.

The developed setup allows for up to four concurrent channels. Figure 4-42 presents simultaneous MP, LDV, AE, and in-situ FH measurements of a random defect on a disk. The total mapped area is 23.1 mm (horizontal downtrack direction) and 1.75 mm (vertical cross track direction). For this measurement, the LDV probes the disk defect immediately ahead of the slider while the AE sensor is attached very close to the slider suspension. Both MP and in

situ FH are based on the readback signal from the read sensor. The sampling frequency used for data acquisition is 10 MHz and disk RPM is 7200.

Figure 4-41 shows that although the measurements are at the same defect area, different information can be obtained from different testing techniques. The LDV probes the disk directly and in this case is the most accurate (mechanical) representation of the defect. Comparing the MP and in-situ FH measurements, similarities are observed in that large contrast features are observed at the onset of the defect. Both MP and FH measure variations in the magnetic readback signal, which are influenced by changes in read sensor-media spacing. One interesting point is that the onset of strong AE response is different. This head-media spacing is already changing before the read sensor reaches the defect in the LDV measurement. The onset of strong AE signal, on the other hand, is delayed until the defect itself and it does not reveal information on the flying slider prior to the defect. Here, concurrent mapping provides valuable timing information on the occurrence and sequence of interactions.

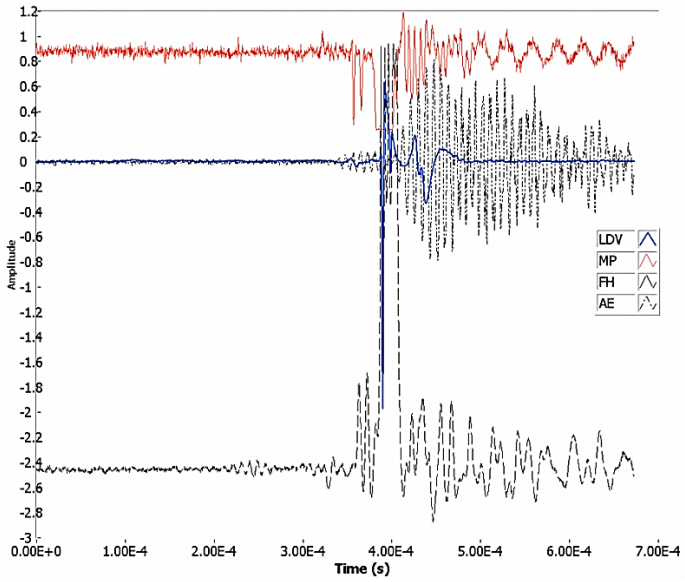

Figure 4-41: Concurrent measurement profile taken at the defect region

From the measured frequency spectrum, 120 and 250 kHz are modes attributed to slider's roll and pitch, respectively. The roll mode vibration pivots near the slider's center from the leading edge (LE) to the trailing edge (TE) as shown in Figure 4-42(a) and the pitch mode vibration pivots near the slider's longitudinal center as shown in Figure 4-42(b). The resonance frequency of a slider is specific to a particular slider design. In our experiment, the slider's resonance modes are characterized by placing the LDV beam spot at various locations as shown in Figure 4-42. To determine pitch mode frequency, the LDV beam spot is positioned at the trailing edge of the slider's body and to determine roll mode frequency, the LDV beam spot is positioned at the longitudinal corner of the slider.

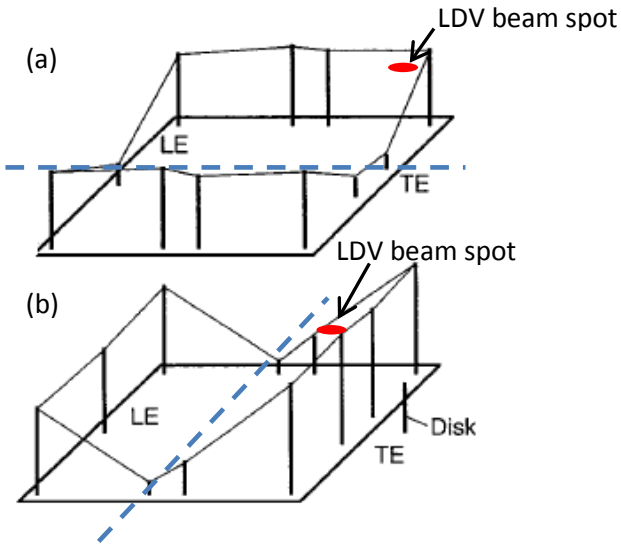

Figure 4-42 (a): Slider's vibration - roll mode
Figure 4-42 (b): Slider's vibration - pitch mode

In subsequent experiments, the LDV beam spot is placed at the trailing edge center. The pitch and roll frequency of the slider used in this experiment is similar to that measured by Knigge and Talke [23]. The lower 120 kHz mode corresponds to the modulations observed in the AE measurements in Figure 4-43 while the slider pitch modulation at 250 kHz corresponds to that in the MP measurement in Figure 4-39. It is thus shown that different defects can excite different slider vibration modes, and that different measurement techniques possess different sensitivities in different scenarios. The selectivity depends on the defects

encountered. One future work is to use this concurrent measurement setup to further study the nature of the defects and their selectivity to different vibration modes.

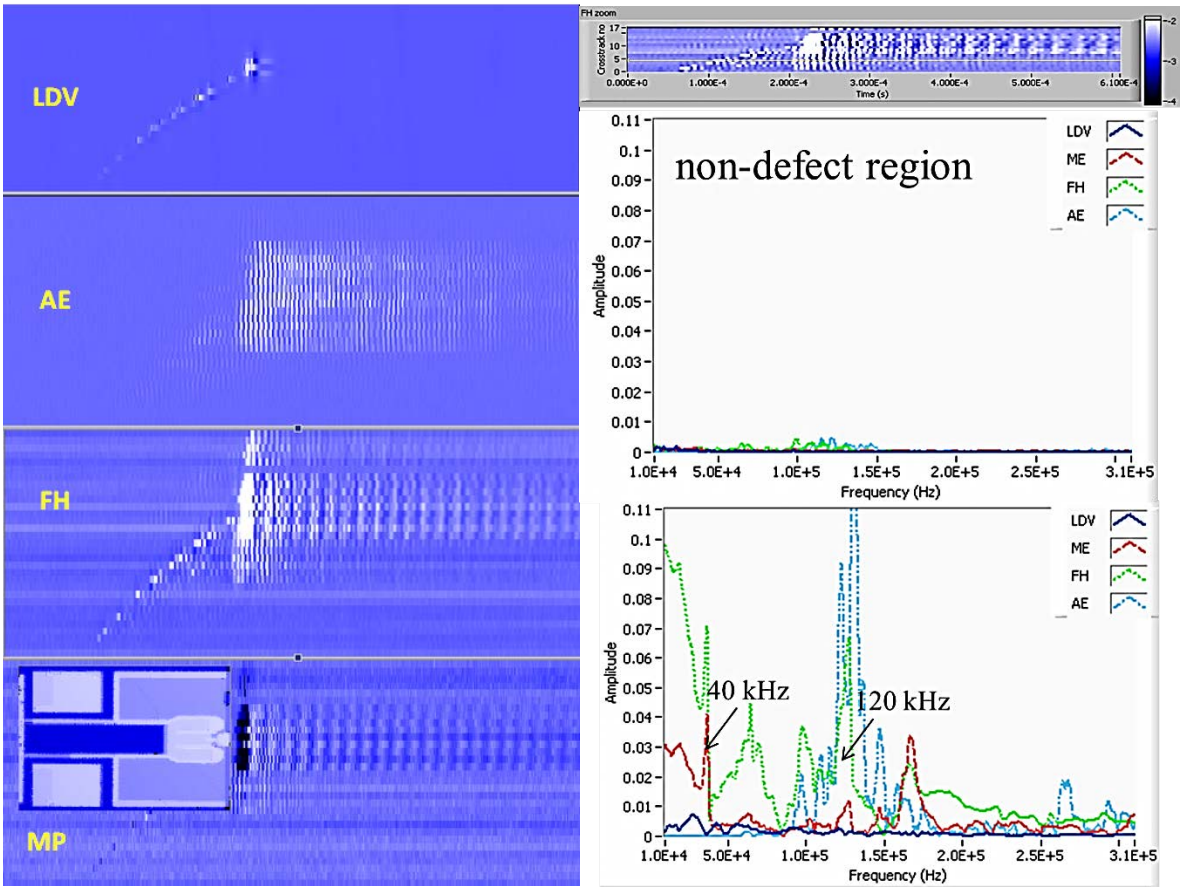

Figure 4-43: Frequency spectrum slider dynamics interaction with defect

Another difference between the measurements is that the AE modulations are of different frequencies as compared to that of the MP and in-situ FH. In addition, the AE modulations decayed rapidly while the MP and in-situ FH continue to show sustained slider flying instabilities. These differences clearly indicate that the AE measures flying stabilities of a different nature than that shown by MP and in-situ FH. In our experiments, both missing pulse and in-situ FH are more sensitive to flying dynamics than AE measurements. This is evident from their ability to strongly detect the small defect dots prior to the large defect, as well as measuring the sustained flying instabilities beyond the AE signal decay as seen in Figures 4-41 and 4-43. It is observed by Zeng *et al* [19] that in some situations, using a sub-

10 nm slider, there is little or no observable AE signal but carbon overcoat starts to wear off. Between in situ FH and MP, the former appears to provide marginally better resolution. Figure 4-43 shows the frequency spectrum around the defect region where, both in situ FH and MP detection reveals frequency modes at 37 kHz while AE detection shows mainly a vibration mode at 120 kHz.

4.5.1.1 Magnetic Defect Enhancement through In-situ FH and MP Measurements

Magnetic defect detection can also be enhanced through concurrent in situ FH and MP measurements (Figure 4-44). In-situ FH measurement uses triple harmonic ratio to obtain information of magnetic spacing. Therefore, this method is less sensitive to readback amplitude dropout due to magnetic variations from media defects. On the other hand, the MP is proportional to the magnetic signal strength which is affected by both magnetic defects and flying height change. Taking these detection sensitivity differences into account, the contribution to MP from missing magnetic information (caused by media defects) can be accentuated if FH information can be subtracted from that of MP. Magnetic spacing information can be obtained from MP signal by applying Wallace's Equation in (4-10). Here, a writing frequency of 40 MHz is used which corresponds to wavelength of 400 nm. Simple subtraction is subsequently performed after flattening both images with respect to their respective background level, followed by normalizing both images. The resulting contrast enhancement is shown in Figure 4-44 (c). When compared to flattened and normalized LDV measurements of the defect at the same scale as shown in Figure 4-44 (d), it can be concluded that portions of mechanical defect may not cause magnetic defects.

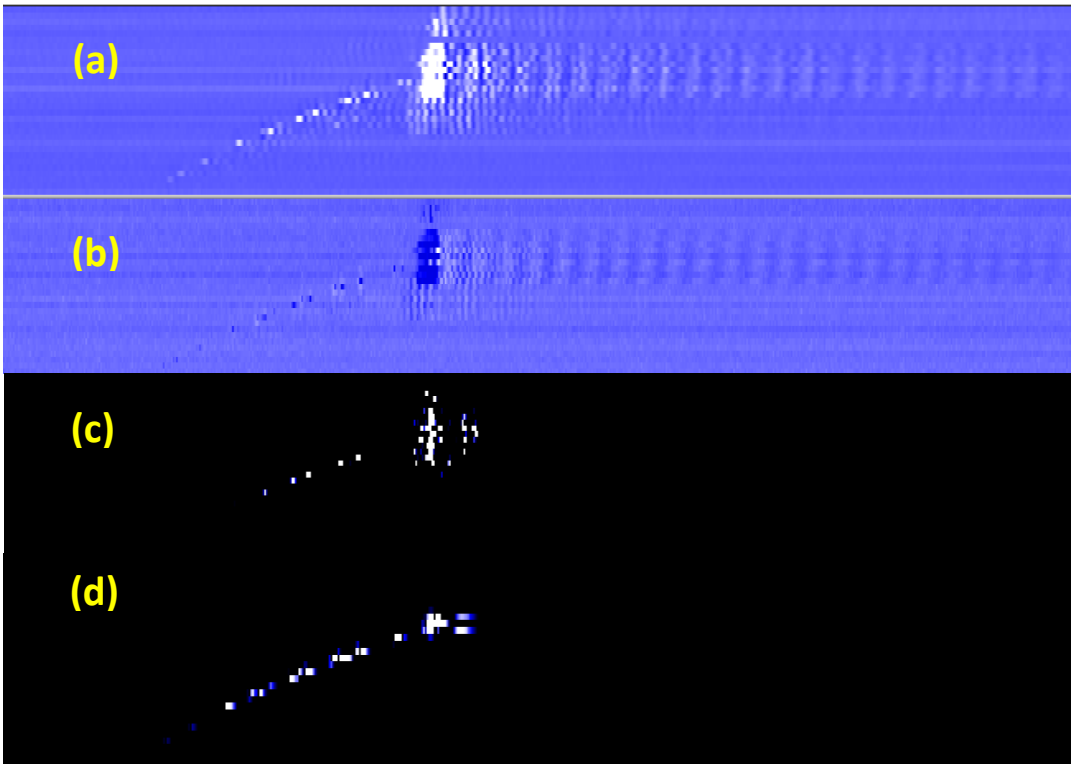

Figure 4-44(a): Flattened and normalised FH image
Figure 4-44(b): Flattened and normalised MP image
Figure 4-44(c): Normalised enhanced magnetic defect detection
Figure 4-44(d): Flattened and normalized LDV signal of defect

4.5.2 Contact Induced Slider Dynamics using Thermal Protrusion

From the perspective of thermal fly height control (TFC); such two-dimensional mapping can be applied for the study and characterization of thermally actuated protrusions, especially the changes in interaction region size and nature of slider/disk interactions when TFC is applied. One way is to use a known and specially fabricated disk feature which is much smaller than the protrusion area of the TFC slider. The special feature can probe and map out the thermal activated protrusion.

4.5.2.1 In-situ FH Measurement

In-situ FH measurement has been a well-known technique to measure head media spacing using readback signal harmonic ratio. For longitudinal recording, the use of 111100

pattern [36], provides strong first and third harmonic to increase measurement accuracies. The harmonic of readback signal can be modeled as:

$$V(k) \propto e^{-kd} \frac{1-e^{-k\delta}}{k\delta} \frac{\sin(kg/2)}{kg/2} \quad , \qquad (4.16)$$

where $V(k)$ is the readback signal harmonics, C is a constant, k is wavenumber, d is head media spacing, a is the media transition length parameter, δ is media thickness, and g is the head gap length. Due to effect of gap loss and media thickness loss, the relationship with head media spacing is nonlinear. By taking ratio of the two readback harmonics, the loss terms can be eliminated and thus linear relationship of head media spacing can be obtained as

$$d = -\frac{3\lambda}{4\pi} \ln\left(\frac{V_3}{V_1}\right), \qquad (4.17)$$

where V_1 is the first harmonic, V_3 is the third harmonic, C is a constant, d is head media spacing, and λ is the wavelength. Harmonics of readback signal can be obtained by computing the Fast Fourier Transform (FFT) using digital signal processing. This method can be easily implemented, but the measurement is slow and cannot be conducted in real time. Figure 4-45 introduces a measurement setup for flying height measurement.

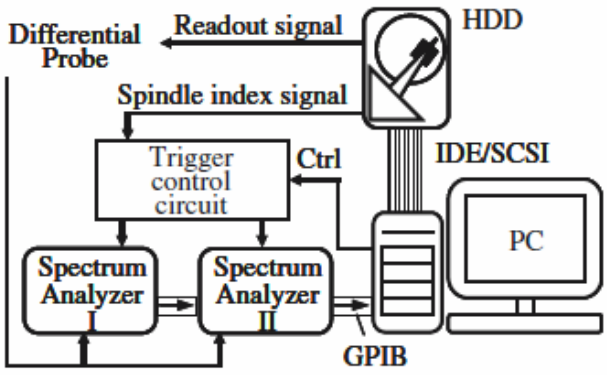

Figure 4-45: Experimental set-up for flying height modulation measurement

In this setup, two spectrum analyzers are utilized to obtain the harmonic amplitudes of readback signal. Spectrum analyzers use analog electronics to obtain signal harmonics. Zero span configuration of the spectrum analyzer can produce very fast measurement of readback signal harmonic which is more superior to FFT method. The disadvantage of this method is that the setup is bulky and expensive.

Analog in-situ FH electronics has been developed by the Data Storage Institute in 2006. This technology implements two channels programmable analog filter which output signal proportional to the two harmonic amplitudes of a readback signal. With a customized analog implementation, the system's bandwidth is designed to be in the order of hundreds of MHz. This produces very fast computational response. This analog signal is then furthered processed through an analog logarithmic amplifier and produces final output analog waveform which is proportional to $\ln\left(\frac{V_{ch1}}{V_{ch2}}\right)$. With calibration using a spectrum analyzer, the output waveform represents real time in-situ FH signal which has bandwidth sufficient to detect slider dynamics characteristics. Figure 4-46 shows an experimental setup that was adopted by Xu *et al* [55] as an external testing module to test variations of head medium spacing for different batches of heads.

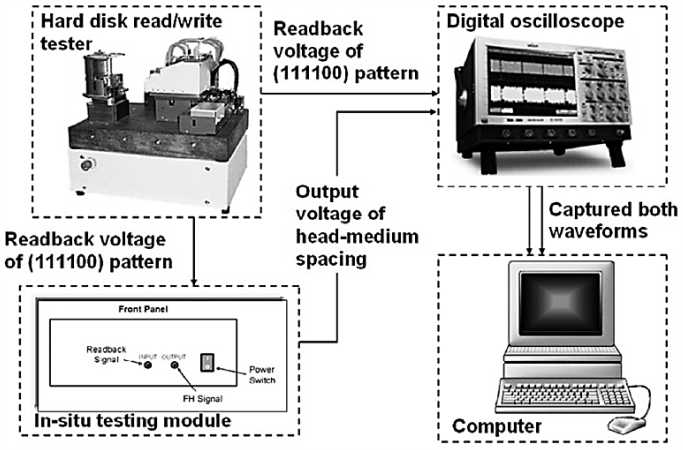

Figure 4-46: Real time in-situ testing FH module

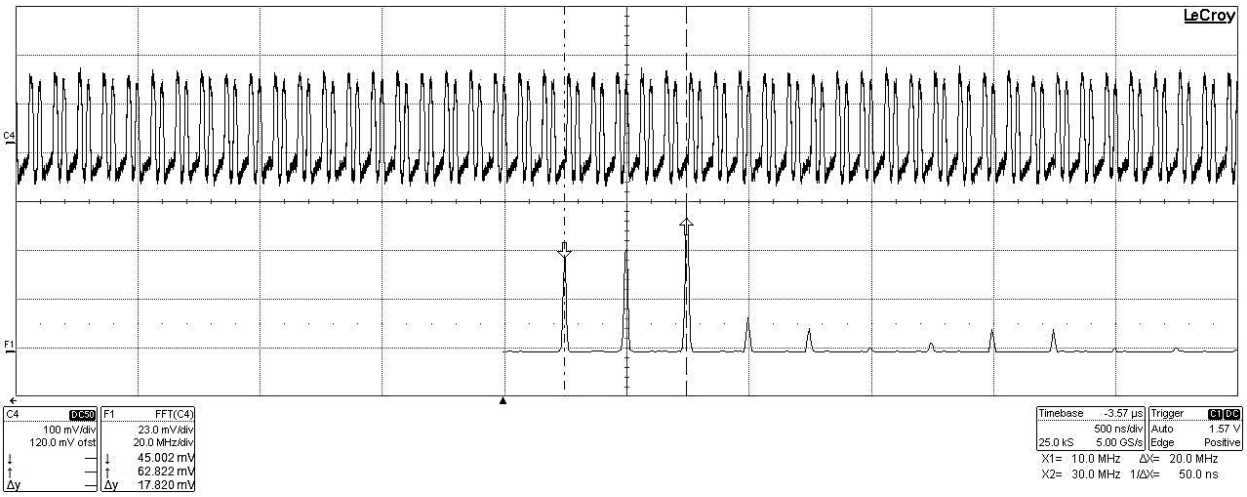

Figure 4-47: 1111 00 code pattern for FH testing

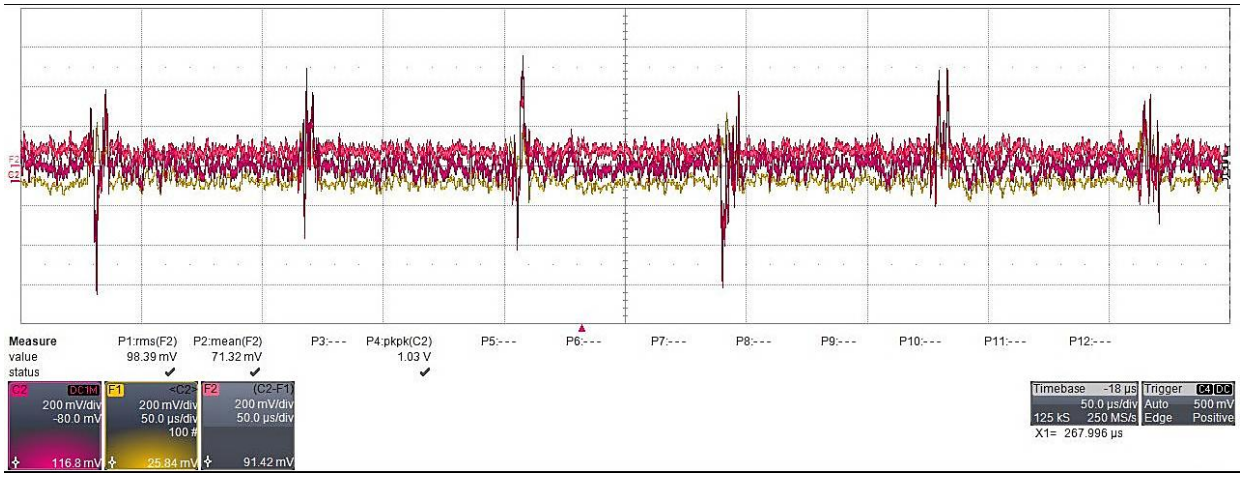

Figure 4-48: Real time in-situ FH signal

An example of readback 111100 testing code written on the test track is given in Figure 4-47. It can be seen that the first and third harmonics of the readback signal are of comparable amplitudes. The processed real time flying height signal is shown in Figure 4-48. A study by Yuan *et al* [56] showed that triple harmonic method cause about 1 nm or 3% testing error due to changing write current with ±20% pulse asymmetry and 50% off-track conditions.

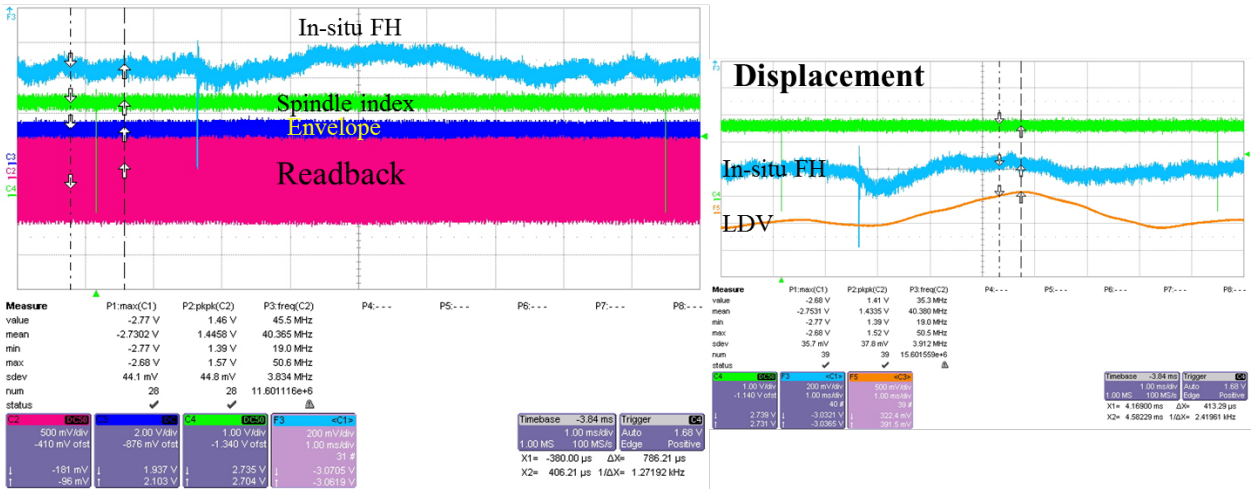

Figure 4-49: Low frequency disk runout measurement of in-situ FH

In-situ FH measurement as shown in Figure 4-49 shows correlation with LDV displacement measurement. According to Ng *et al* [16], this corresponds to slider's flying height variation due to disk clamping distortion. Here, the LDV beam spot is positioned on the same track as the read head and is slightly ahead of slider.

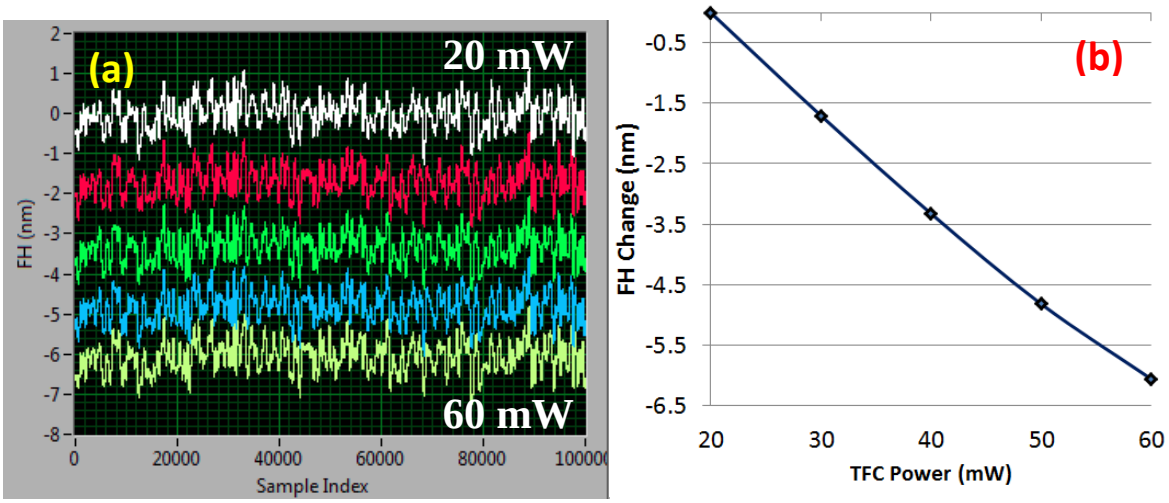

Figure 4-50: Touch down testing

Similarly, the mean real time FH signal across a large segment of the track can be used to compute relative FH more accurately. Figure 4-50(a) shows the change in FH signal level when TFC power is increased from 20 mW to 60 mW. FH change can thus be computed from (4.17) and as shown in Figure 4-50(b).

4.5.2.2 Acoustic Emission

The acoustic emission testing is a powerful method for examining the behavior of materials deforming under stress. Acoustic emission is transient elastic wave generated by the rapid release of energy within a material. AE sensors respond with good sensitivity to motion in the low ultrasonic frequency range. It basically detects acoustic waves that are generated by sudden movement in solid materials. In our study, mini AE sensors with bandwidth of 500 kHz are sufficient to detect slider related vibration dynamics. Signal generated by the sensor is further amplified using a wideband AE pre-amplifier. Both AE sensor and amplifier are shown in Figure 4-52. The AE sensor is attached to HGA mount close to the HGA as shown in Figure 4-51.

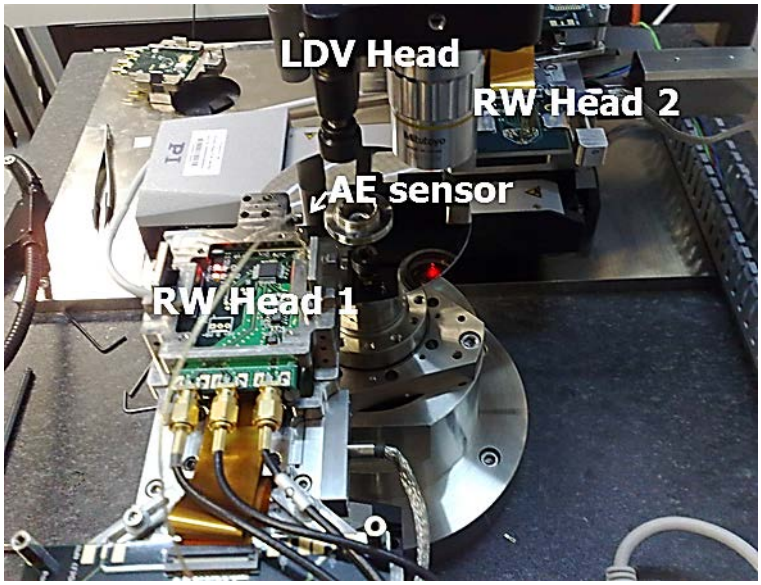

Figure 4-51: Measurement setup of slider dynamics study

Figure 4-52: Acoustic emission sensor and amplifier

4.5.2.3 Slider Dynamics during Touch Down

A touchdown measurement was performed on the setup and the vibration modes of a same batch slider used in the experiments were measured. Slider touchdown was performed by applying current to heater element with increasing heater power. To obtain in-situ FH, a wide track of 1 μm is written using wide head on perpendicular recording media with 1111 0000 pattern at 80 MHz writing frequency. Both first and third order harmonics are used in the measurement. Heater power is supplied preamplifier and at the same time MP, AE and LDV signals are also monitored. By monitoring the root mean square signals of AE and LDV, touch down occurs when 100 mW heater power is applied.

In frequency domain, frequency peaks of interest can be observed in the range of 0 to 300 kHz as shown in Figure 4-53. Based on a typical slider's mechanical design, this frequency range represents a slider's mechanical resonance of the air bearing (pitch and roll modes) [23][25][57] and the suspension or mechanical fixture. The characteristics of a slider's resonance frequency of the suspension have been studied by Fu and Bogy [72], Takahashi *et al* [58], Zeng and Bogy [59] via experiments and simulation by Li and Horowitz [73]. There are generally three primary air-bearing vibration modes, which are the trailing-edge pitch mode, leading edge pitch mode, and roll mode [57]. As shown in Figure 4-53, the

observed lower frequencies at 40 and 70 kHz represent the vibration of head suspension [58] [59] or slider's roll mode [57], and the higher frequencies of 120 kHz and 250 kHz match the frequency of slider's leading-edge and trailing-edge pitch mode, respectively [57]. Different slider design has different dynamic characteristics and capability of observation of these frequencies in different measurement modes could provide more comprehensive insight to further study of slider dynamics under ultra-low flying HDI phenomenon, such as slider-lube interactions [60] [61]. The developed tester is aimed to achieve this capability.

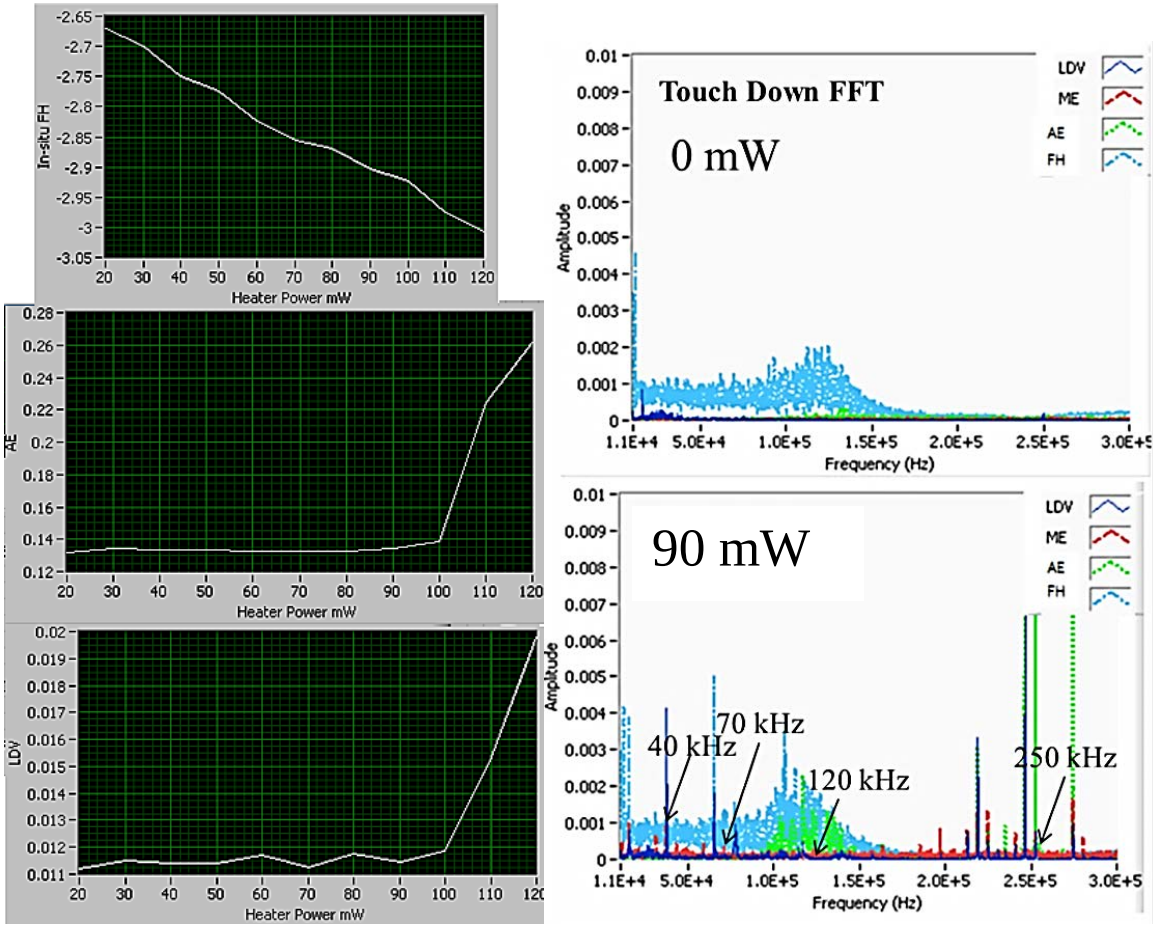

Figure 4-53: Simultaneous measurement of touch down process. Left: signal RMS, right: FFT

Another test measurement is carried out, where increasing heater power is implemented using programmable ramping voltage source as shown in Figure 4-54. The

heater coil resistance ranges from 50 Ω to 70 Ω and voltage power relationship can be obtained as shown in Figure 4-55.

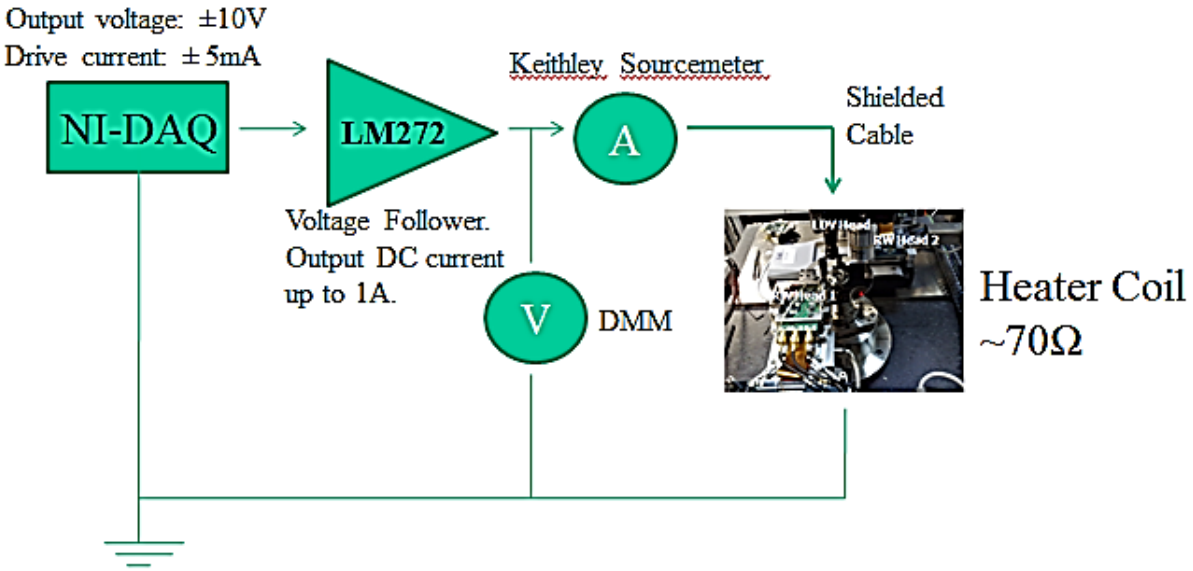

Figure 4-54: Touch down process measurement setup

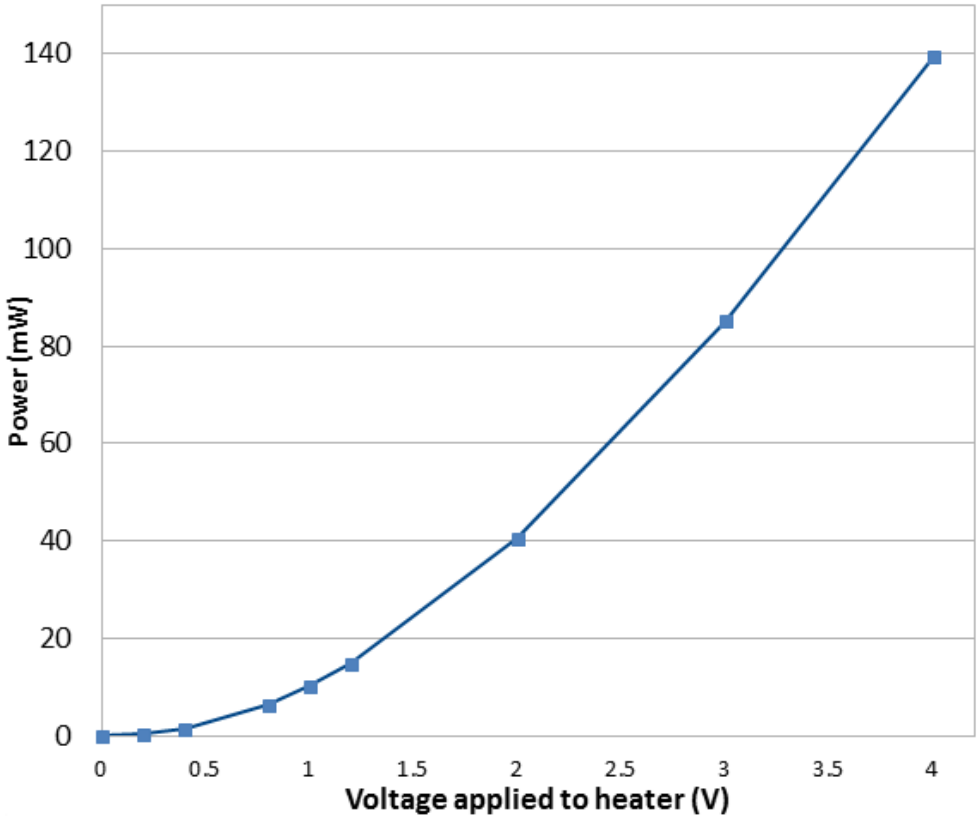

Figure 4-55: Voltage vs heater power plot

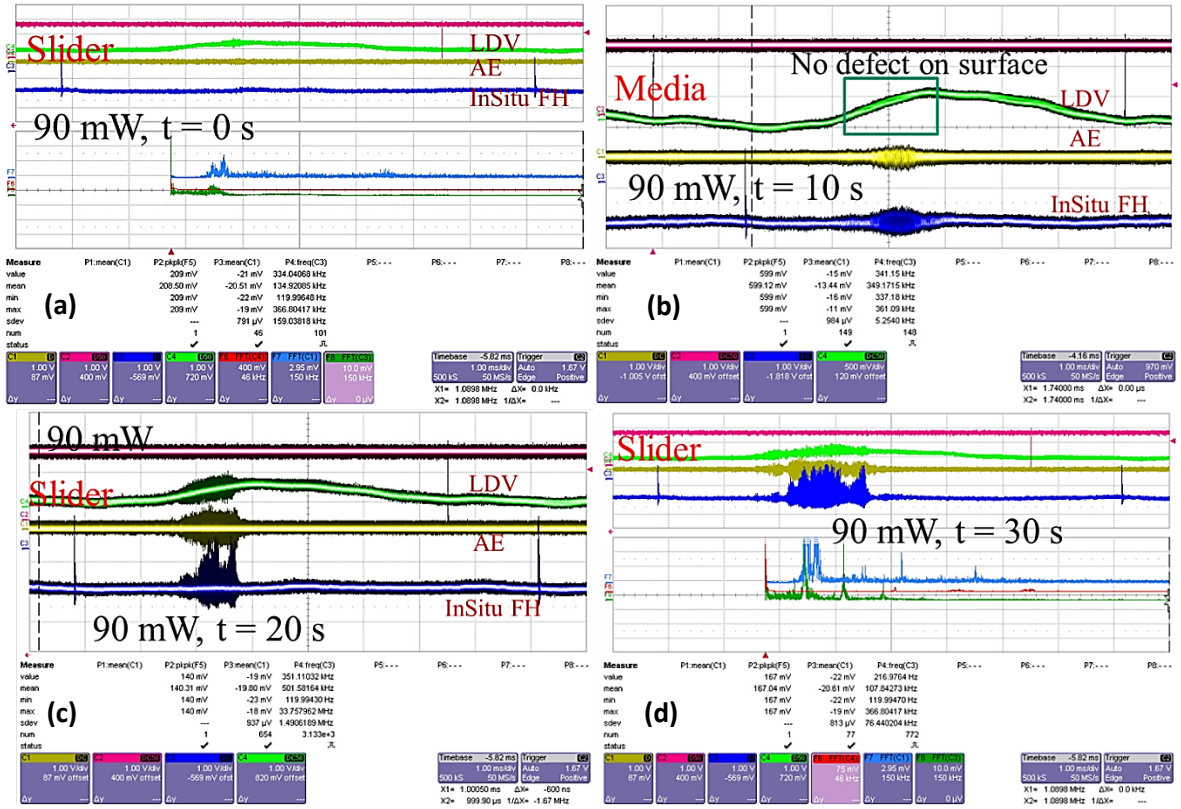

Figure 4-56(a)-(d): Concurrent measurements at 90 mW

Touch down indication can be easily determined from the RMS of both AE and LDV as shown in Figure 4-53, but measurement signals observed in time domain can provide more detail of the touch down process. As shown in Figures 4-56(b)-(d), LDV, AE and, in-situ FH show continuous slider vibration only at a particular location of media at 90 mW. Together with information of LDV signal, slider contact occurs when the slider reaches its highest acceleration in response to the varying media run-out topography (represented by steepest slope of the LDV velocity signal). Different slider would yield different sensitivity and further analysis can be carried out to understand slider's response to such topography in terms of air bearing surface design.

At t = 0, little or no slider vibration can be seen. After 10 seconds, AE and in-situ FH signals start to show slider vibration which is not caused by defect on media as shown by the LDV signal in Figure 4-56(b). When LDV beam spot is positioned back on slider's trailing

edge, vibration is seen to persist at t = 20 s. Subsequently, vibration amplitude becomes more intense with slider vibrating at longer time after 30 seconds. Here, the frequency domain information shows dominant frequencies with the same characteristics of slider as shown in Figure 4-53.

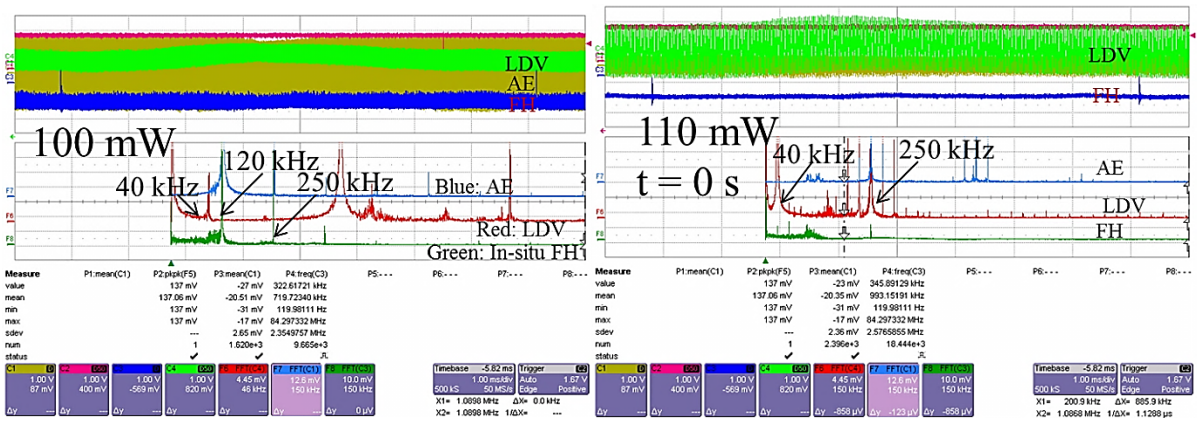

Figure 4-57(a): Concurrent measurements at 100 mW.
Figure 4-57(b): Concurrent measurements at 110 mW, t = 0 s.

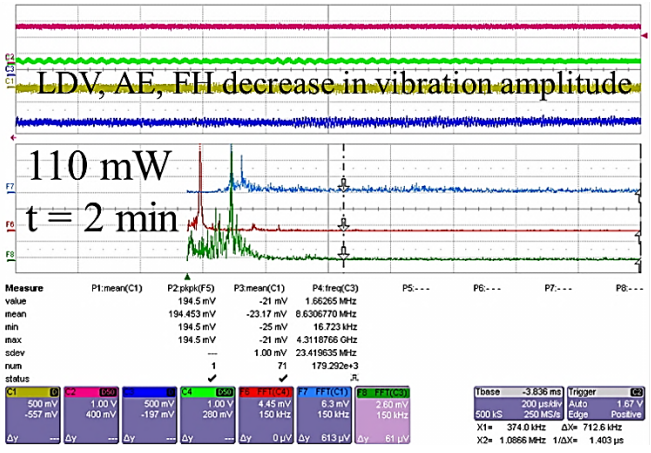

Figure 4-58: Concurrent measurements at 110 mW at t = 2 min.

At 100 mW (as shown in Figure 4-57(a)), the slider continues to vibrate with excitation frequency modes of 40, 120, and 250 kHz. At this time, it has entered the phase of continuous bouncing vibration [62] with increased vibration amplitudes detected in all measurement channels. Upon increasing protrusion further by applying 110 mW heater power (as shown in Figure 4-57(b)), the 250 kHz vibration mode remains strong while the

120 kHz vibration mode diminishes. After 2 minutes (as shown in Figure 4-57), the slider vibration mode is dominated only by 120 kHz with drastic reduction in vibration amplitude. This observation of the slider dynamics is of particular interest because it may indicate various stages of slider's interaction with the lubricant, eventually leading to lube-surfing condition where only a part of the TFC protrusion is in contact with the lubricant. This dampens slider's vibration [63]. Lube surfing condition is one of possible solutions for contacting head disk interface towards 10 Tb/in^2 areal density [48]. Possibility of this condition under prolonged flying may eventually wear off lubricant and carbon overcoat, causing head disk crash.

4.6 Summary

The developed spinstand provides concurrent multifunctional and concurrent testing capabilities. As such, multifold information can be obtained that can help to provide better understanding of HDI phenomenon. The tester was used for measurement of defects on disk media based on the concurrent mapping approach consisting of AE, LDV, in-situ FH, and MP, and multifold information can be obtained that can help to remove spurious information present in any single scan. Among the various methods, LDV's capability to detect media defects has been discussed in detail. It can be shown that through special enhanced method, LDV can be used concurrently with missing pulse to perform media defect certification that is fast and more efficient.

In addition, application of concurrent methods has been applied to measure and study slider dynamics. The first involves the observation of slider dynamics when a slider interacts with a media defect. It has been shown that mapping approach provides two-dimensional information on the size of the interaction regime, and nature of interactions. Such a mapping approach is suggested for useful characterization of sliders, in particular, thermal activated

protrusions from TFC technology. Secondly, particular interest is shown to study slider dynamics of ultra-low flying height using thermal protrusion. Here, contact induced vibrations are analyzed in both frequency and time domain analysis to better understand the touch down process. It is observed that slider dynamics is a slider design specific characteristics and frequency domain analysis is shown useful to characterize slider's mechanical response. Time domain information helps to reveal slider's interaction with media surface. Concurrent methods can also help to provide better understanding of slider lube interactions using different sensitivity of different measurement methods.

CHAPTER 5: Tribocharge Evaluation during Slider Disk Contact

Continual increase in recording density towards Tb/in^2 requires extremely low slider flying height (FH) of 2-3 nm. Further increase in recording density of magnetic disk drives requires further reduction of head-media spacing. Researchers are thus exploring new head disk interface schemes such as fly and lubricant-contact recording mechanisms, aimed at pushing mechanical spacing between head-slider and disk media to the possible minimum. In the fly and lubricant-contact recording scheme, the majority of the slider's air bearing surface remains flying while only a tiny read/write area contacts the lubricant on the disk surface. As the mechanical spacing between the slider and disk decreases, a potential difference can exist between them (due to contact potential) which can cause electrostatic forces to be generated. The electrostatic force is seen as one of the causes of interface instability.

An important effect associated with intermittent head-disk contact is the tribocharging phenomenon. The generated tribocharges can induce lubricant degradation and accelerate contamination induced head disk interface failure. In this way, interface stability and reliability are affected. Tribocharge emission at slider-disk interface also degrades MR sensor's reliability. This is of concern as head disk spacing continues to decrease to facilitate higher recording densities. Nakayama *et al* [66], indicated that the degree to which tribo-charging is detectable depends on the difference between the rate of charge accumulation and the rate of discharge. Feng *et al* [42] reported that tribocharging intensity is related to the degree of slider-disk interaction.

This chapter focuses on the investigation of tribocharging phenomenon and the electrical characterization of the head-disk interface. It is proposed that the amount of tribocharge generated is dependent on contact velocity and contact area. The generated

charges can penetrate through the DLC layer, and are discharged through the electrometer as tribovoltage or tribocurrent. The level of tribocurrent intensity depends on the potential difference between head and disk as well as the charge density of the DLC.

In the experiment, three regimes of slider-disk interaction are studied - slider flying over disk surface during disk deceleration, slider dragging on disk surface at constant velocity, and slider takeoff and flying during deceleration. Comparisons are made based on the same slider flying with different disk initial linear velocities. Differences in tribocharge current peak values and their occurrences are discussed. Finally, calculations were also conducted to verify the observations.

5.1 Tester Tribocharge Setup

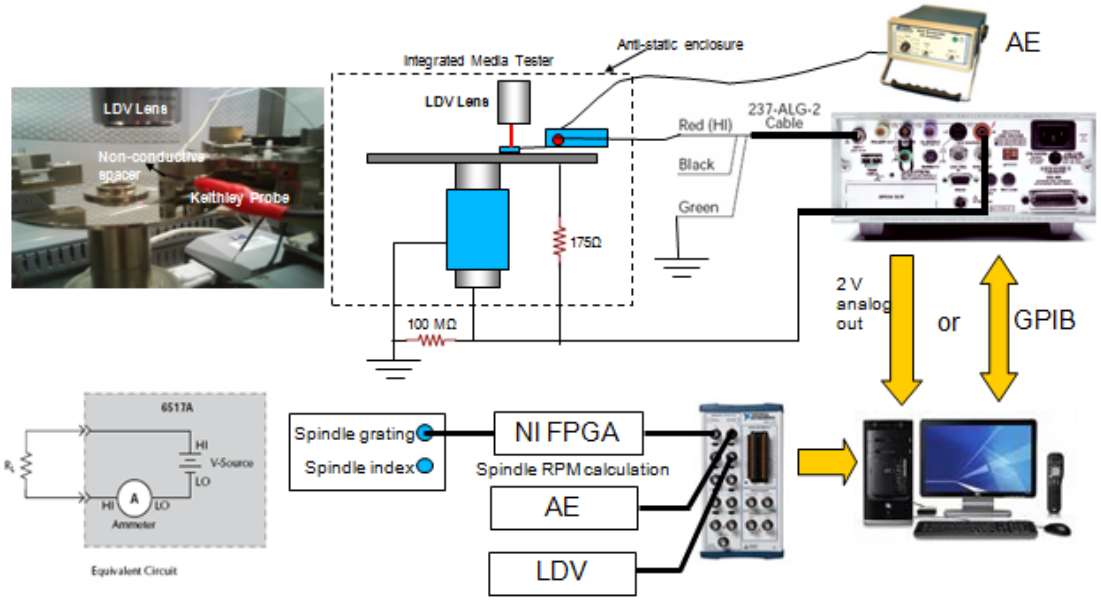

Figure 5-1: Tribocharge measurement setup on the integrated media tester

As shown in Figure 5-1, the measurement of tribocurrent across the head-disk interface involves isolating the electrical path across head disk interface with minimal current leakage. Measurement is performed by modifying the electrical connection of the integrated media tester by adding a wire extension to the body of the spindle base and modifying the

cartridge to isolate the slider from the system's ground. The electrical equivalent schematic of the measurement system is shown in Figure 5-2. Since the current level is small (in the order of nA and below), stray electrical resistive path will induce large current leakage and noise. Therefore, there can be three possible charge flow paths in our measurement: charge leakage through electrometer path, charge leakage at the interface, and discharge through electrometer.

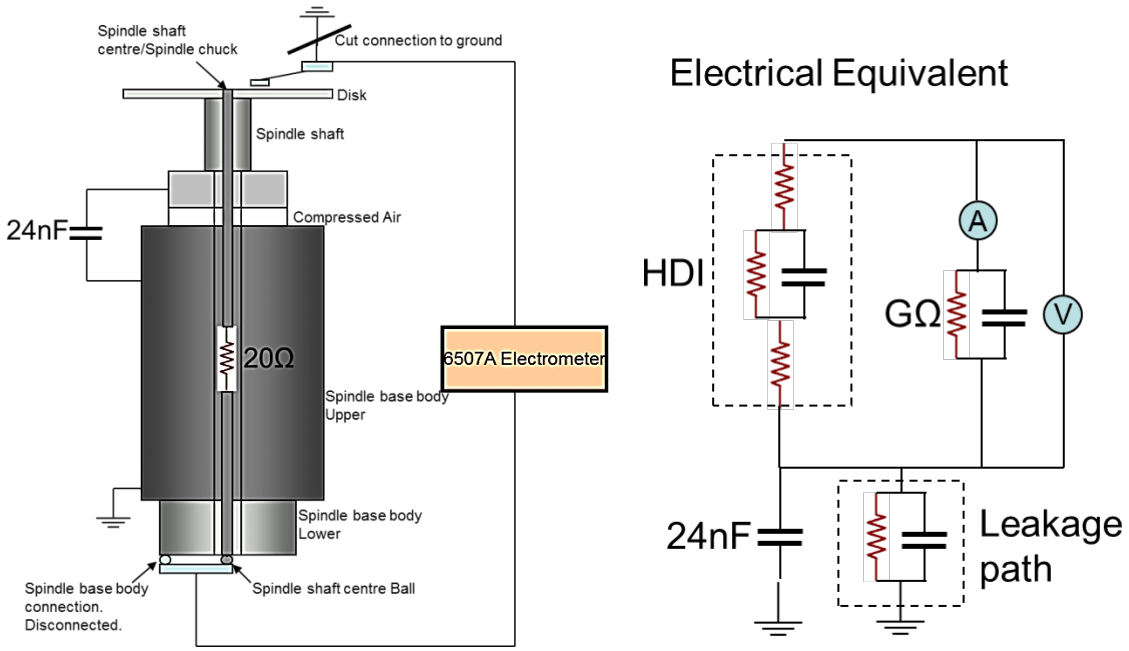

Figure 5-2: Schematic of electrical connections of the multifunctional spinstand

Figure 5-3: Testing platform and shielding cage

Kiely and Hsia [67] recommend using a Faraday cage around the spinstand to shield external interferences. The Faraday cage on the integrated media tester is shown in Figure 5-3. Apart from the electrical isolation for tribocharge measurement, the setup is also modified to include the connection to the voltage source. This enables the application of fixed potential or DC voltage across the head disk interface and current can be measured simultaneously. Figure 5-4 shows the schematic of 6517A electrometer manufactured by Keithley Instrument.

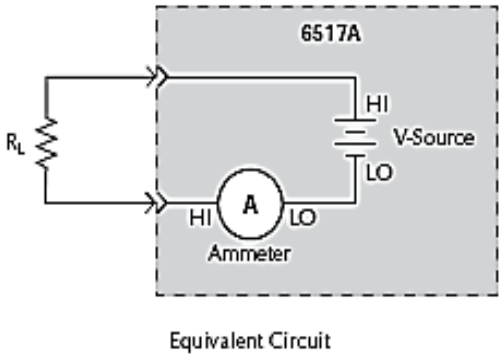

Figure 5-4: Schematic of voltage source of electrometer 6517A

Generally, an electrometer is a current/voltage measurement device which has very high input impedance, in the order of TΩ, and has enough sensitivity to measure very small current (in the order of pA). This model of electrometer also features a built-in DC voltage source to aid measurements. As shown in Figure 5-4, measurement can be configured by connecting device under test between the HI port of the voltage source and the HI port of the ammeter. In this configuration, both LO ports of the internal ammeter and voltage source need to be connected. This can be easily done via the device's setting. If only tribocurrent measurement is required, device under test can be directly connected to the ammeter HI and LO ports.

5.1.1 Low Current Measurement: Electrical Shielding and Guarding

It is important to be able to reduce leakage current so that we are able to obtain an accurate current measurement using an ammeter. The source resistance of the head-disk interface in the presence of combined layer of lubricant, DLC from media, SiO_x, and DLC from head is at GΩ level. At this magnitude of resistance, voltage measurement requires minimal circuit loading. The electrometer has extremely high input impedance, typically at the TΩ level. Furthermore, the input offset current is less than 3 fA. In this way, the electrometer has minimal effect on the circuit being measured. When measuring a small current at the order of nA and below, the electrometer's ammeter has to have low input offset current and very low voltage burden. Voltage burden is the input voltage drop of an ammeter.

Measurements are implemented on both the Guzik spinstand and the integrated media tester. We measured 24 nF capacitance with very high resistance (more than 40 MΩ) from the spindle base to ground on the integrated media analyzer. This capacitance does not exist on the Guzik system. Instead, we measured 50 kΩ resistance to ground. We have simulated

these two conditions. On the Guzik system, the measured current across head and disk ranges is in μA level and the first few applied voltage steps has a linear I-V relationship and measured resistance across the head disk Interface is approximately 2 MΩ. The material between head and disk is categorised as dielectric and the I-V characteristic should not follow a linear trend. Moreover, resistance measurement using a digital multimeter shows very large reading, greater than 40 MΩ. This means that the measured current should be very small. In our result, the measured current is less than 5 pA without applied voltage and only 50 pA with 1 V potential across the head and disk. This translates to a resistance at GΩ level.

Guarding is a low current measurement technique to minimize leakage current. If leakage current is large and is affecting the current flow path to the ammeter, the measurement will totally be inaccurate. As such, the measurement setup is modified to include proper guarding technique as shown in Figure 5-5.

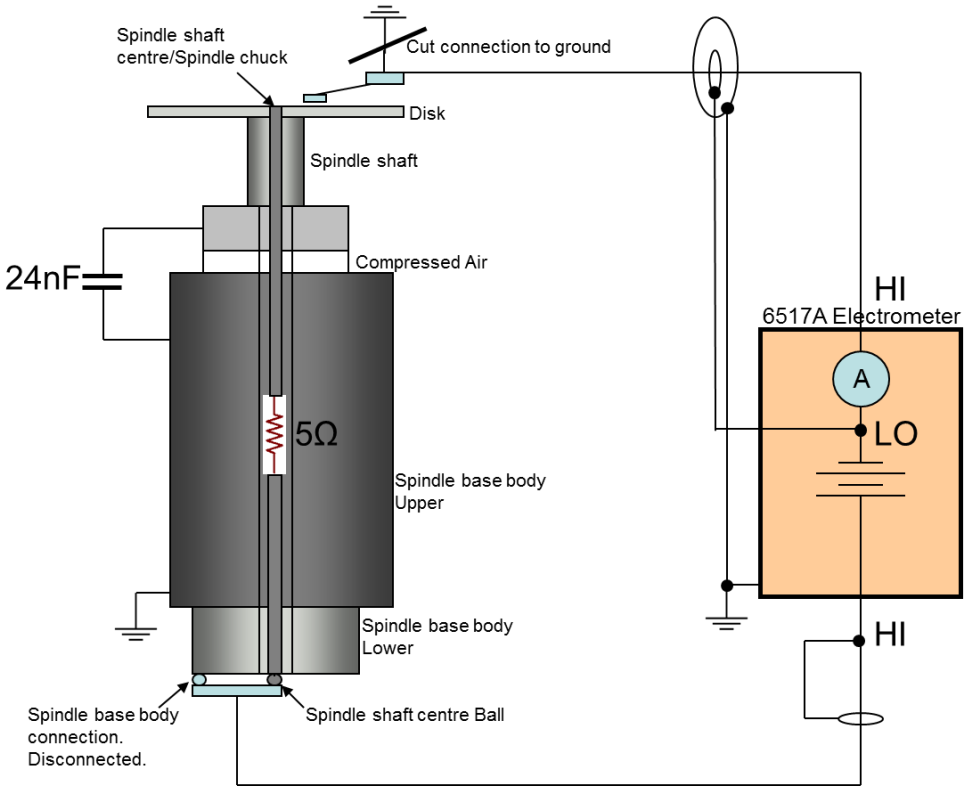

Figure 5-5: Guarding technique for tribocharge measurement

If our test subject has very high resistance, leakage current can occur across the coaxial cable's dielectric insulation to ground (assuming that the resistance across the dielectric is lower than test subject resistance). This concept is clearly shown in Figure 5-6(a) and Figure 5-6(b) .

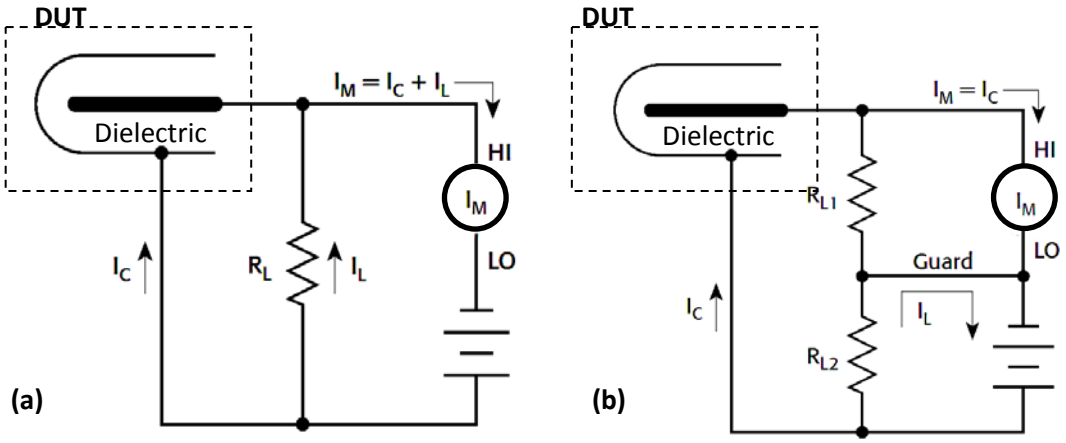

Figure 5-6(a): Circuit without guarding
Figure 5-6(b): Circuit with guarding

Without guard, the measured current by the ammeter includes both leakage current across coaxial cable, I_L and the current through the measured load I_C. By introducing a guard shield connected to the LO port of ammeter will greatly reduce the leakage current flowing to the ammeter. This is because the the voltage burden of the ammeter is in μV range and will assume minimal potential difference across cable's coaxial dielectric R_{L1} to the guard shield. The major leakage current flows via the R_{L2} path of the dielectric, bypassing the ammeter.

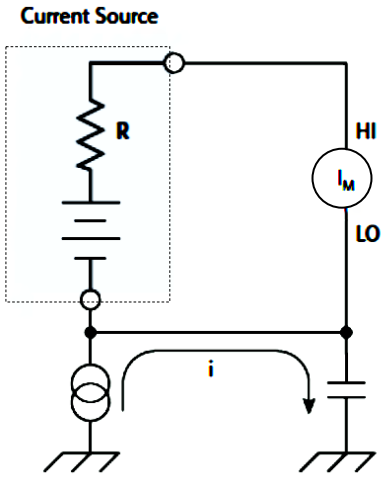

Figure 5-7: Connection point of test load to 6517A ammeter to minimize noise

As shown in Figure 5-7, the HI input port lead of the ammeter is connected to the highest resistance point of the device under test. This is to ensure that any leakage or current noise sources do not flow through the ammeter during measurement. Connecting the spindle base to the ammeter HI port will produce a large current noise measurement. This is because the connection at spindle base is not the high resistance point of the device under test (DUT) and the spindle shaft body structure is still unguarded. As shown by the plot in Figure 5-8, the measured leakage current was significantly reduced by a factor of 10.

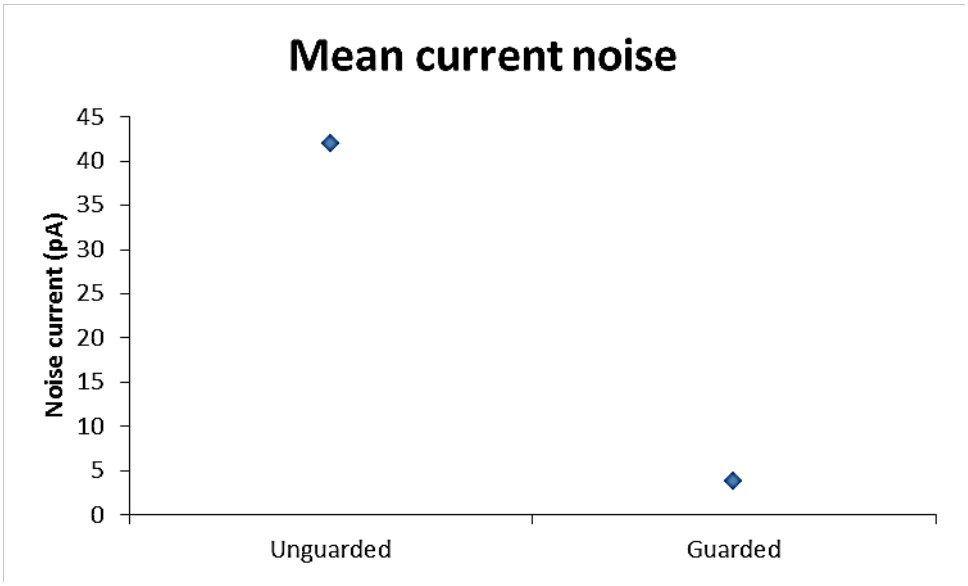

Figure 5-8: Measured mean noise current with and without guarding

Other than the possible leakage current through the dielectric, there are other sources of noise that can induce erronous measurement. Other sources of noises include triboelectric effects and mechanical stress effects as shown in Figure 5-9.

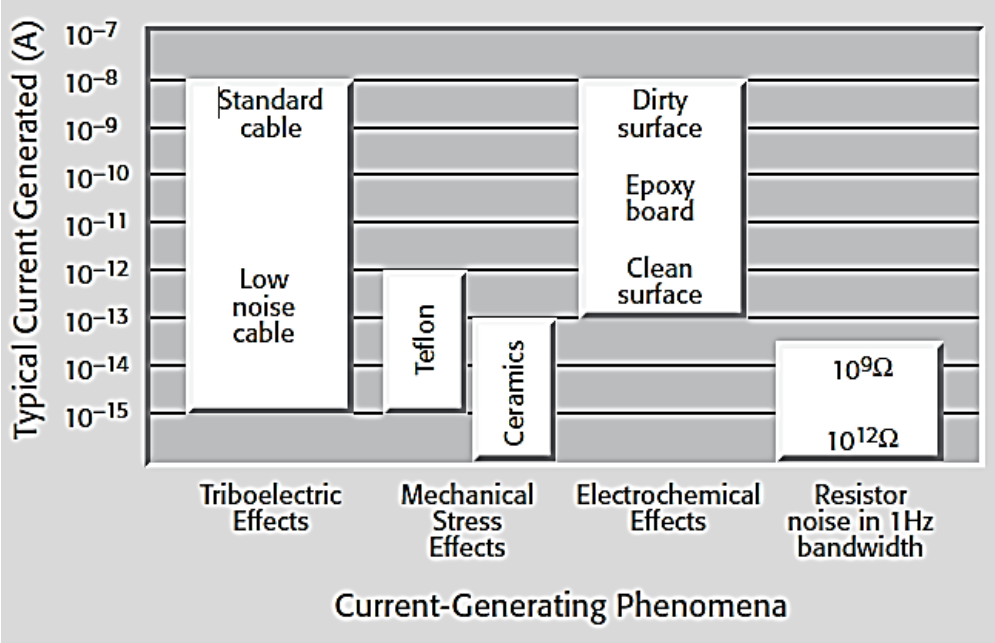

Figure 5-9: Current generating phenomena

5.1.2 Data Acquisition and Measurement

Measurement of current and voltage was performed using the Keithley electrometer 6517A. This device has very high impedance at 200 TΩ, which is desirable for very small current measurements. There are two available measurement modes: Keithley analog output or GPIB-based measurement.

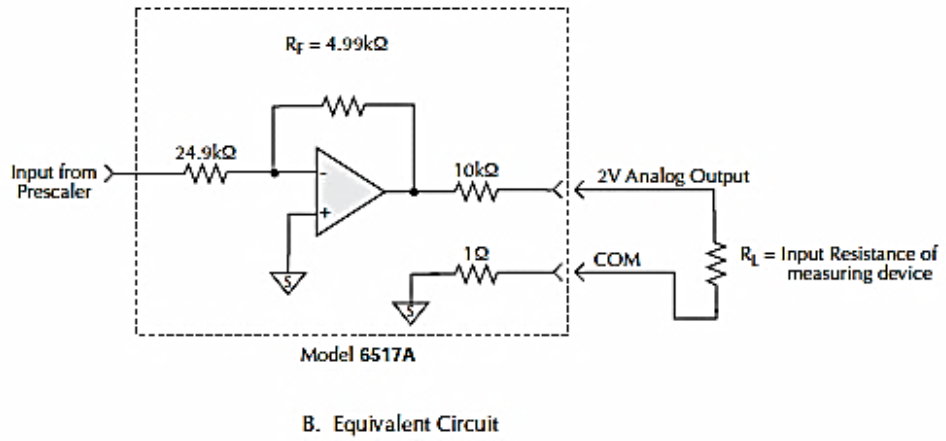

B. Equivalent Circuit

Figure 5-10: Analog output of Keithley 6517A

The connection of the electrometer analog output to the device under test is shown in Figure 5-10. Keithley analog output ranges between 0 V to 2 V for voltage measurement and -2 V to 0 V for current measurement. The electrometer output produces an output voltage which corresponds to the level of measured input. This output voltage is a proportion of the configured input range setting and has maximum magnitude of 2 V. Analog measurement has higher measurement bandwidth than GPIB-based measurement and is suitable for fast measurement. In this case, measurement can be obtained accurately and can synchronize well with other analog measurements such as those from AE and LDV.

The analog 2 V output corresponds to the full range of the measurement setting. Proper configuration of measurement range needs to be implemented to ensure that the full range setting is modified according to the measured current or voltage level. If the actual measurement starts in the middle of the full range and the measurement crosses to the next full range level, the measurement will go out-of-range and the voltage output will be saturated at rail voltage. An 'auto' mode can be set, but this will produce inaccuracy if measurement goes to another range level. Analog measurement will also be noisy if input measurement range is much smaller than the maximum range.

In this case, GPIB measurement is preferred. GPIB measurement provides an option to measure the display reading in real-time. The communication time between PC and measurement device takes at least 50 ms and consequently, the acquisition between successive measurements is slow causing fewer number of acquired samples and loss of details. In order to speed up the data acquisition, the Keithley electrometer can be configured to internally store data to buffer. In this case, the computer needs to only communicate via GPIB to start acquisition. Based on speed or Number of Power Line Cycles (NPLC) setting and buffer size, the data for the total duration of time can be retrieved. For example, at normal speed setting with NPLC= 1 and buffer size= 1000, the total acquisition time is 75s. This means that the sampling interval is 75 ms. Acquisition at the highest speed setting with NPLC = 0.01 and buffer size = 1000 takes 12.5 s which is equivalent to the sampling interval of 12.5 ms. A comparison of voltage analog output and GPIB measurement is shown in figure 5-11.

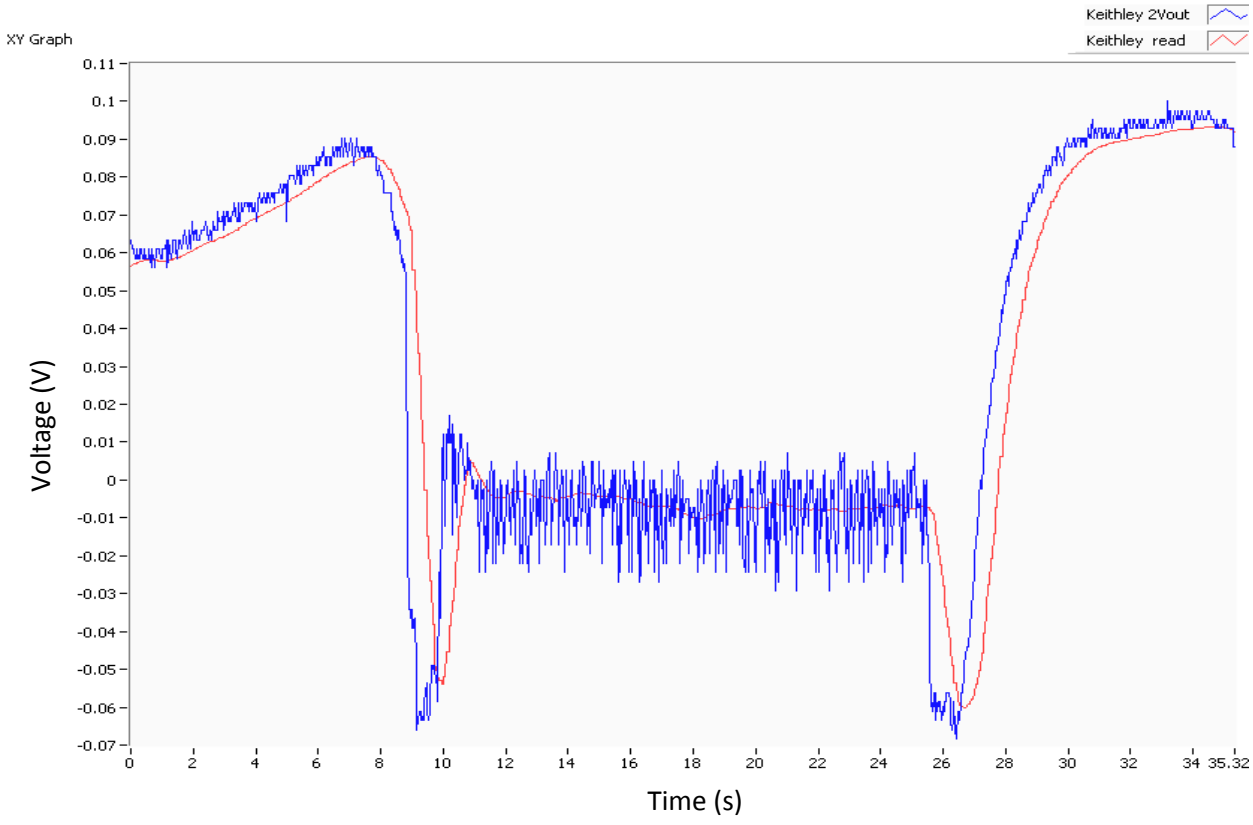

Figure 5-11: Voltage measurement mode, analog output comparison

5.2 Electrical Characteristics of the Head Disk Interface

I-V characteristic is an important electrical parameter of a material. If a material (metal) is resistive, its current will increase linearly with the applied voltage. According to the Ohm's law, if the resistance of a material to charge flow is constant, higher electric field or voltage will cause the rate of charge flow to increase. If a material is capacitive, then this material may consist of two metal electrodes separated by dielectric material. The capacitance is computed as

$$C = \frac{\varepsilon A}{d} , \qquad (5.1)$$

where C is capacitance, A is surface area of capacitor plate, d is the separation distance between capacitor plates, and ε is the dielectric constant. Relative permittivity of air is 1, so a layer of dielectric between the metal plates increases the capacitance. Capacitance is also defined as the ability to store charge per unit voltage. This means that higher dielectric constant will increase the surface charge density accumulated on the capacitor plates. When two materials rub, electric charges are generated on the two material surfaces due to polarization. This creates localized electric field at the interface.

Characterizing electrical parameters of an interface, particularly when a slider is flying, is complex. Current flow at the head disk interface is caused by induced electrostatic potential between slider and disk at ultra-low flying height. Firstly, intermittent slider disk contact causes charge generation and change in slider disk potential. Secondly, decrease in flying height affect capacitance or resistance of head disk interface which can cause change in potential between the slider and disk. Thirdly, changes in measured current during flying maybe small with only intermittent contact. This is limited by the speed of measurement

system and voltage or current offset. Electrostatic can cause lube degradation and non-uniform distribution of lubricant which can affect slider flying capabilities [68]. There is possibility that air molecule breaks down or ionizes in the presence of electrostatic potential. Also, the flying height is in the order of a few nm and there is chance that charges can overcome potential barrier through tunneling. Field emission can be caused by polarized lubricant on media surface [69]. Due to these dynamic uncertainties, it is difficult to characterize the electrical parameter of head disk interface when the slider is flying.

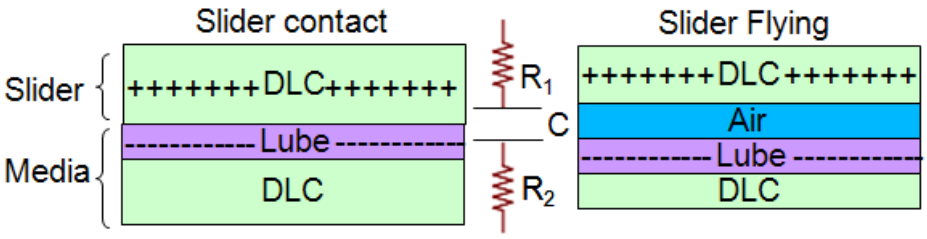

Figure 5-12: Electrical equivalent of head disk interface

We can model a head disk interface structure as metal-dielectric-metal. Dielectric composition of the interface consists of SiO_2/DLC (head) and Lube/DLC (media) as illustrated in Figure 5-12. When a slider is flying, the air layer also acts as an additional dielectric to the system. With this consideration, it is useful to start with a static I-V measurement to characterize the head disk interface. I-V measurements are obtained by applying voltage across head and disk in incremental steps. The current flow is then measured through the electrometer. From the I-V measurement, charging and discharging behavior of the system can be characterized.

Figure 5-13 shows the linear relationship between voltage and current. This is a typical resistive I-V plot according to the Ohm's law. Figure 5-14 shows the I-V plot of an ideal capacitor. Incremental voltage at two seconds interval is applied to the capacitor. The

result in Figure 5-14 shows that current is generally zero with current peak and decay occurrence during charging.

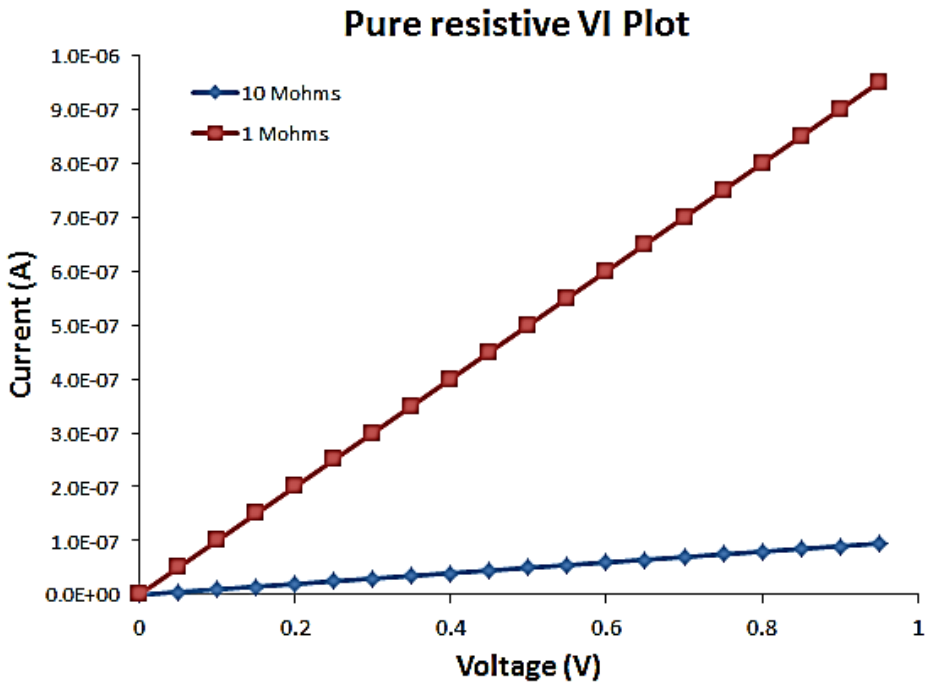

Figure 5-13: Pure resistive I-V plot

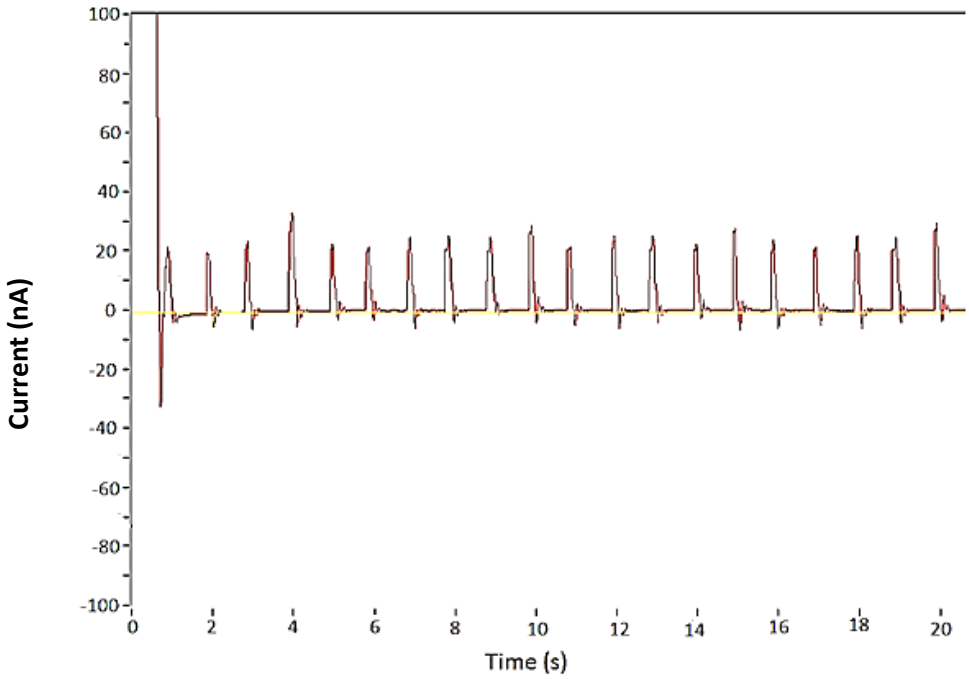

Figure 5-14: Current measurement of an ideal capacitor

The same measurement is performed to characterize the head disk interface. The sample is a 3.5” commercial media with 1.7526 mm thickness. As shown in Figure 5-14, current spikes at regular intervals are observed, showing similar behavior as an ideal capacitor. The spike is followed by a nonlinear decrease in current which implies a discharging process. The I-V plot shows a nonlinear characteristic which is typical of a dielectric or an insulator. From here, the discharging time constant of the interface can be easily estimated. The accuracy of the estimation is limited by the resolution of measurement sampling capability of the Keithley electrometer which is 12.5 ms or 80 Hz. The current spike occurrences in Figure 5-14 indicate discharging process. Therefore, a curve fit according to the model (5.2) can be applied to the measurement data to determine the time constant of the discharging process using

$$I = \frac{V_0}{R}\exp\left(-\frac{\tau}{RC}\right), \qquad (5.2)$$

where I is current, V_0 is the applied voltage, R is the resistance, C is the capacitance, and τ is the discharging time constant. The model fits the experimental data very well and the fitting result is shown in Figure 5-15. Here, time constant is calculated to be 0.06209. This value can be used to estimate head-disk interface’s electrical characteristics such as the capacitance.

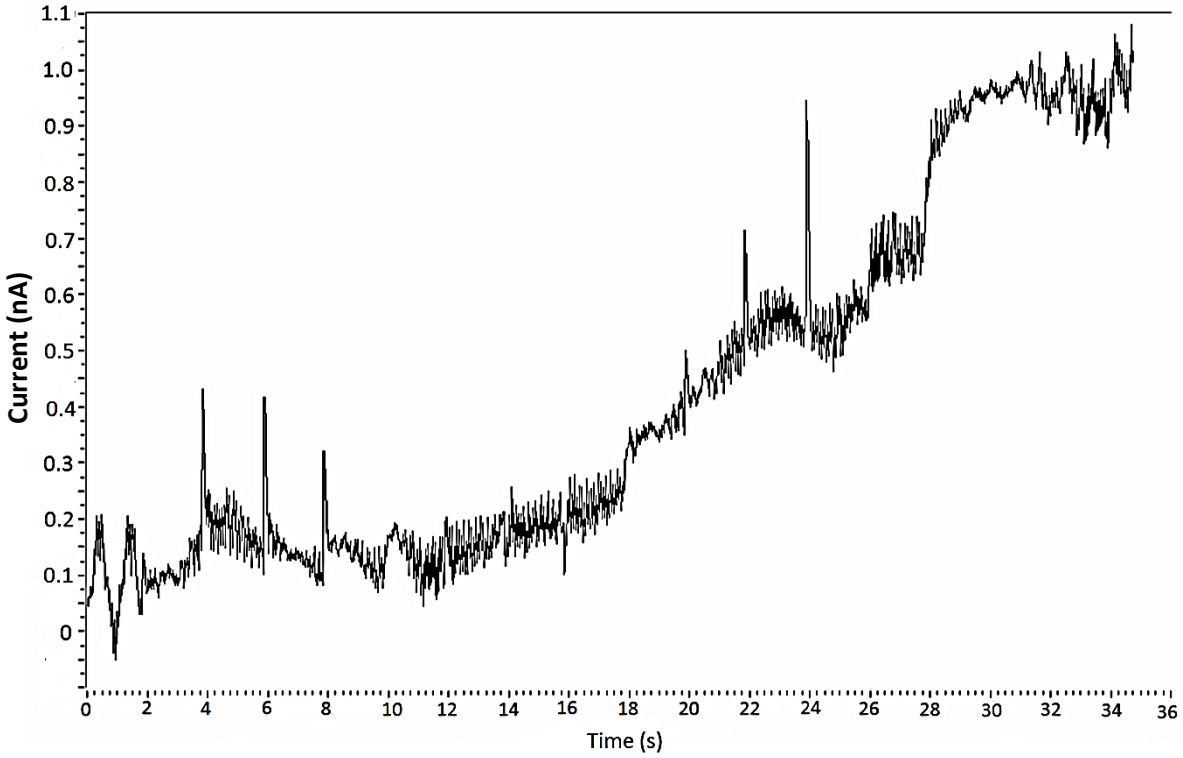

Figure 5-15: Current measurement at the slider disk interface of a 3.5" commercial media sample

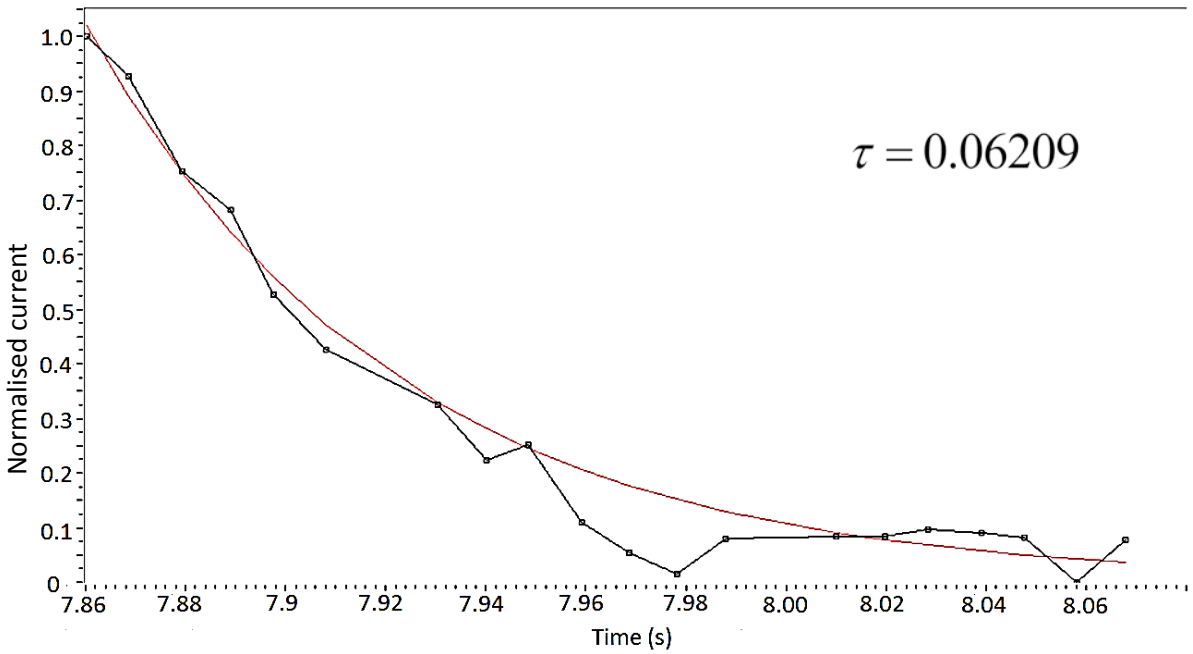

Figure 5-16: Curve fitting of current spikes using (5.2) model

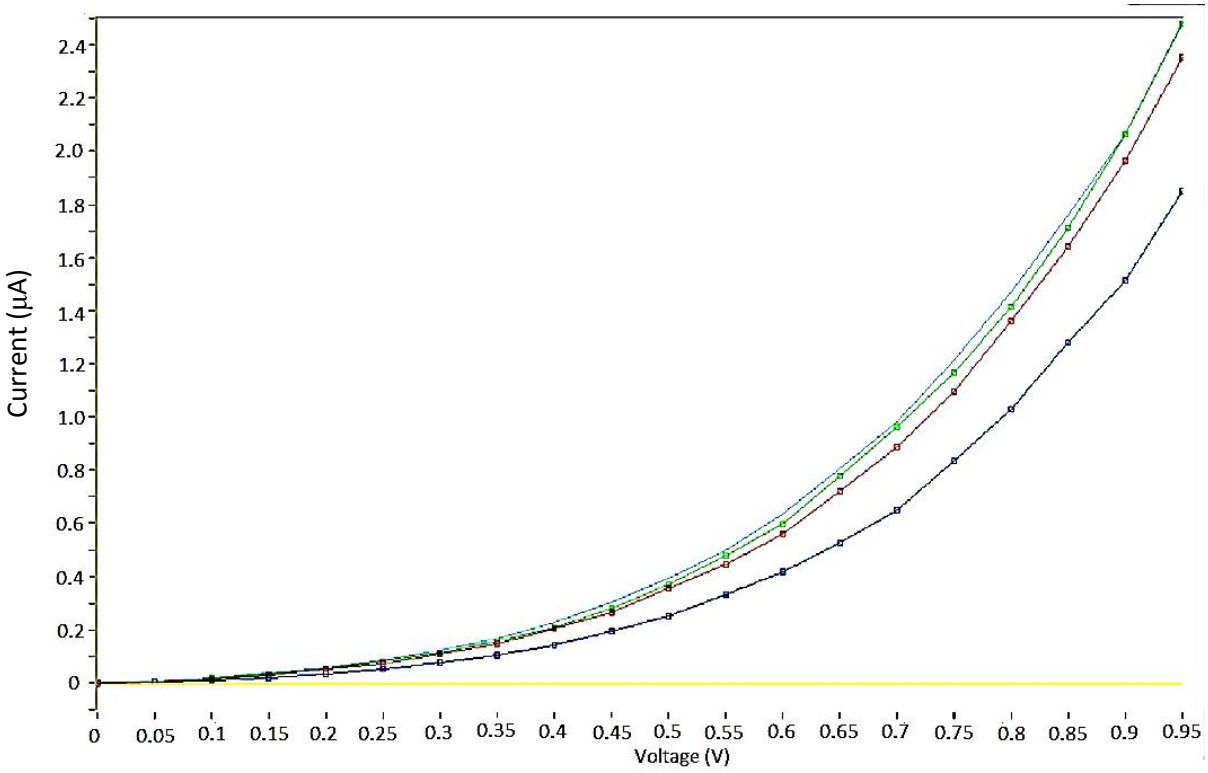

Figure 5-17: Voltage current relationship of head disk interface

The behavior of I-V characteristics is consistent and is shown in Figure 5-17. Curve-fitting is performed to further understand the model of I-V relationship of an interface. The characteristic of measured I-V curve is similar to that of Metal/DLC/Si/Metal structure [64]. In this case, a simplified equation (5.3) can be used for approximate description of conducting properties of the structure:

$$I = I_{d0} \exp\left(\frac{eV}{\eta kT}\right), \qquad (5.3)$$

where I_{d0} is the current corresponding to near zero voltage, e is the electron charge, V is voltage, η is the ideality factor, k is the Boltzmann constant, and T is temperature. A quadratic relationship $J\alpha V^2$ has been studied to be the conduction characteristics due to space-charge distribution in insulators. In order to determine more accurate electrical characteristics, I-V measurements are obtained on different two different media samples:

media A and media B. Here, 3 types of curve fitting are applied and correlated. The results are summarized in Figure 5-18.

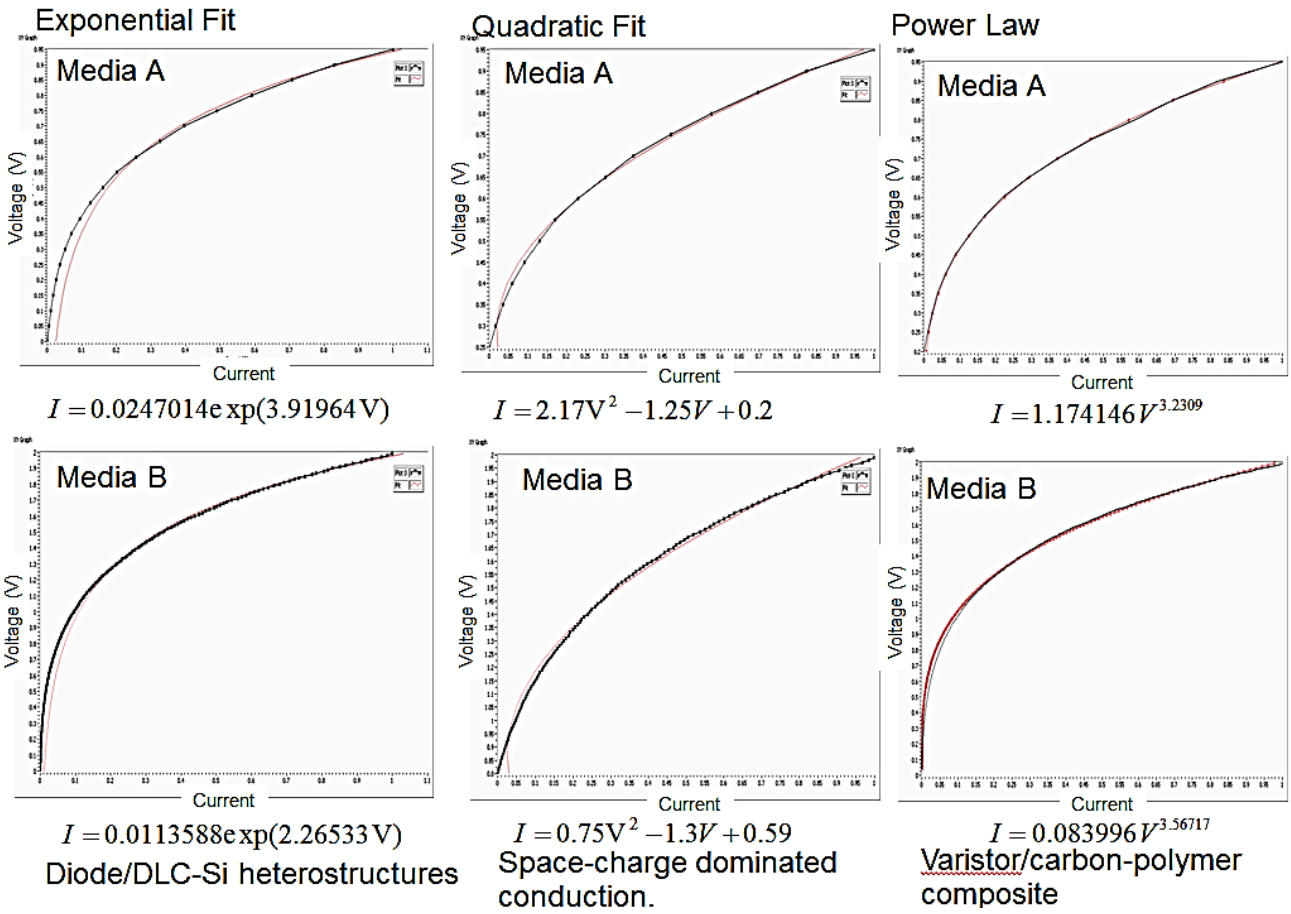

Figure 5-18: I-V fitting using exponential, quadratic and power law

Based on the results in Figure 5-18, power law has the best correlation with the measurement data. The power law relationship has been observed by Sodolski *et al* [65] as I-V behavior at room temperature of a carbon-polymer random composite system. He suggested that the I-V curves generally follow a power law expression $I = AV^n$ where A is constant and exponent n ranges from 1-1.85 [66]. The power law relationship has also been observed in Zinc Oxide Varistor where experimentally, V-I characteristics can be empirically related by simple equation $I = \left(\frac{V}{C}\right)^n$ in experiments. In this case, infinity *n* is ideal for a

varistor [67]. Typical values of *n* ranges from 30 to 100. Explanation for such non-ohmic behavior can be due to 'hopping conduction' in which electrons move by quantum mechanical tunneling between pockets, if the conductive material isolated in an insulator.

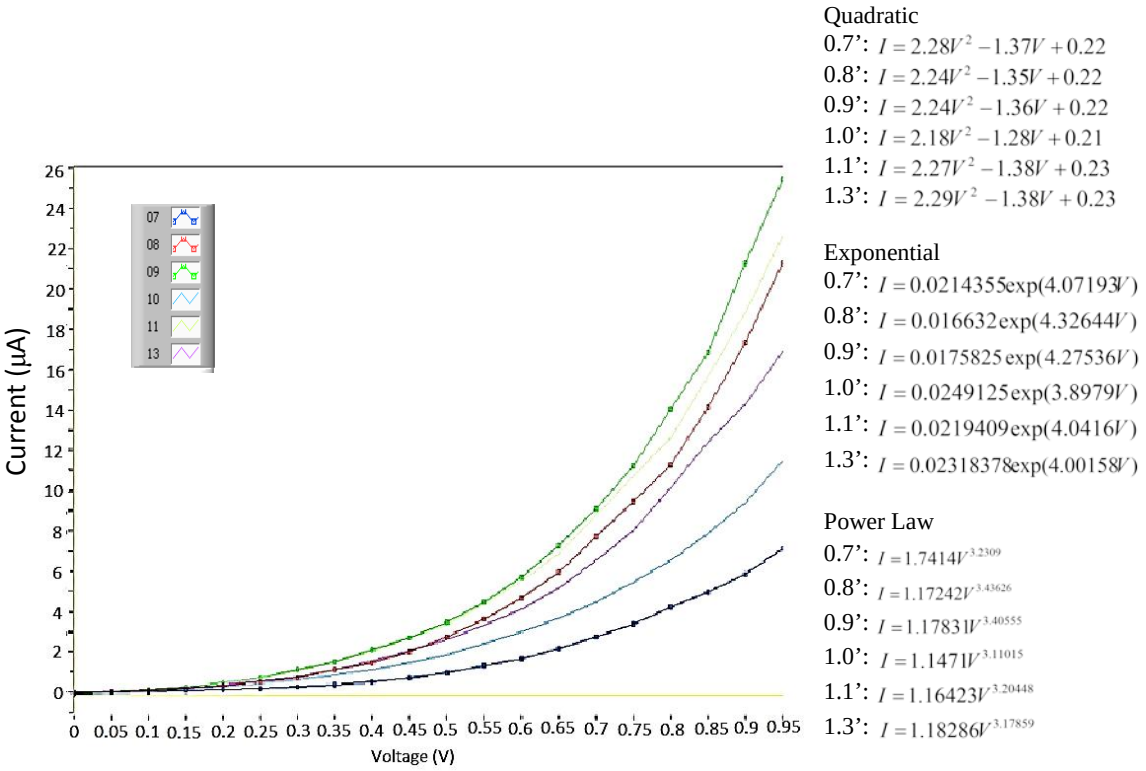

Figure 5-19: I-V measurement across different disk radius

Measurements are performed across different disk radii and fitting parameters are obtained as shown in Figure 5-19. Note that the measurement values change across different radii, there is no obvious trend of magnitude change with respect to radius change. Since fitting is obtained from normalised current, it can be seen that the dynamic behaviour (time constant, curvature), *etc* is relatively similar for all. The different magnitude indicates different slider attitude on disk surface. Probably different meniscus, different contact area, different contact force, *etc*. As the electric field increases, current increases exponentially, or power law relationship. To characterize the I-V of a sample, we need to also consider the model with influence of contact area, different thickness of lube/carbon.

5.3 Tribocharging and Discharging Concept

Slider and disk interfaces can be electrically modeled as illustrated in Figure 5-12 with non-conductive DLC on slider surface and DLC, lube on media surface. Interface region or region of charge separation can be modeled by a capacitor. Dominant charging mechanism is through frictional electrification. Charge transfer occurs in excess charge on one material and loss of charge in another. This creates a potential difference between two materials.

As charge accumulates, the voltage across a capacitor increases. At the same time, current also decays exponentially to zero. During capacitor discharging, both current and voltage decay. A higher capacitance means higher charge storing capability. The capacitance of capacitor is a function of surface area, surface area separation, and dielectric permittivity as given in (5-1) . Depending on the slider contact area and separation between slider and disk, the capacitance will change. Current is defined as net charge generation rate which is equivalent to the difference between the rate of charge generation and the rate of discharge. If current value increases, charge generation rate increases and this means that charging is dominant than discharging over same period of time.

5.4 Tribocharging Experiment

The experiments were conducted on the developed multifunctional spinstand with an attached Keithley 6517A electrometer. Figure 5-2 shows the schematic of the experimental setup for tribocharge current measurement. A shielding cover was placed over the tester to reduce noise interference from the surroundings. Both the slider body and the disk were also isolated from the ground to prevent current leakage. A commercial 3.5” perpendicular media and read/write heads were used in the experimental investigations. A test is conducted at the middle diameter zone of the disk surface. The spindle speed was varied according to the

desired linear velocities. As shown in Figure 5-20, three different disk velocities v_i of 6.4, 15.3, and 26.7 m/s were selected for investigations. The disk constant speed is 0.06 m/s. At this speed, the slider is assumed to be dragging on the disk surface.

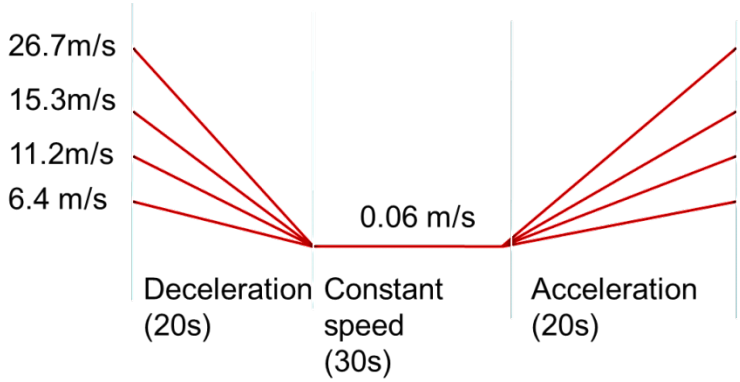

Figure 5-20: Three measurement regimes, deceleration, constant speed and acceleration

The electrical capacity of the materials at the slider-disk interface and the relative speed of the slider are the factors affecting tribocharge generation level during slider-disk interaction. Figure 5-21 shows a tribocharge current curve at disk initial linear velocity of 26.7 m/s.

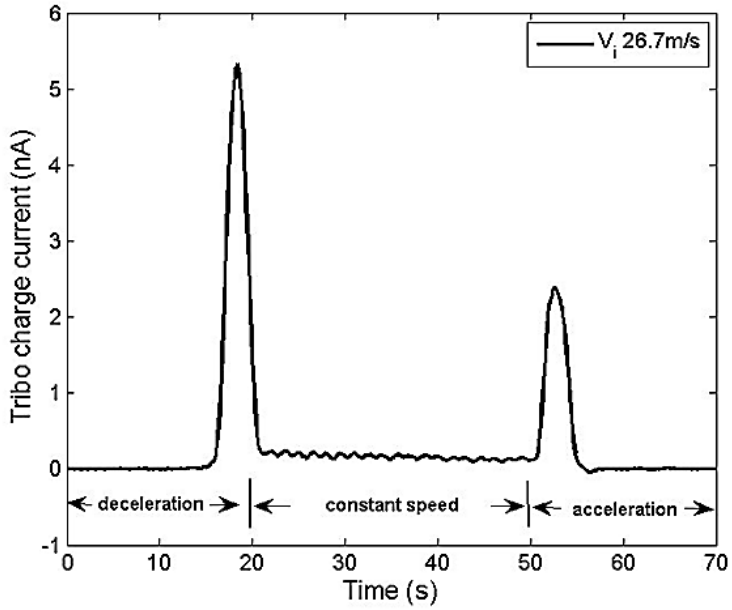

Figure 5-21: Tribocurrent curve at disk initial linear velocity of 26.7 m/s

Two saturation points of tribocharge current occurred in the test cycle. One occurred before the end of the disk deceleration regime, and another occurred after the beginning of the disk acceleration regime. The former showed a larger value of tribocurrent, while the latter was smaller in the test condition. A small tribocurrent ripple was also observed in the constant linear velocity regime between the two tribocurrent peaks shown in Figure 5-21. In this region, the slider was dragging on the disk surface at a constant linear velocity of 0.06 m/s. At such a low disk linear velocity, less extra charges are generated, and the ripple observed could be the indication that charges still remain on the contact track of the disk.

5.4.1 Disk Deceleration

The tribocurrent in the disk deceleration phase was plotted with two types of horizontal axes: tribocurrent versus time in Figure 5-22(a) and tribocurrent versus linear velocity in Figure 5-22(b). The results show that for different disk initial velocities, the tribocurrent reaches different saturation values at the end of the disk deceleration regime. The variation of tribocurrent followed nearly the same trend for the three disk initial velocities. A large change in tribocurrent level occurred around 15^{th} and 20^{th} second and larger tribocurrent appeared with larger disk initial velocity. Figure 5-22 shows that the tribocurrent saturation levels are around 5.3, 3.1, and 1.8 nA for the initial velocity of 26.7, 15.3, and 6.4 m/s, respectively. It is observed that the tribocurrent increases about three times (from 1.8 to 5.3 nA) for the disk initial velocity variation of 20 m/s (from 6.4 to 26.7 m/s).

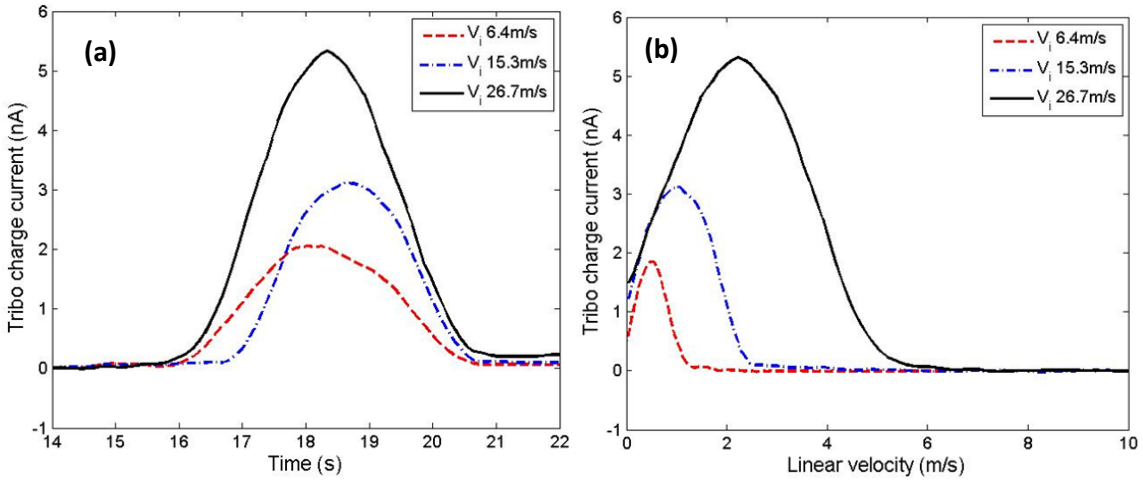

Figure 5-22 (a): Tribocurrent versus time in disk deceleration phase
Figure 5-22 (b): Tribocurrent versus disk linear velocity

Figure 5-22(b) shows tribocharge current versus disk velocity for different initial velocity v_i . It can be observed that an increase in tribocurrent starts to occur at velocities of 6, 2.4 and 1.2 m/s for the disk initial velocities of 26.7, 15.3 and 6.4 m/s. respectively. It is noted that the ratio of the disk initial velocity to the linear velocity at the onset of tribocurrent increase at the same deceleration time frame is similar for all three cases. The result implies that during disk deceleration, the spacing between the slider and disk is reduced at a faster rate; thus slider-disk interaction intensity is increased, resulting in more generation of tribocharges. From this observation, it can be concluded that tribocharge current occurs due to slider-disk interaction intensity, and the tribocurrent buildup level depends on disk initial velocity. This is consistent with the result by Park *et al* [45] stating that the charge buildup level and the tribocurrent level are independent of the slider-disk interaction time.

5.4.2 Disk Constant speed; Slider dragging on disk surface

The charges accumulated during disk acceleration remained at a constant level with less than 0.25 nA of tribocurrent in the disk constant speed regime. In this phase, the disk velocity was reduced to 0.06 m/s and the slider was dragging on the disk surface. The

tribocurrent is approximately 0.05 nA for initial velocity v_i = 6.4 m/s, 0.1 nA for v_i = 15.3 m/s and 0.2 nA for v_i = 26.7 m/s. Also, a tribocurrent ripple was observed for the large v_i = 26.7 m/s, which decayed during the disk constant speed phase. For the other two cases, an obvious gradual decay for the tribocurrent ripple was not seen.

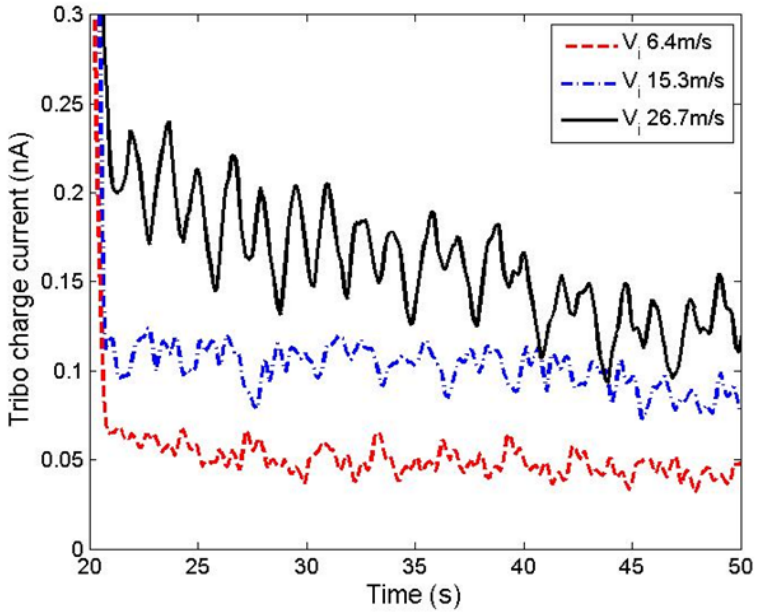

Figure 5-23: Tribocurrent at constant RPM region

The results in Figure 5-23 suggest that the increased head-disk intermittent interactions during the slider's dragging on the disk surface leads to more tribocharge accumulation at the head disk interface, and that excess generated charges are discharged via the external path as tribocurrent through the Keithley electrometer. The charge and discharge of tribocharges occurred as long as the slider was rubbing against the rotating disk. One interesting point to note is that although the velocity for the slider's dragging on the disk was the same in all cases, the final equilibrium tribocurrent levels at the end of the constant velocity phase are different. This suggests that the velocity during the intermittent contact phase was less important than the disk initial velocity and deceleration in terms of their effects on the observed tribocharge current. It is believed that the increased charge

accumulation on the surface of slider/disk for larger disk initial velocities remains on the disk and can change the tribocharging conditions during this constant velocity intermittent contact phase.

5.4.3 Disk Acceleration

With reference to curves in Figures 5-24 (a) and (b), tribocurrent increase is observed during slider take-off or disk acceleration. This is compared to the case during disk deceleration and constant velocity. Similar to the tribocurrent curves in the deceleration regime, a larger tribocurrent saturation point occurred for a larger disk initial velocity in the acceleration regime. The range of linear velocity during tribocurrent occurrence is also similar during both acceleration and deceleration for all three cases. The only observed difference is that the magnitude of the tribocurrent is smaller during disk deceleration compared to that of disk acceleration. Moreover, discrepancy is also noted for v_i = 15.3 m/s which shows slightly higher tribocurrent magnitude compared to v_i = 15.3 m/s. Further study needs to be done to explain this discrepancy. It can be implied that the saturation level of tribocharge current build up is related to disk initial linear velocity and is less affected by the velocity during the dragging intermittent contact phase.

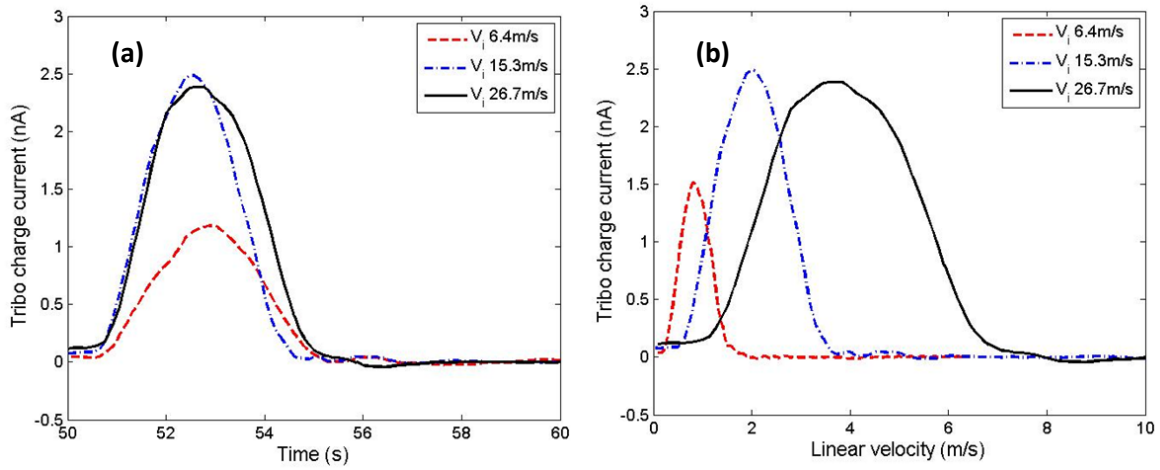

Figure 5-24 (a): Tribocurrent versus time in disk acceleration phase.
Figure 5-24 (b): Tribocurrent versus disk linear velocity

5.5 Tribocharge Generation and Current

The tribocharge generation conditions are different for take-off and touch down situations, although the magnitude of acceleration and deceleration is the same for each case of same initial velocities. Figure 5-25 plots the acceleration against the excess charges generated for both take-off and touch-down conditions. The excess charges are calculated from the tribocurrent measured by the electrometer which is given by (5.4)

$$Q = \int I dt \,, \qquad (5.4)$$

where Q is the tribocharge, I is the measured tribocurrent and t is the time of measurement.

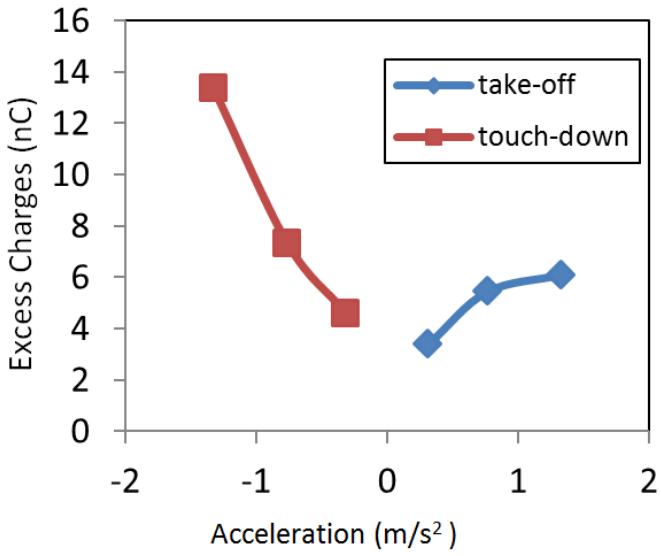

Figure 5-25: Relationship between acceleration and generation of tribocharges

Assuming that the electrical capacity is the same in all the experiments (since the head and disk were unchanged) and similar conditions hold for discharge occurring directly across the interface, any extra charges generated at the interface are assumed to be discharged through the external circuit via the electrometer. Hence, the excess charges indicate the intensity of charge generation, and are observed to be higher in the touchdown (TD) or deceleration case as compared to the take-off (TO) or acceleration case. This may indicate differences in slider/disk interaction between TO and TD conditions. The onset velocities (at which increased tribocurrent profile was observed) were also different. For the 6.4, 15.3, and 26.7 m/s initial velocities, the onset velocities for deceleration and acceleration were 1.2, 2.4, and 6.0 m/s and 1.5, 3.8, and 7.0 m/s, respectively.

In general, charge generation increases as the magnitude of acceleration increases. The increased generation of charges may be attributed to the increase of stiction with acceleration. Zhao *et al* [68], showed that the stiction coefficient increased with acceleration for laser textured disks (but reduced for mechanical textured disks). Results by Nakayama *et al* [69] showed an opposite trend where the temporal distributions of tribocurrent were

actually lower for higher accelerations. The observed differences may therefore be due to differences in lubricant and surface texture/roughness conditions in the respective experiments.

To further understand the tribocharging phenomena, a separate tribovoltage together with acoustic emission (AE) measurement was conducted to compare with the tribocurrent measurement under similar initial velocity conditions. In general, the tribovoltage and tribocurrent measurements were repeatable.

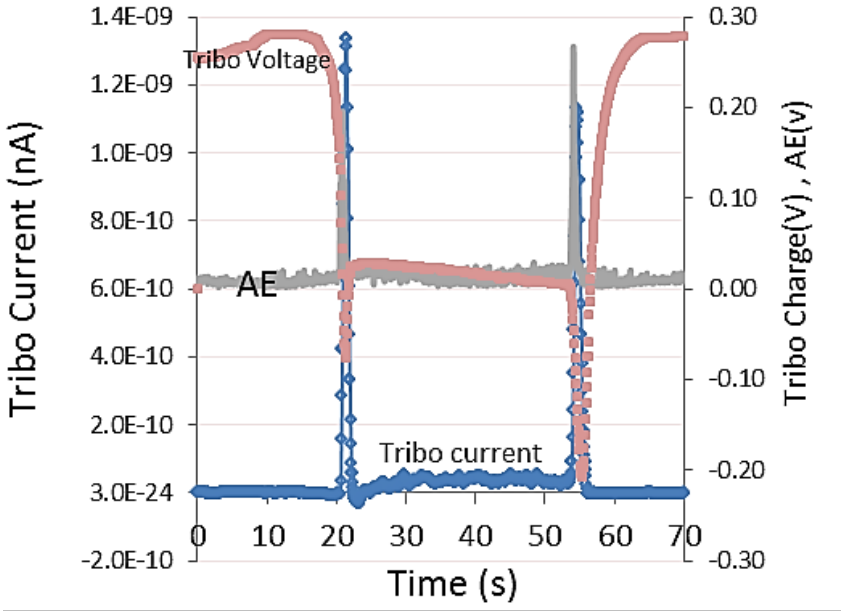

Figure 5-26: Tribovoltage and AE measurement plotted with tribocurrent for similar initial velocity

The results in Figure 5-26 show that the AE spike occurs marginally before the tribocurrent spike for both deceleration and acceleration phases. The onset of AE signal indicates a sharp increase in surface interaction and contact area, and explains the observed spike in tribocharging. In the constant velocity (slider rubbing against disk) regime, the tribovoltage was generally around the zero-volt line, indicating relatively as little charging (or almost equal charging and discharging) activity takes place in this phase compared to the

deceleration and acceleration phases, where both significant tribovoltage and tribocurrent profiles were present.

In the case of negative peaks of the tribovoltage measurement, the generated excess charges are not as easily discharged through the electrometer (voltage measurement mode) path. As such, the negative peak for the acceleration phase is considerably broader than that of the corresponding tribocurrent peak profile. In addition, the tribovoltage measurement shows that significant charging (or discharging) activity continues to take place for a short time beyond the presence of a detectable AE signal. The electrical circuit in our experiments is the same and three possible paths are suggested for the escape of generated charges at the interface: discharge or leakage across the interface, discharge via electrometer path (during measurement), and leakage during electrometer path. As such, the tribovoltage and tribocurrent measurement could only indicate the degree of interface charge generation qualitatively, but does not quantitatively tell the exact nature or degree of escape of generated charges through each of the possible paths.

5.6 Correlation between Head Disk contact and the Measured Current Magnitude

A stronger slider disk impact will induce higher tribocurrent. As such, it is worthwhile to correlate slider-disk contact intensity with measured current. Slider disk contact is characterized using both AE and LDV. The AE sensor of bandwidth up to 500 kHz is attached to the cartridge side and is isolated from slider. The LDV laser spot is shined on the back of slider body and displacement mode measurement is obtained. Simultaneous measurements are obtained upon reducing disk linear velocity with a data acquisition period of 0.5s. FFT of both the AE and LDV are obtained. In this way, peak amplitude obtained is dependent on vibration mode frequency.

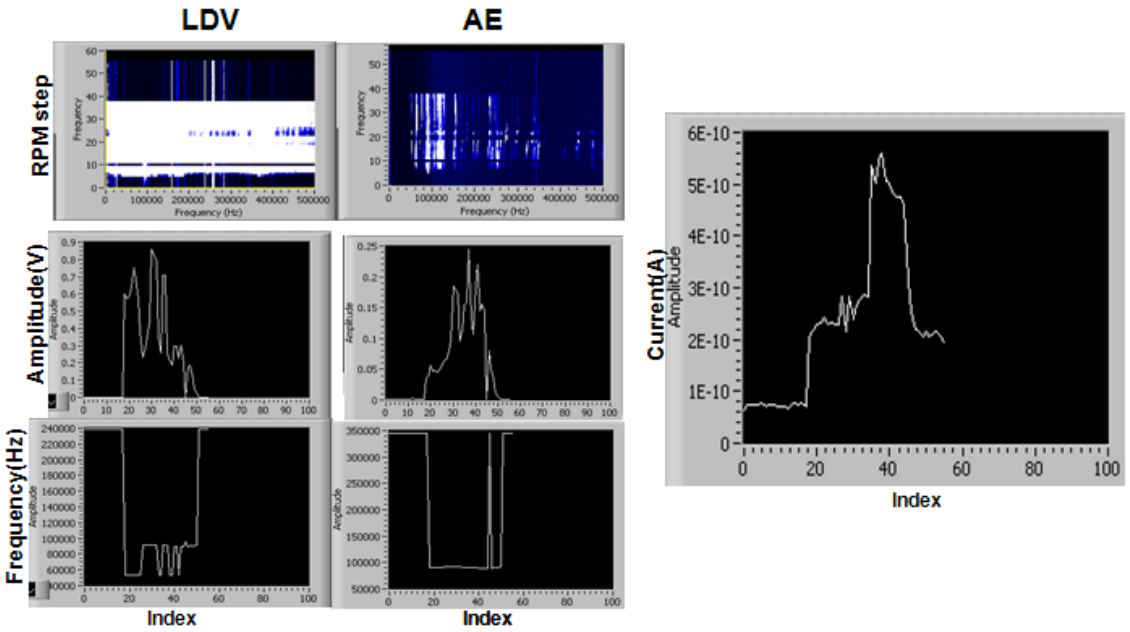

Figure 5-27: AE and LDV measurements (map, amplitude and frequency) compared to tribocurrent

According to equation (5.4), the degree of charge generation is linked to head disk contact. Charge generation is also proportional to head-disk contact. It can be seen that the magnitude of AE and LDV shows similar correlation but not with the measured current. Figure 5-27 shows simultaneous measurements of AE and LDV when the spindle RPM is slowly reduced from 1000 RPM to 100 RPM. The dominant FFT peak with the highest amplitude at each RPM step is recorded and plotted. The corresponding tribocurrent is also monitored. From the results, it can be observed that severe head disk contact occurs with dominant vibration frequencies which range from 60 kHz to 90 kHz. Both AE and LDV show consistencies in detected frequency modes. When compared to AE, the LDV measurement shows additional sensitivity of 60 kHz mode. Generally, an increase in head disk contact causes an increase in generated current. However, there is no distinct correlation between magnitude of contact and current. Improvement in these detections will be done in the future by taking summation of peaks in frequency and time domain rather than just single frequency peak.

5.7 Summary

Tribocharging is a critical HDI phenomenon at ultra-low flying height. Tribocharges build up induces instabilities at the head disk interface due to electrostatic potential which can also degrade MR head's electrical performance. In this work, the developed multifunctional tester is being used as measurement tool for tribocurrent or tribovoltage measurement. It was shown that proper guarding of measurement path is necessary to reduce measurement noise due to stray leakage paths across the cable's dielectric to minimize tribocurrent generation using a low noise coaxial cable. The implementation of this method has been discussed in detail and the results show a significant (ten times) reduction in tribocurrent noise.

Determining the electrical characteristics of the head-disk interface can help to understand the dynamics of charge flow when tribocurrent is generated. Due to the complexity of study when the slider is flying, static voltage current relationship is conducted when slider is resting on disk surface. For the pseudo-dielectric combination of slider disk interface, three electrical models were used to fit the VI curves. It was found that the characteristic of power law has the best correlation.

To investigate tribocharge buildup at the slider-disk interface, tribocurrent measurement was conducted in three regimes: slider flying and disk deceleration, slider dragging at constant speed, and disk acceleration to slider flying. In general, the tribocharging is different for deceleration and acceleration regimes and shown to be related to velocities and acceleration. The onset appearance and changes to the tribocurrent occur at different disk velocity (and have different peak values) for initial velocities used. Additional tribovoltage and AE measurement were performed to understand the phenomenon of tribocharging occurring at the interface.

CHAPTER 6: Conclusion

As areal density continues to increase, head media spacing continues to decrease and as the slider flying height enters the sub-5nm regime. At this ultra-low flying height, new head disk interface phenomena such as electrostatic force (tribocharge) and Van-der-Waal's force (slider lube interaction) play more significant roles in affecting the interface reliability. Moreover, the disk surface needs to be smooth and asperities need to be minimized to reduce defect related HDI problems. Therefore, a good characterization tool is crucial to be able to understand and analyze these problems and to allow introduction of new solutions in slider design and head-disk system integration. The major contribution of this thesis is on the development of such tool and case studies have been carried out to illustrate the measurement capability of the tools in various HDI-related events.

A multifunctional spinstand has been developed to integrate HDI measurement tools such as AE, LDV and missing pulse electronics to provide concurrent measurement capabilities in characterizing slider dynamics and media defects. In this case, multifold information can be obtained that helps to remove spurious information present in any single scan. It had been shown that the LDV's capability to detect media defects is comparable to that of OSA and through special enhancement method. The LDV can also be used concurrently with missing pulse to perform media defect certification that faster and more efficient.

Measurements of slider dynamics are carried out in two different test conditions. The first involves the observation of slider dynamics when a slider interacts with media defects. It has been shown that mapping approach provides two-dimensional information on the size of the interaction regime and nature of interactions. Such a mapping approach is suggested for useful characterization of sliders and in particular, thermal activated protrusions from TFC

technology. Particular interest is shown to study slider dynamics of ultra-low flying height using thermal protrusion. Here, contact induced vibration is analyzed in both frequency and time domain analysis to better understand the touch down process. It is pointed out that slider dynamics is a slider design specific characteristics and frequency domain analysis is shown useful to characterize slider's mechanical response. Time domain information helps to reveal slider's interaction with media surface. Concurrent methods can help to provide better understanding of slider lube interactions using different sensitivity of different measurement methods.

Tribocharging is a critical HDI phenomenon at ultra-low flying heights. Tribocharge build up can induce instabilities at the head disk interface due to electrostatic potential, and it can also degrade MR head's electrical performance. To investigate tribocharge build up at the slider-disk interface, tribocurrent measurement was conducted in three regimes: slider flying and disk deceleration, slider dragging at constant speed, and disk acceleration to slider flying. In general, tribocharging is different for deceleration and acceleration regimes, and is shown to be related to velocity and acceleration. The onset appearance and changes to the tribocurrent occur at different disk velocities (and have different peak values) for different initial velocity used. Additionally, tribovoltage and AE measurements were performed to correlate the tribocharging occurrence at the interface.

6.1 Future Work

One future work includes using the concurrent measurement setup to further study the nature of the defects, and their selectivity to different vibration modes. Measurement sensitivity can be further improved by optimizing the location of measurement transducer. For example, LDV measurement could be more sensitive if the beam spot is positioned at the

leading-edge of slider. Moreover, sensitivities of different methods such as in-situ FH, AE, and LDV need to be further understood.

Particular interest is shown to the study of slider dynamics of a specific HDI-related phenomenon such as slider lube interaction during the touch-down process. Since the HDI phenomenon at ultra-low FH is complex, observations of slider dynamics need to be more systematic and controlled. For example, frequency domain analysis can be obtained at a finer step of TFC power and at each step with monitors of concurrent measurements. Slider dynamics is slider design-specific and in order to have an in-depth understanding, it is also paramount to know slider design specifications for simulation of dynamics using commercial software such as CML or ABSolution. In this case, it is also worthwhile to have optical surface analyzer module on the tester to analyze slider dynamics as well as the degree of slider interaction with the lube and DLC. In this way, observations can be easily understood and analyzed with respect to the expected slider dynamics theory.

Electrical characterization could be useful to understand the nature of tribocharging especially with relation to the carbon overcoat. Further experiments can be conducted using different carbon overcoat compositions and charge flow dynamics can be further understood from the voltage-current relationship of the head disk interface. Correlation between tribocurrent generation and slider dynamics can be further improved by taking summation of peaks in frequency and time domain, rather than just single frequency peak and experiments using different slider and disk combinations.

REFERENCES

[1] “The IBM 350 RAMAC Disk File,” *ASME*, 1984.

[2] “Barracuda Green SATA 6Gb/s 3TB Hard Drive specifications,” *Seagate.com*, 2010.

[3] Wood, RW and Takano H, “Prospects for Magnetic Recording over the Next 10 Years”, in *the Magnetics Conference, Intermag IEEE International Conference*, 2006.

[4] “The Discovery of Giant Magnetoresistance,” *Royal Swedish Academy of Sciences*, October 2007.

[5] Shan X Wang and Alexander Taratorin, *Magnetic Information Storage Technology*, Academic Press, 1999.

[6] Ambekar *et al*, “Effects of Radial and Circumferential Disk Features on Slider Dynamics,” *IEEE Trans. On Magnetics*, vol 45, pp206-211, 2009.

[7] S.N. Piramanayagam, “Perpendicular Recording Media for Hard Disk Drive”, *Journal of Applied Physics*, vol 102, 011301, 2007.

[8] Dieter Weller and Mary.F.Doerner , “Extremely High-Density Longitudinal Magnetic Recording Media”, *Annu. Rev. Mater. Sci*, vol 30, pp 611-644, 2000.

[9] Alexander Taratorin, *Magnetic Recording Systems and Measurement*, Guzik Technical Enterprises Handbook, 2004.

[10] Wu Yihong, “Nano Spintronics for Data Storage”, *Encyclopedia of Nanoscience and Nanotechnology*, 2003.

[11] *S.H.* Charap, “Thermal Stability of Recorded Information at High Densities”, *IEEE Trans.on Magnetics*, vol 333, p 978, 1997.

[12] Y.Tanaka ,“Fundamental Features of Perpendicular Magnetic Recording and Design Considerations for Future Portable HDD Integration”, *IEEE Trans on Magnetics*, vol 41, no 10, pp 2834-2838, 2005.

[13] “HDI-Tribology Roadmap”, in *INSIC/SRC HDD Roadmap workshop.*

[14] Brian *et al*, “The Effects of Disk Morphology on Flying Height Modulation: Experiment and Simulation”, *IEEE Transactions on Magnetics*, vol 38, no 1, January 2002.

[15] Zhou *et al*, “Effects of Environmental Temperature and Humidity on Thermal Flying Height Adjustment”, *Microsystem Technologies*, vol. 16, no 1-2, pp 49-55, 2008.

[16] Ng *et al*, “Disk Clamping Distortion and Slider Crown Sensitivity Induced Flying Height Variation”, *Journal of Magnetism and Magnetic Materials*, vol. 303, pp 72-75, 2006.

[17] M Suk, B.Bhushan and D.B. Bogy, “Role of Disk Surface Roughness on Slider Flying Height and Air Bearing Frequency”, *IEEE Transactions on Magnetics*, vol. 26 no 5, September 1990.

[18] J.F Xu *et al*, “Effect of Disk Topography on Slider Dynamics”, *IEEE Trans on Magnetics*, vol. 42, no 10, October 2006.

[19] Zeng *et al*, “Flyability and Flying Height Modulation Measurement of Sliders with Sub-10 nm Flying Height”, *IEEE Transactions on Magnetics*, vol. 37, no 2, March 2001.

[21] Yuan *et al*, “Sub-mm Disk Waviness Characteristics and Slider Flying Dynamics under Thermal FH Control,”, *Journal of Magnetism and Magnetic Materials*, vol. 320, pp 3189-3191, 2008.

[22] Young *et al*, “Prediction of Track Misregistration due to Disk Flutter in Hard Disk Drive”, *IEEE Trans. on Magnetics*, vol. 38, no 2, pp 1441-1447, March 2002.

[23] Knigge and Talke, “Nonlinear Dynamic Effects at the Head Disk Interface”, *IEEE Trans. Magnetics*, vol. 37, pp 900–905, 2001.

[24] Liu *et al*, “Towards Fly- and Lubricant-Contact Recording”, *Journal of Magnetism and Magnetic Materials*, vol. 320, pp 3183-3188, 2008.

[25] James D Kiely and Yiao-Tee Hsia, “Independent Measurement of Air-bearing Pitch, Roll and Vertical Modulation”, *Journal of Applied Physics*, vol. 98, 114501, 2005.

[26] Khurshudov and Talke, “A Study of Sub-ambient Pressure Tri-pad Sliders using Acoustic Emission,” *ASME J. of Tribology*, vol. 120, pp 54-59, 1998.

[27] Andrei Khurshudov and Peter Ivett, “Head-disk Contact Detection in Hard-disk Drives”, *Journal of Wear*, vol. 255, pp 1314-1322, 2003.

[28] Klaassen and Contreras, “Thermal Transient Response of Electrical Self Heating in Current-in-Plane Magnetoresistive Heads”, *IEEE Trans. on Magnetics*, vol. 42, no 10, October 2006.

[29] Ramesh *et al*, “Study if Head/Disc Interface Dynamics using a Thermal Asperity Sensor”, *IEEE Trans. on Magnetics*, vol. 35, no 5, Sept 1999.

[30] D.Abraham, *US Patent 5 527110*, 1993.

[31] Gordon J Smith, “Dynamic In-Situ Measurements of Head-to-Disk Spacing”, IBM, *IEEE Trans. on Magnetics*, vol. 35, no. 5, September 1999.

[32] Leng *et al*, “Bump Characterisation with MR/GMR Head as Transducer”, *IEEE Trans. on Magnetics*, vol. 36, no. 5, Sept 2000.

[33] Klaassen and Peppen, “Slider-Disk Clearance Measurements in Magnetic Disk Drives using the Readback Transducer”, *IEEE Trans. on Instrumentation*, vol. 43, no 2, 1994.

[34] *W.K* Shi *et al*, "Use of Readback Signal Modulation to Measure Head/Disk Spacing Variations in Magnetic Disk Files", *IEEE Transactions on Magnetics*, vol. 23, no. 1, January 1987.

[35] R.I Wallace, "The Reproduction of Magnetically Recorded Signals", *The Bell Tech Journal*, pp. 1145-1173, 1951.

[36] Liu *et al*, "In-situ Characterisation of Head Disk Clearance," in *ASME/Tribol symp. On interface tribology towards 100 Gb/in^2 and beyond*, Seattle USA, vol. 51, pp. 51-58, 2000.

[37] *W.R* Harper, "Triboelectrification", Oxford, 1967.

[38] Peter M. Ireland, "The Role of Changing Contact in Sliding Triboelectrification," *Journal of Physics D*, vol. 41, pp. 1-11, 2008.

[39] Mike Suk,"Effect of Tribocharging on Lubricant Redistribution", *IEEE Transaction on Magnetics*, vol. 41, no. 2, February 2005.

[40] Liu *et al*, "Tribo-Magnetics and Nanometer Spaced Head-Disk Systems", *IEEE Trans. On Magnetics*, vol. 37, no. 2, March 2001.

[41] Park *et al*, "Numerical Investigations of Contamination Particles Trajectory in a Slider Disk Interface," *IEEE Trans on magnetics*, vol. 36, pp. 2739-2741, 2000.

[42] Zhu Feng *et al*, "A Study of Tribo-charge Emission at the Head–Disk Interface", *Journal of Applied Physics*, vol. 85, no. 8, April 1999.

[43] Dae-Young Lee *et al*, "Effect of relative humidity and disk acceleration on tribocharge build-up at a slider-disk interface", *Tribology International*, vol. 80, p. 1253, Aug. 2007.

[44] Feng *et al*, "A study of electrical charge at head-disk interface", Tribology letters, vol. 18, no. 1, pp. 53-58, 2005.

[45] H.S Park, J.Hwang, S.H and Choa, "Tribocharge build-up and decay at a slider-disk interface", *Journal of Microsystem Technologies*, vol. 10, p. 109-114, 2004.

[46] Weissner and Talke, "Load/Unload Measurements using laser Doppler vibrometry and acoustic emission," *Tribology International*, vol. 33, no. 5-6, pp. 367-372, 2000.

[47] Yuan *et al*, "Engineering Study of Triple Harmonic method for in situ characterisation of head-disk spacing*", J. Magnetism & Magnetic materials*, vol. 239, p.p 367-370, 2002.

[48] Liu *et al*, "Lube-Surfing Recording and Its Feasibility Exploration," *IEEE Trans. On Magnetics*, vol. 45, no. 2, pp. 899-904, 2009.

[49] Leong *et al*, "Characterization of Slider Dynamics and Media Defects by Concurrent Methods using a Multifunctional Spinstand", *IEEE Trans. on magnetics*, vol. 45, no. 11, 2009.

[50] "Missing/Super Pulse Test", *IDEMA Standards*, T13-91.

[51] Martin *et al*, "Targeting the Limits of Laser Doppler Vibrometry", *Polytec whitepaper*, 2005.

[52] Pressesky J, "Towards a New Paradigm for Final Test of Magnetic Media for Hard Disk Drives," *IEEE Trans. On magnetics*, vol. 33, no 1, January 1997.

[53] Bogy *et al*, "Use of the laser Doppler Vibrometer to Measure the Surface Topography of Magnetic Disks", *Journal of Wear*, vol. 107, pp. 227-244, 1986.

[54] Xu *et al*, "Head-Medium Spacing Measurement Using the Read-back signal", *IEEE Trans. on magnetics*, vol. 42, no. 10, Oct 2006.

[55] J.Xu, Y.Shimizu and L.Su, "Drive level measurement of flying height modulation and control of slider disk contact", *Tribology Letters*, vol. 24, no. 2, November 2006.

[56] Yuan *et al*, "In-Situ Flying Height Testing Technology", *APMRC/TMRC*, TU-P-13-01, IEEE, 2002.

[57] Qing *et al*, "Time Evolution of Lubricant-Slider Dynamic Interactions", *IEEE Trans. on magnetics*, vol. 39, no. 5, Sept 2003.

[58] Takahashi *et al*, "Vibration of Head Suspensions for Proximity Recording", *IEEE Trans. on Magnetics*, vol. 34, no. 4, pp 1756-1758, 1998.

[59] Zeng and Bogy, "Dynamics of Suspension-Slider-Air-Bearing Systems: experimental study", *IEEE Trans. on Mechatronics*, vol. 3, no. 3, pp 210-217, 1998.

[60] Pit R et al, "Experimental Study of Lubricant–Slider Interactions", *IEEE Trans. Magn*, vol. 39, pp. 740–742, 2003.

[61] Lee and Polycarpou, "Strategies to Avoid Head-Disk Instabilities due to Adhesion in Ultralow Flying Head-Disk Interfaces, *IEEE Trans. on Magnetics*, vol. 40, no. 4, pp. 3130-3135, July 2004.

[62] Jianfeng Xu *et al*, "Dynamics of Ultra-Low Flying Sliders during Contact with a Lubricated Disk", *Microsyst. Technnology*, vol. 13, pp. 1371-1375, 2007.

[63] Canchi and Bogy, "Slider Dynamics in the Lubricant-Contact Regime", *IEEE Trans. on Magnetics*, vol. 46, no. 3, March 2010.

[64] M.Dluziniewski et al, "DC conductivity of Metal/DLC/Si/Metal Heterostructures", *IEEE Trans. on Dielectric and Electrical Insulation*, vol. 8, no.3, June 2001.

[65] H.Sodolski,"The Current–Voltage Characteristics of Polyester Polymer-Carbon Black Compositions", *Physica Status Solidi (a),* vol. 32, issue 2, pp. 603-609, 1975.

[66] In-Gann Chen and W.B Johnson, "Non-ohmic I-V Behaviour of Random Metal-Insulator Composites near Their Percolation Threshold", *Journal of Materials Science*, vol. 27, pp. 5497-5503, 1992.

[67] Kazuo Oda, Matshushita, “Zinc Oxide Varistors”, *Electric Industrial Co. Ltd.*

[68] Zhao *et al*, “Experimental Investigation of the Effect of Disk Acceleration and Velocity on the Tribology of the Head/disk Interface”, *IEEE Trans. on Magnetics*, vol. 35, pp. 2406-2408, Sept 1999.

[69] Nakayama and Nguyen,“Triboelectromagnetic Phenomena in a Diamond/hydrogenated-Carbon-film Tribosystem under Perfluoropolyether Fluid Lubrication”, *Applied surface science*, vol. 158, pp. 229-235, 2000.

[70] M.Sze, *Physics of Semiconductor Devices*, John and Wiley Sons, 2007.

[71] Brian E.Shultz, “Thermal Fly-Height Control (TFC) Technology in Hitachi Hard Disk Drives*”, Hitachi GST white paper,* 2007.

[72] Ta-Chang Fu and David B. Bogy,“ Drive Level Slider-Suspension Vibration Analysis And its Application to a Ramp-Load Magnetic Disk Drive”, *IEEE Trans. on Magnetics*, vol. 31, no. 6, pp. 3003-3005, Nov 1995.

[73] Yunfeng Li and Roberto Horowitz,“Active Suspension Vibration Control with Dual Stage Actuators in Hard Disk Drives”, *Proceedings of the American Control Conference*, June 25-27, 2001.

[74] “AD8350: 1.0 GHz Differential Amplifier”, *Datasheet, Analog Devices Inc*, 2001.

[75] “AD8351: Low Distortion Fully Differential RF/IF Amplifier,” *Datasheet, Analog Devices Inc*, 2004.

[76] “LMH6703: 1.2 GHz, Low Distortion Op Amp with Shutdown from the PowerWise® Family”, *Datasheet, National Semiconductor Inc*, May 2005.

[77] Ed Grochowski, “*Recording Technologies*”, Hitachi Global Storage Technologies, San Jose Research Center.